SYNTHESIS AND CHARACTERIZATION OF $Bi_{12}SiO_{20}$ THIN FILMS PREPARED BY SOL-GEL METHOD

Asja Veber

Doctoral Dissertation
Jožef Stefan International Postgraduate School
Ljubljana, Slovenia, June 2010

Evaluation Board:

Prof. Dr. Radovan Stanislav Pejovnik, Chairman, University of Ljubljana, Ljubljana, Slovenia

Prof. Dr. Boris Orel, National Institute of Chemistry, Ljubljana, Slovenia

Prof. Dr. Klaus Reichmann, Technical University, Graz, Austria

MEDNARODNA PODIPLOMSKA ŠOLA JOŽEFA STEFANA
JOŽEF STEFAN INTERNATIONAL POSTGRADUATE SCHOOL

Asja Veber

SYNTHESIS AND CHARACTERIZATION OF $Bi_{12}SiO_{20}$ THIN FILMS PREPARED BY SOL-GEL METHOD

Doctoral Dissertation

SINTEZA IN KARAKTERIZACIJA $Bi_{12}SiO_{20}$ TANKIH PLASTI PRIPRAVLJENIH S SOL-GEL METODO

Doktorska disertacija

Supervisor: Prof. Dr. Danilo Suvorov

Ljubljana, Slovenia, June 2010

Index

Abstract

The sillenites $Bi_{12}MO_{20}$ (M = Si, Ge, Ti, Pb, Mn, $B_{1/2}P_{1/2}$) have been recognised as promising bulk materials for electronic applications because their dielectric properties (5.5 GHz: ε = 37.4 - 41, τ_f = -19 – (-84) ppm/K, Q x f = 800 - 8100 and T_{sin} = 680 - 850°C). Among them, $Bi_{12}SiO_{20}$ (BSO) appears to have the most interesting dielectric properties (5.5 GHz: ε = 37.6, τ_f = -20 ppm/K, Q x f = 8100 and T_{sin} = 850°C).

The continuous search for improved properties of electronic devices led us to the preparation of BSO thin films. The following work describes a study of the synthesis chemistry and characterization of BSO thin films prepared by the sol-gel method.

The sols were prepared using $Bi(NO_3)_3 \cdot 5H_2O$ and $Si(OC_2H_5)_4$ as precursors, 2-ethoxyethanol and glacial acetic acid as solvents, ethanol-amine as the chelating agent and formamide as the drying control chemical additive (DCCA). Three syntheses were compared: the synthesis of sol R_h 60, the synthesis of sol R_h 5 and the synthesis of sol R_h 60 with DCCA.

The thin films were deposited on various substrates ($Pt/TiO_2/SiO_2/Si$, sapphire, spinel and Si) by the spin-coating method, pre-heated at 250°C and then annealed at 700°C for 1 h.
The chemical interaction that occurred during the sol synthesis and the deposition of thin films was studied by means of Fourier transformed infrared (FT-IR) spectroscopy. The gel point in the sols, which is an important parameter for a sol-gel derived thin film, was determined by use of a Physica MCR rheometer, by following the change in the viscosity of the sols. The TG/DTA/DSC/EGA analyses were performed on sols and thin films, to determine the pre-heating temperature of the thin films, as this is essential for obtaining dense, crack-free BSO thin films. The phase composition of the thin films was characterized by means of X-ray diffraction (XRD) and transmission electron microscopy (TEM), whereas the morphology and the thickness of the thin films were studied with field-emission scanning electron microscopy (FE-SEM) and atomic force microscopy (AFM).

The quality of BSO thin films critically depends on the molar ratio (R_h) of the sol. We found that sols with the molar ratio R_h 60 are unstable below a concentration of 0.76 M. Furthermore, the rate of the hydrolysis and condensation reaction is too high to obtain dense, crack-free BSO thin films. Therefore, the rate of the hydrolysis and condensation reactions was superseded by reducing the amount of water in the sols, by vacuum drying of the $Bi(NO_3)_3 \cdot 5H_2O$ (sols R_h 5).

The sols R_h 5 are stable across the whole concentration range and a reasonably dense microstructure of BSO thin films with a thickness of 200 nm was obtained. The disadvantage of this synthesis process was the poor wetability of the substrates, due to the high viscosity of the sol.

The most promising sol synthesis to achieve dense, crack-free BSO thin films was the synthesis of sol R_h 60 with DCCA and 2-ethoxyethanol. Such thin films resulted in a dense and homogeneous microstructure with a thickness of 250 nm and a 30-nm average roughness (R_a).

The dielectric properties of the BSO thin films were characterized utilizing both low-frequency and microwave-frequency measurement configurations. The low-frequency measurements (100 kHz - 1MHz) were performed with a parallel insulator-capacitor measurement configuration. At 1MHz the following dielectric properties were determined: ε

$\cong$40 and $\tan\delta \geq 6.10^{-2}$. The dielectric properties at the microwave frequency were measured via the split-dielectric-resonator method at 10 GHz and in addition also with the sputtering planar capacitor configuration (0.5 - 3 GHz). The relative permittivity and dielectric losses measured at 10 GHz were $\varepsilon \cong 40$ and $\tan\delta \geq 17.10^{-3}$, which is in good accordance with the values measured at lower frequencies. When measured by the sputtering planar capacitor configuration the dielectric constant ε remains $\cong$ 40. However, the dielectric losses were significantly higher, $\tan\delta \geq 2.10^{-1}$, indicating that the measuring configuration can strongly affect the measured values of the dielectric properties of the BSO-thin films.

Povzetek

Silenitni materiali $Bi_{12}MO_{20}$ (M = Si, Ge, Ti, Pb, Mn, $B_{1/2}P_{1/2}$) so postali zanimivi za elektronsko industrijo zaradi svojih uporabnih dielektričnih lastnosti (5.5 GHz: ε = 37.4 - 41, τ_f = -19 – (-84) ppm/K, Q x f = 800 - 8100 and T_{sin} = 680 - 850°C). Izmed njih $Bi_{12}SiO_{20}$ (BSO) izkazuje najprimernejše dielektrične lastnosti (5.5 GHz: ε = 37.6, τ_f = -20 ppm/K, Q x f = 8100 and T_{sin} = 850°C).

Prizadevanja k izboljševanju lastnosti elektronskih naprav so me vodile k pripravi BSO tankih plasti. Tako doktorska disertacija opisuje študij sintezne kemije ter karakterizacijo tankih plasti BSO pripravljenih s sol-gel metodo.

Pri pripravi solov sem uporabila $Bi(NO_3)_3 \cdot 5H_2O$ in $Si(OC_2H_5)_4$ kot prekurzor, 2-etoksietanol ali ocetno kislino kot topilo, etanolamin kot stabilizator ter manjšo količino formamida za nadzorovano sušenje tanke plasti.
Tanke plasti so bile nanešene na različne podlage ($Pt/TiO_2/SiO_2/Si$, safir, spinel in Si) s tehniko vrtenja. Nanešene BSO tanke plasti so bile nato pirolizirane pri 250 ° C ter termično obdelane pri 700 ° C,1 h.

Kemične interakcije, ki so nastale pri sintezi solov in v tanki plasti, sem proučevala s pomočjo Fourier-jeve transformirane infrardeče (FT-IR) spektroskopije. Pomemben parameter pri sintezi tankih plasti pridobljene s sol-gel metodo je točka gelacije sol-ov, ki je bila določena iz spremembe viskoznosti sol-ov z uporabo Physica MCR reometera. Za pridobitev gostih BSO tankih plasti je prav tako pomembna določitev temperature pirolize le-teh. Termična analiza (TG / DTA / DSC / EGA) je bila opravljena tako na sol-ih kot tudi na nanešenih tankih plasteh. Fazno sestavo tanke plasti sem zasledovala s pomočjo rentgenske difrakcije (XRD) in presevne elektronske mikroskopije (TEM). Morfologija in debelino tanke plasti sem raziskovala z vrstičnim elektronskim mikroskopom (FE-SEM) in mikroskopom na atomsko silo (AFM).

Kakovost tanke BSO plasti je kritično odvisna od molarnega razmerja R_h. Ugotovila sem, da so soli z molskim razmerjem R_h 60 nestabilni pod koncentracijo 0,76 M. Poleg tega se je izkazalo, da so hitrosti hidroliznih in kondenzacijskih reakcij v teh solih previsoke za pridobitev gostih tankih BSO plasti. Nasprotno pa je zmanjšanje količine vode v solih (sol Rh 5), ki sem ga dosegla z vakuumskim sušenjem $Bi(NO_3)_3 \cdot 5H_2O$, vodilo do nadzorovane hitrosti hidroliznih in kondenzacijskih reakcij.

Soli R_h 5 so bili stabilni v celotnem koncentracijskem območju. Dobljene tanke BSO plasti so izkazovale razmeroma gosto mikrostrukturo z debelino 200 nm. Slaba stran te sinteze je bila neustrezna omočljivost substratov zaradi višje viskoznosti solov.

Najprimernejša sol-gel sinteza za pridobitev BSO tankih plasti je bila sinteza sol-gel R_h 60 kjer so imele tanke plasti gosto in homogeno mikrostrukturo z debelino 250 nm ter povprečno hrapavost (R_a) 30 nm.

Dielektrične lastnosti BSO tankih plasti so bile določene v nizko frekvenčnem področju kot tudi v mikrovalovnem frekvenčnem področju. Meritve dielektričnih lastnosti v nizko frekvenčnem področju v območju od 100 kHz do 1 MHz so bile izvedene z uporabo paralelne kondenzatorske konfiguracije. Izmerjene dielektrične lastnosti BSO tankih plasti pri frekvenci 1 MHz so naslednje: $\varepsilon_r \cong 40$ in $\tan\delta \geq 6.10^{-2}$. V mikrovalovnem frekvenčnem področju so bile dielektrične lastnosti BSO tankih plasti izmerjene z načinom planarne kondenzatorske konfiguracije (0.5 - 3 GHz) ter z resonatorskim načinom merjenja (10 GHz). Izmerjene

dielektrične vrednosti v frekvenčnem območju med 0.5 - 3 GHz so: $\varepsilon_r \cong 40$ in $\tan\delta \geq 2.10^{-1}$, medtem ko pri 10 GHz so: $\varepsilon_r \cong 40$ in $\tan\delta \geq 17.10^{-3}$. Dielektrične vrednosti izmerjene z resonatorskim načinom (10 GHz) se dobro ujemajo z vrednostmi pri nižje frekvenčnih meritvah. Zaradi opisane lastnosti je uporabnost BSO materiala možna tako v nizkem kot tudi v visokem frekvenčnem področju. V primeru merjenja z načinom planarne kondenzatorske konfiguracije pa izmerjene dielektrične izgube izkazujejo, da izbrana metoda merjenja vpliva na dobljene dielektrične vrednosti.

List of abbreviations

ε	permittivity
τ_f	temperature coefficient of resonant frequency
Qxf	frequency-quality factor
BSO	$Bi_{12}SiO_{20}$
T_{sin}	sintering temperature
DCCA	drying control chemical additive
FT-IR	Fourier transform infrared
TA	thermal analysis
TG	thermogravimetry
DTA	differential thermal analysis
DSC	differential scanning calorimetry
EGA	evolved gas analysis
XRD	X-ray diffraction
FE-SEM	field emission scanning electron microscopy
SEM	scanning electron microscopy
SEI	secondary electron imaging
BSEI	back scattered electron image
AFM	atomic force microscopy
R_a	average surface roughness
TEM	transmission electron microscopy
EDS	energy dispersive spectroscopy
R_h	molar ratio: $R_h = [H_2O] / [TEOS]$
rt	an ideal radious of the interstitial ion
CS	chemical solution
CVD	chemical vapour deposition
PVD	pulsed laser deposition
CSD	chemical solution deposition
TEOS	$Si(OC_2H_5)_4$
S_N2	bimulecular nucleophilic type substitutuin mechanism
k_H	relative rates of hydrolysis
k_C	relative rates of condensation
SAXS	small-angel-X-ray scattering
t_G	time of gelation
SBT	$SrBi_2Ta_2O_9$
LNO	$LaNiO_3$
ATR	attenuated total reflection
GSG	ground-source-ground

1. Introduction

1.1 Microwave ceramics

The applications of microwave ceramics in electronics for resonators, filters and antennas, etc. have been rapidly increasing in recent decades. Many researchers have been focused on developing new microwave dielectric materials to enable device miniaturization and increased systems stability.

Three dielectric properties must be considered for materials used in microwave devices: a suitable dielectric constant, a high quality factor, and a near-zero temperature coefficient of resonant frequency. They are required for the small size, low dielectric loss, and high temperature stability, respectively [1, 2].

Among the various microwave ceramics, sillenite compounds $Bi_{12}MO_{20-\delta}$ (M = Si, Ge, Ti, Pb, Mn, $B_{1/2}P_{1/2}$) have emerged as being of particular interest due to their suitable dielectric properties.

1.1.1 Sillenite compound

Bismuth oxide (Bi_2O_3) is an interesting dielectric material with a lot of potential applications, such as optical coatings, metal/insulator/semiconductor (MIS) capacitors and integrated microwave circuits [3]. Bi_2O_3, exhibits extraordinarily rich phase polymorphisms, i.e., the formation of α-monoclinic, β-tetragonal, γ-body centered (bcc), and δ-face centered cubic (fcc) phases (Scheme 1) [4].

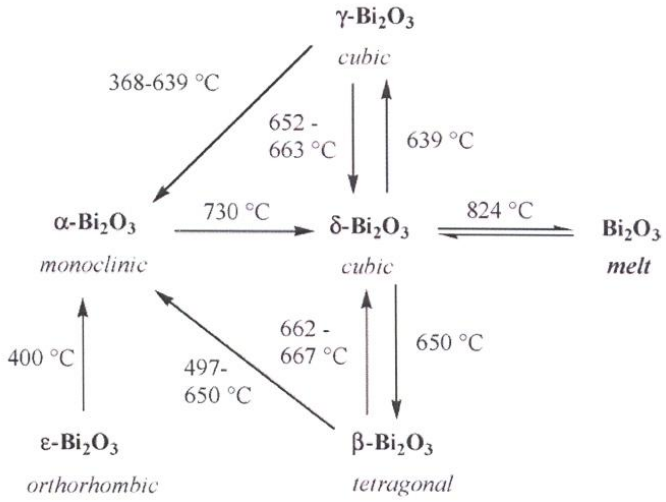

Scheme 1: Transformation temperatures for α-, β-, γ- and δ-Bi_2O_3 [4]

The stable or metastable occurrence of theses phases depends on the various conditions of temperature/thermal treatment and chemical doping [5]. Among these different phase modifications of Bi_2O_3, the γ-bcc phase has been of particular interest for basic science as well

as for technological applications. The body cantered cubic γ-form of pure Bi_2O_3 is a metastable phase which appears during cooling of the high-temperature-stable fcc δ-form [6]. The γ-phase can be stabilized by the presence or addition of small amount of other cations, such as Si, Ge, Ti, Ga, etc [7]. The compounds which form are known as sillenites, named after Sillen, who discovered this special class of materials [8].

Sillenite-type compounds crystallize in the I23 space group with a body centred cubic cell. Fig. 1 shows the structure of ideal sillenite, which consists of a Bi-O framework. The Bi^{3+} ions within the framework are in octahedral coordination with the apical oxygen ion at a very short distance of ~2.05 Å and with two basal-plane oxygen ions at a distance of ~2.2 Å, and with another two at a longer distance ~2.6 Å. The two oxygen ions from the adjacent octahedron are at relatively long distance of ~3.1 Å from Bi^{3+} and are not usually considered as being part of the first coordination sphere. Opposite the apical oxygen, a stereochemically active $6s^2$ lone electron pair that completes the distorted octahedron extends over a distance of 1.8 Å [9]. The Bi-O octahedron connects to the geometrically regular M-O tetrahedron. Each of the M-O tetrahedrons are formed by four oxygen anions surrounding the M cation, which is located in tetrahedral intersticies [10]. The octahedral sites (A-site) in this study are occupied with Bi^{3+} ions within the Bi-O framework, while the tetragonal sites (B-site) are vacant or occupied by either Bi^{3+} or M^{n+} ions (n+ is the space charge of the M atom). This structure can be described with the general formula $Bi_{12}MO_{20}$. According to Radaev and Simonov [11] the tetrahedral positions are 80% occupied by Bi^{3+}ions and 20% vacant. Bi^{3+} ions occupy the tetragonal site by removing an oxygen ion from the tetrahedron and accommodating the lone electron pair to fill this space [11, 12]. As a result, the size of the M^{n+} cation is not limited by the size of the tetrahedral interstices, which allows the incorporation of large ions. Radaev and Simonov [11] proposed a new general formula $Bi_{12}(Bi_{4/5-nx}M^{n+}{}_{5x})O_{19.2+nx}$ ($0 \leq x \leq 0.2$), where n is the charge of the M ion.

The sillenites that have their oxygen sublattice fully occupied, either by oxygen ions or the lone-electron pairs of Bi^{3+} ions, are considered to be stoichiometric. Among the various sillenite compounds described in the literature, the only stoichiometric compound is $Bi_{12}SiO_{20}$ [9].

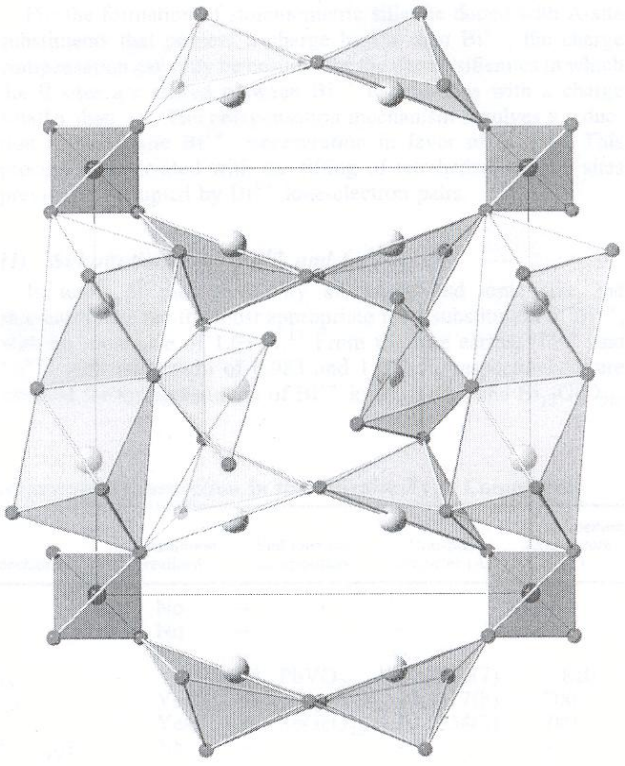

Figure 1: Structure of the ideal sillenite $Bi_{12}GeO_{20}$ projected on (x,y) plane: $-0.2 < z < 0.2$ [10]

It is important to note that sillenite compounds, especially those where M= Ti, Ge, Si display a remarkable array of physical properties and behaviours. They are wide-band-gap, high-resistivity, semi-insulating materials that are at the same time photocunductive, photoluminescent, electro-optic, magneto-optic, acuosto-optic, optical active, as well as piezoelectric. It follows that they present excellent photorefractive and photochromatic characteristics, hence, the potential for technological applications in opto-electronics, photonics and optical information processing that these systems bring forward is tremendous [13-28]. Recently, however, sillenites have begun to be considered for use also as dielectrics in the field of electronics [29].

1.1.1.1 Dielectric properties of sillenite compounds

The dielectric properties of six sillenite compounds $Bi_{12}MO_{20-\delta}$ (M = Si, Ge, Ti, Pb, Mn, $B_{1/2}P_{1/2}$) syntheses by solid-state reaction method were characterized by Valant and Suvorov [29] and are described in Table 1. Measurements of the microwave dielectric properties were performed at 5.5 GHz.

Table 1: B-Site Ionic Radii, Cell Parameters, Sintering temperatures, and Microwave Dielectric Properties, Measured at 5.5 GHz of $Bi_{12}MO_{20-\delta}$ Compounds (M = Si, Ge, Ti, Mn, $B_{1/2}P_{1/2}$) [29]

	B-site ionic Radius (Å)	Lattice parameter(Å)	ε	τf (20-60°C) (ppm/K)	Q * f (GHz)	Sintering temp. (°C)
$Bi_{12}(B_{1/2}P_{1/2})O_{20}$	0.14	10.1515	37.4	-19	850	780
$Bi_{12}SiO_{20}$	**0.26**	**10.109**	**37.6**	**-20**	**8100**	**850**
$Bi_{12}GeO_{20}$	0.39	10.143	38	-31	7800	850
$Bi_{12}MnO_{20-\square}$	0.39	10.217	39.4	-35	800	720
$Bi_{12}TiO_{20}$	0.42	10.175	41	-32	3300	800
$Bi_{12}PbO_{19}$	0.98	10.262	38.6	-84	2900	680

From Table 1 we can see only minor differences in the permittivity of the sillenite ceramics. Permittivity values varied in the range from 37.4 for $Bi_{12}(B_{1/2}P_{1/2})O_{20}$ to 41.0 for $Bi_{12}TiO_{20}$. Independence of the permittivity from the nature of the B-site (tetrahedral site) ions can be explained by the fact that the total polarizability of the sillenite unit cell does not change significantly with the change in the ionic polarizability of the B-site ions due to dilution of the B-site ions by the large number of bismuth and oxygen ions.

In contrast to the permittivity, the temperature coefficient of resonant frequency (τ_f) strongly depends on the composition of sillenite compounds. The most temperature dependent is the resonant frequency of the $Bi_{12}PbO_{20}$ samples with τ_f = -84 ppm/K, while the smallest τ_f values are recorded for $Bi_{12}SiO_{20}$ (BSO) -20 ppm/K and for $Bi_{12}(B_{1/2}P_{1/2})O_{20}$ -19 ppm/K. A correlation exists between the ionic radius of the B-site ions and τ_f. The B-site ions in the sillenite crystal structure are located in the tetrahedral interstices and coordinated with four oxygen ions. In such an arrangement the ideal radius of the interstitial ions allows close-packing of all five ions (Fig. 2 b). In such case an ideal radius (rt) can be calculated from the equation [29]:

$$rt = \left(\sqrt{3}/_2 - 1\right) \cdot R = 0.225 \cdot R = 0.31\ \text{Å} \qquad (1)$$

where R is the atomic radius of the anion.

The calculated ideal radius of an interstitial ion for the oxygen tetrahedron is 0.31 Å. When the interstitial ion is larger than the ideal, the oxygen ions must move apart to accommodate the interstitial ion in the tetrahedral interstice (Fig 2 c). Ions which are smaller than the ideal can occupy the tetrahedral interstice without any changes in the O-O bond lengths (Fig. 2 a).

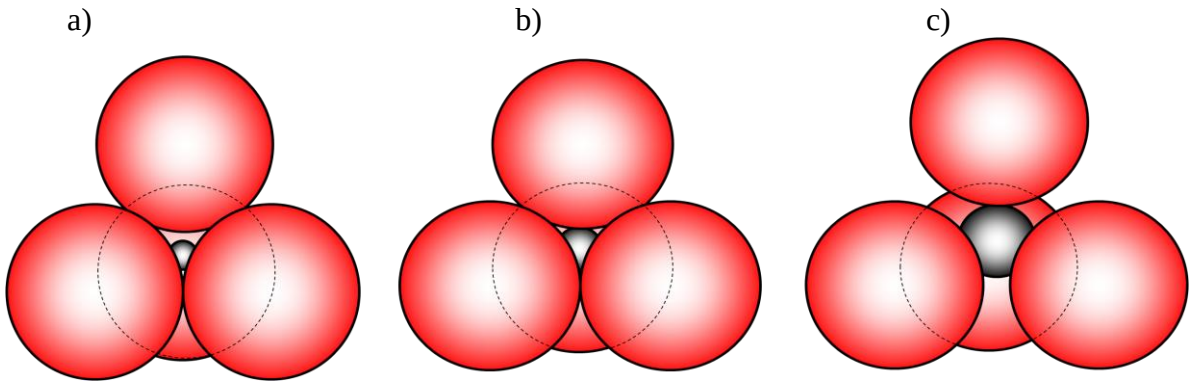

Figure 2: Schematic presentation of the MO_4 tetrahedron packing for different size of M ions: a) M ion is smaller than the ideal size, b) the ideal size of M ion, c) ion larger than ideal [29]

The large tetragonal site ions induce changes in the structure of the oxygen network and in this way affect the τ_f.

In addition, all deviations from a close-packed arrangement of the ions in the crystal structure will also be reflected in dielectric losses (Fig. 3). For example, $Bi_{12}(B_{1/2}P_{1/2})O_{20}$ with the smallest B-site ion has a high dielectric loss, which results in a low Qxf (frequency-quality factor) value of only 850 GHz (measured at 5.5 GHz). With approaching of B-site radius to the ideal radius of the interstitial ions (rt) the Qxf values increase. Two sillenites, $Bi_{12}GeO_{20}$ and $Bi_{12}SiO_{20}$, with their B-site close to the ideal and with a near-close-packed arrangement of the tetrahedron, exhibit the peaks in the Qxf values of the sillenite studies 7800 and 8100 GHz (at 5.5 GHz), respectively [29]. In contrast, by further increasing the value of B-site radius from the ideal radius the Qxf values decrease [29].

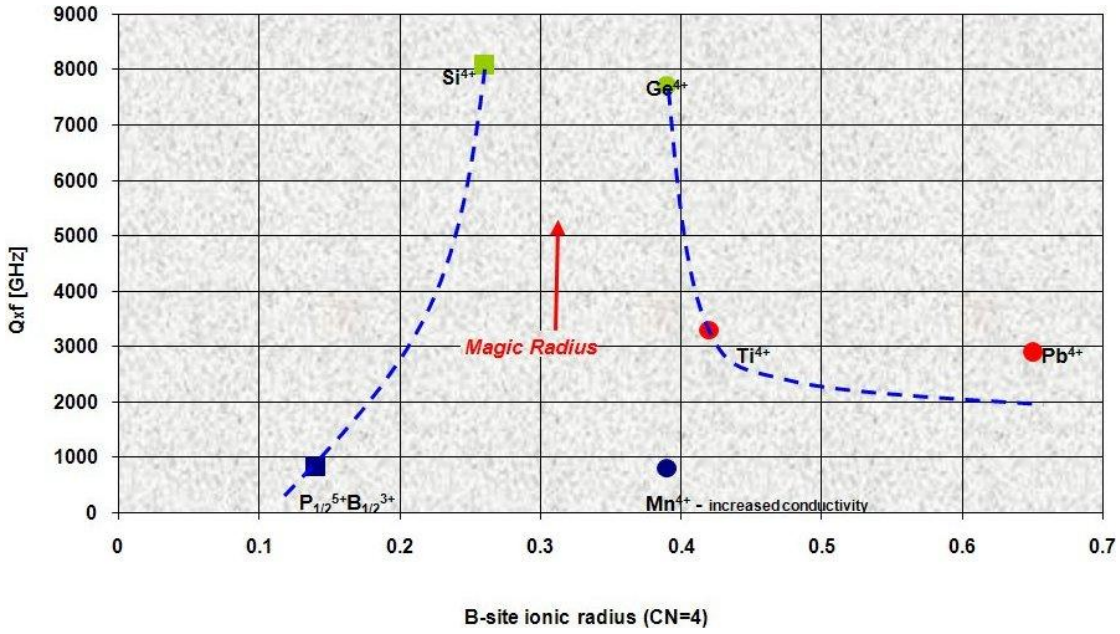

Figure 3: Q x f values, measured at 5.5 GHz, as a function of the B-site ionic radius of the stoichiometric sillenite compounds [29]

In the case of the low-frequency dielectric measurement, the obtained values of the permittivity and the dielectric losses for BSO single crystal, which was grown by Czochralski method, was 56 and 1.5 10^{-4}, respectively [30].

In addition to the ceramics' microwave properties, a high degree of materials homogeneity is expected for electronic applications. In the conventional solid-state synthesis of multicomponent ceramics the constituent oxides (or suitable salts, such as carbonates) are mixed, or milled to achieve better homogeneity and a reduction in the particle size before calcination. This is because the solid-state reaction occurs by the diffusion of oxides; therefore the distribution and particle size are important. It is often necessary to repeat calcinations steps with intermediate milling to improve the homogeneity and to complete the reaction. These steps can be an additional source of contamination. High calcination temperatures can also affect the stoichiometry due to the volatility of the reactants, and this issue is particularly important in the case of bismuth-containing ceramics. The problems that are typically associated with solid state synthesis are a broad particle size distribution, poor sinterability, the presence of secondary phases and the loss of homogeneity.

In continued research to overcome the problems of solid-state synthesis and to improve the properties of microwave ceramics a synthesis method such as the chemical solution (CS) method is used. The CS process allows the synthesizing of ceramic materials with a high homogeneity, since the precursors are mixed at the molecular level in the solution, this allows a sub-micron particle size and significantly lower processing temperatures.

1.2 Thin films

In recent years, thin-film science has grown into a major research area. The importance of coatings and the synthesis of new materials for industry have resulted in a tremendous increase in thin-film processing technologies. This development goes hand-in-hand with the explosion of scientific and technological breakthroughs in electronics, optics and nanotechnology.

1.2.1 Methods for thin-film deposition

Today, the chemical vapour deposition (CVD) and physical vapour deposition (PVD) methods, as well as chemical solution deposition (CSD), such as sol-gel, are mainly used for the production of thin ceramic layers. Compared with other fabrication methods for ceramics coatings, the main advantage of sol-gel deposition is its ability to prepare thin films with a wide variety of chemical compositions and microstructures. Unlike many vapour phase methods, control of stoichiometry in a multicomponent oxide coating is straightforward, as precursors for all the cations are mixed in the coating solution before deposition. a unique property of the sol-gel route is the ability to go all the way from molecular precursors to materials, allowing a better control of the whole process (precise control over composition, its homogeneity, large area deposition…). In addition, the sol-gel deposition method allows lower synthesis temperature. However, the most important advantage of the sol-gel method in comparison with other coating methods is its ability to tailor the microstructure of the deposited film by varying the synthesis parameters. Another advantage is the relatively low cost of the process compared with vapour phase coating technologies that require complex vacuum chambers.

BSO thin films have already been synthesised by the Chemical Vapour Deposition (CVD) [31], the Pulsed-Laser Deposition (PLD) [32, 33] and Sol-gel processes [34-36]. S. N. Plyaka and co-workers [34] studied the differences in the conductivity and activation energy values in thin films and single crystals. E. O. Klebanski and co-workers [35] studied the optical properties of BSO thin films, while M. Jain [36] studied BSO thin films for pyroelectric

detector applications. However, the microwave properties of BSO thin films have not been reported yet. Moreover, the influence of the synthesis parameters on the microstructural development that has a direct effect on the dielectric properties of BSO thin films has not been investigated and discussed yet.

1.3 Sol-gel method

Sol-gel process has brought a new view in the domain of glass and ceramics fabrication and has highlighted the importance of chemistry during the complete fabrication lines of the material, from the initial chemical precursors to the final products. The basic idea is to progressively create an oxide network by a polymerization reaction of the chemical precursor to the final products. Coatings prepared by the sol-gel process begin as liquids or dispersions and end up as dense oxide ceramics. The coatings' structure and composition undergo tremendous changes during the process. The term sol-gel is used to describe the first stage of the process in which the material transforms from a sol with fluid-like properties to a gel with solid-like properties. A sol is composed of colloidal ceramic particles dispersed in a liquid or polymerizable metallorganic precursor dissolved in a solvent. Polymerization leads to the development of an interconnected solid network with an interspersed liquid phase, a structure called a gel [37]. Following the gelation stage, thermal treatments are used to convert the coating to an inorganic ceramic oxide. Many variations can be brought to the sol-gel synthesis of ceramics. In fact, sol-gel processing does not only designate a unique technique, but very broad type of procedures that centralize around a single scheme, as presented in Fig. 4 [38].

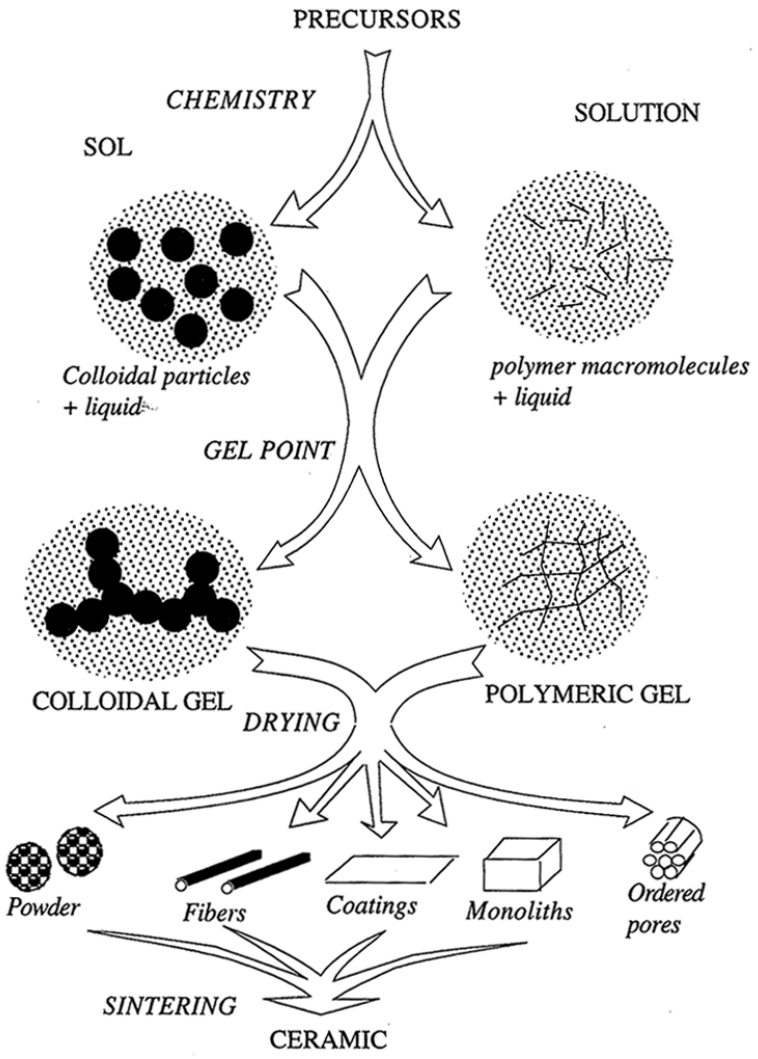

Figure 4: Simplified chart of sol-gel process [38]

The first step of any sol-gel process always consists of selecting the precursors of the wanted materials. It is the precursor that, because of its chemistry, leads the reaction towards the formation of either colloidal particles or polymeric gels. When the future material is composed of several components, then the use of a combination of different precursors enhances the different chemical synthesis and hence different products. Sol-gel is now used to prepare coatings, ceramics powder, monoliths, ordered pores and fibres. The most widespread use of sol-gel process is for coatings [39]. Application of these coatings could be found as reflective and antireflective coatings on architectural glass [40, 41], dielectric coatings [42], ferroelectric coatings [43, 44], electrochromic coatings [45, 46] and protective coatings for metal [47]. The disadvantages of the coating processes are that the coating thickness rarely exceeds one micron without cracking, metastable undesired crystalline phase can form during heating, and the viscosity of the coating solution might be changed during the ageing of the sols. Nevertheless, the sol-gel coating process continues to make an impact for many coating applications.

As already mentioned the sol-gel process starts with preparing a precursor solution containing colloidal or metallorganic ceramic precursors. The most common metallorganic precursor is the metal alkoxide, $M(OR)_n$, which is comprised of a metal atom (M), of valance (n), bonded to one or more alkoxy groups (OR) [48]. The alkoxy group contains an alkyl group (R), such as ethyl (C_2H_5), or methyl (CH_3).

There are three general methods for the preparation of multi-component precursor solution for the fabrication of oxide thin films:

1. the all alkoxide method,
2. the alkoxide salt method,
3. other methods.

An oxide network is formed via the hydrolysis and condensation reactions of molecular precursors. This chemistry is controlled by parameters such as the H_2O / $M(OR)_n$ ratio (R_h), catalysis or the molecular structure of the precursors. The crucial points which determine the reactivity of the starting materials are the polarity of the metal-ligand bond, the coordination number (N) of the central metal in relation to the number of metal-ligands bonds (Z) and the electronic and steric properties of the ligands attached to the central atom. This latter can be simply modified by oligomerization, solvation or the addition of the nucleophilic chemical additives, which lead to tailoring of the coordination sphere of the precursors ions.

The selection of the precursor compounds and the solvents is a very important step in the precursor solution approach for the fabrication of the thin films. The most important points to be considered are:

1. the nature of the initial species,
2. the formation of mixed precursor ions species,
3. the influence of the solvent,
4. the elimination of the organics,
5. the temperature of crystallization.

Thin films are prepared by the deposition the alkoxide-based or colloidal solution onto a substrate. During this deposition a uniform liquid layer is formed, evaporation of the solvent and other volatiles begins, and the coating solidifies. Thermal treatments then cause several processes (e. g., pyrolysis of residual organics, densification, and crystallization) that shapes the structure of the ceramic coating.

1.3.1 Selection of precursor, solvent and additive

The first step in the sol-gel alkoxide method is the selection of the alkoxide for each element of the desired composition, selection of solvents and additives, and then the synthesis of the solution containing the precursor cations.

Alkoxides of most metals can be synthesized or obtained commercially, however alkoxides vary in their physical characteristics (volatility, solubility, hydrolysis rate ect.). These physical characteristics depend on the chemistry of the metal and alkyl group [48, 49]. Aloxides contain metals with M-O-C bonds. Alkoxides of metals with low electronegativity (Na, Li, Ti) have more polarized M-O bonds and tend to associate to form oligomers (dimmers, trimers, etc.) or polymeric solids to lessen the polarity. Alkoxides of metals with a higher electronegativity (Si, Sn, etc.) tend to be monomeric and more volatile. The alkyl group also influences the properties. The tendency toward oligomerization decreases as the length of the alkyl group increases due to partial charge and steric effects [50, 51]. This limits the ability of a metal to increase its coordination number, for example, titanium is pentacoordinated in titanium etoxide, but tetracoordinated in titanium isopropoxide [52].

The solution is comprised of alkoxide [M(OR)] in an alcohol solvent. The addition of water to an alkoxide solution results in hydrolysis followed by condensation reactions, network formation, and the eventual development of a continuous polymeric gel. The hydrolysis and condensation rate increases as the electronegativity (χ) of the metal decreases. The rate of hydrolysis and condensation for titanium alkoxides is therefore much higher than of silicon alkoxide (χ_{Ti}= 1.5, χ_{Si}=1.8). While many alkoxides have been synthesized and used successfully in thin-film processing, some alkoxides have a low solubility are difficult to prepare and are not stable over time [53, 54].

Most advanced ceramics are multicomponent materials having two or more types of cations in the lattice. Since alkoxide precursors are mixed at the molecular level in the solution a high degree of homogeneity is expected. However, a major problem in forming a homogeneous multicomponent solution is the unequal hydrolysis and condensation rate of the alkoxides. This may result in phase separation, during hydrolysis or thermal treatment, leading to higher crystallization temperature or even undesired crystalline phases. It is therefore necessary to prepare a solution of high homogeneity in which cations of different types are uniformly distributed at an atomic scale through M-O-M bridges.

The alkoxide-salt approach can overcome the problem of un-equal hydrolysis and condensation rate in an all-alkoxide approach. For some elements of the desired composition a salt can be selected as precursor instead of alkoxide [55, 56]. The term salt for the described process basically refers to carboxylates, but also includes the use of nitrates, sulfates, carbonates, etc. For most salts carboxylate with medium length ligands is the preferred precursor compound. The carboxylate anions are versatile ligands capable of:

1. existing simply as counter anions,
2. binding the cations,
    a) unidentate,
    b) chelating,
    c) bridging modes.

Acetates based on di- and trivalent metals show a high reactivity towards alkoxide and are easily incorporated in mixed cation species [57-60]. Nitrates are also viable candidates, because they have high solubility and decompose cleanly. For example, Li and Thompson [61] used $Al(NO_3)_3 \cdot 9H_2O$ with $Si(OC_2H_5)_4$ to prepare mullite. Yao and Hong [62] used $Bi(NO_3)_3 \cdot 5H_2O$ to prepare nanocrystals of $B_{12}TiO_{20}$, while H.Gu [63, 64] reported that in the bismuth titanate system, were bismuth nitrate was used as aprecursor, the problem is in the stability of the sols. The bismuth precursor easily reacts with water to yield white precipitate $BiONO_3$ and hence the solution is unstable and decomposes within a short time [63, 64]. Kim [65, 66] reported that alkanolamine is very effective in the stabilization of bismuth precursor and as result a stable sol is formed [67-69]. Other salts such as chlorides have stable anions which can contaminate the final ceramics, therefore they are not appropriate for sol-gel synthesis.

In sol-gel processing, the homogeneity of the gels is very important for further processing of the material. Therefore, in a multicomponent system chemical additives are always used in order to improve the process by protecting the precursors from precipitation or by controlling the rate of polymerization. Such additives can be solvent [70-74], acid or based catalysis[75-77], stabilizing agents [65-69, 78-80] or drying control chemical additives (DCCA) [37, 81-83]. The influence of solvent can be multiple; it can form or stabilize intermediates and control the concentration of the precursor that influences the gelation kinetics. Solvents can be classified as polar or non polar and as protic or aprotic. With regard to solvating power, the important characteristics of solvents are:

1. Polarity, which largely determines the solvating ability for polar or non polar species.
2. Dipole moment determines the length over which the charge on one species can be felt by surrounding species.
3. The availability of labile protons determines whether anions or cations are solvated more strongly through hydrogen bonding. The hydrolysis of the precursor may be catalysed both by H_3O^+ and OH^- ions, hydrogen bridging between these species and the solvent obviously reduce their catalytic activity and therefore the hydrolysis reaction rate. Protic solvents favour the acid catalysed hydrolysis, by rendering the H_3O^+ ions more electrophilic, whereas aprotic solvent accelerates the basic catalysed hydrolysis, by rendering the OH^- ions more nuclephilic [84]. The condensation step according to R. Corriu [85] is also differently affected by the solvent, depending on

the pH. The acid-catalysed mechanism occurs between protonated silanol groups. Protic solvents hydrogen bonds to the deprotonated groups of silanols and in this way promote acid condensation. An opposite effects is expected for aprotic solvents.

Table 2: Physical properties of solvents that are widely used in the sol-gel method

Solvent		Polarity	Dipole moment	Dielectric constant
Water (H_2O)	protic	polar	1.84	78.5
Ethanol (C_2H_5OH)	protic	polar	1.69	24.3
2-ethoxyethanol ($C_4H_{10}O_2$)	protic	polar and non polar	2.08	-
Acetic acid ($C_2H_4O_2$)	protic	polar	1.74	6.2
Formamid (CH_3ON)	aprotic	non polar	3.7	110
Dioxane ($C_4H_8O_2$)	aprotic	non polar	0	2.21

Most metal alkoxides are very reactive towards hydrolysis and condensation. They must be stabilized to avoid precipitation. These reactions are controlled by adding complexing (stabilizing) agents that react with metal alkoxides at the molecular level, giving rise to a new molecular precursor of different structure, reactivity and functionality. The carboxylic acid, such as acetic acid and acetylaceton, which act as hydroxylated nucleophilic ligands, help in controlling the hydrolysis rates by decreasing the functionality of the precursor. Metal alkoxides react with organic acid according to the reaction

$$M(OR)_n + xRCOOH \rightarrow M(OR)_{n-x}(OOCR)_x + xROH \qquad (2)$$

This reaction was used by Doeuff et al. [86, 87] to modify $Ti(OBu^n)_4$ by acetic acid and to stabilize it against precipitation. They showed that the acetate groups behave as bidenatate ligands. This enables the control of both the hydrolysis and condensation process. A. Campero [88] found that acetic acid reacts with $Si(OEt)_4$ in a similar way. However in this case the reaction is much more difficult because a nucleophilic attack on Si is more difficult than for Ti, since titanium may easily increase its coordination to a stable six-fold coordination.

$$Si(OR)_4 + AcOH \rightarrow Si(OR)_{4-x}(OAc)_x + xROH+(1-x)\ AcOH \qquad (3)$$

Thus in the reaction the value of x should be smaller than 1. Excess acetic acid can react with removed alcohol to give ester and water can promote the further hydrolysis of $Si(OEt)_4$.

$$C_2H_5OH + CH_3COOH \rightarrow CH_3\text{-}COO\text{-}C_2H_5 + H_2O \qquad (4)$$

R. Winter [83] and Y. Sugahara [89] studied the role of drying control chemical additive (DCCA) on the polymeric structure. Formamide is a typical DCCA and its addition to a mixture of alkoxide, water and alcohol, improves the processing control of the gels structure by modifying the hydrolysis and condensation reactions.

1.3.2 The sol-gel chemistry of silicon alkoxide $Si(OR)_4$ ($R = C_2H_5$)

In sol-gel synthesis, the sol transforms to the gel via hydrolysis and condensation reaction (Eq. 5-9). The result of the hydrolysis of silicon alkoxide is a formation of the Si-OH group called silanol in which a hydroxyl ligand is bondend to a silicon atom. Complete hydrolysis of silicon alkoxide would give silicic acid, however this does not occur [90]. Instead, a condensation occurs between a silanol and ethoxy group to form a bridging oxygen or siloxane group Si-O-Si. Condensation leads to the growth of the structure by the formation of metal-oxygen-metal bonds.

Hydrolysis:

$$Si(OR)_4 + H_2O \rightarrow Si(OH)(OR)_3 + ROH \quad (5)$$

$$Si(OH)(OR)_3 + H_2O \rightarrow Si(OH)_2(OR)_2 + ROH \quad (6)$$

$$Si(OH)(OR)_2 + H_2O \rightarrow Si(OH)_3(OR) + ROH \quad (7)$$

Condensation:

$$\equiv Si\text{-}OR + HO\text{-}Si\equiv \rightarrow \equiv Si\text{-}O\text{-}Si\equiv + ROH \quad (8)$$

$$\equiv Si\text{-}OH + HO\text{-}Si\equiv \rightarrow \equiv Si\text{-}O\text{-}Si\equiv + H_2O \quad (9)$$

The above reactions demonstrate that the reaction from alkoxysilane to a solid material is not a simple one, since many different intermediates are possible [91]. It is very difficult to separate hydrolysis from condensation, because in most cases condensation begins as soon as partially hydrolyzed groups are formed.

From reactions 8 and 9 it can be seen that two partially hydrolyzed molecules can link together in a condensation reaction by liberating small molecules, such as water or alcohol. This type of reaction can continue to build larger and larger silicon-containing molecules by the polymerization process (Fig. 5) [91].

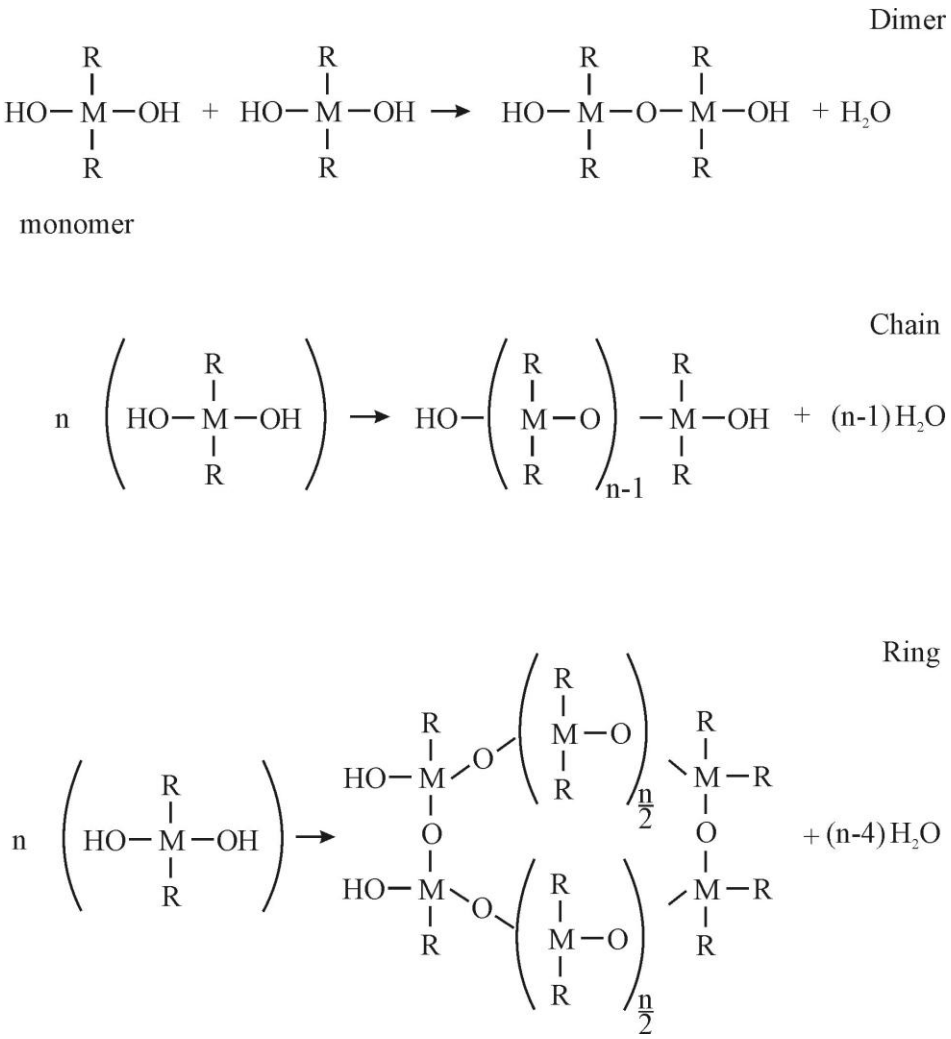

Figure 5: Formation of rings and chains by bifunctional (f = 2) monomer: a) dimer, B) chain and c) ring [91]

Polymerization of silicon alkoxide leads to complex branching because a fully hydrolyzed monomer [$Si(OH)_4$] is tetrafunctional. On the other hand, under certain conditions (e. g., low water concentration) fewer than four ligands will be capable of condensation, so relatively little branching will occur.
Polymerization reactions can precede either in acid-catalyzed or base-catalyzed environments.

1.3.2.1 Hydrolysis mechanism

The hydrolysis of silicon alkoxides has been extensively studied by many authors. An excellent review was presented by H. Schmidt [91] in which the role of water and catalysts on hydrolysis mechanisms was pointed out. In addition, the strong influence of ligands (OR) on $Si(OR)_4$ hydrolysis was determined.

R. K. Iler [92] divides the polymerization process into three pH domains: pH<2, pH 2-7 and pH>7. However, regardless of pH, hydrolysis occurs by the nucleophilic attack of the oxygen contained in the water on the silicon atom, as evidenced by the reaction (Eq. 10) of isotopically labelled water with $Si(OC_2H_5)_4$ (TEOS) that produces only unlabeled alcohol in both the acid- and base-catalysed systems [84]:

$$Si - OR + H\text{-}18OH \Leftrightarrow Si\text{-}18OH + ROH \qquad (10)$$

Acid-Catalyzed Mechanism

Under acidic conditions, it is likely that an alkoxide group is protonated in a rapid first step. Electron density is withdrawn from the silicon atom, making it more electrophilic and thus more susceptible to attack from water. This results in the formation of a penta-coordinate transition state with bimolecular nucleophilic type substitution (S_N2) mechanism [37]. The S_N2-type mechanism begins when an electron pair of the nucleophile attacks the electrophilic center. The resulting collision causes a leaving group to be substituted by an incoming nucleophile. The transition state contains both the substrate and the nucleophile. The transition state decays by displacement of an alcohol and the inversion of the silicon tetrahedron, as shown in Fig. 6.

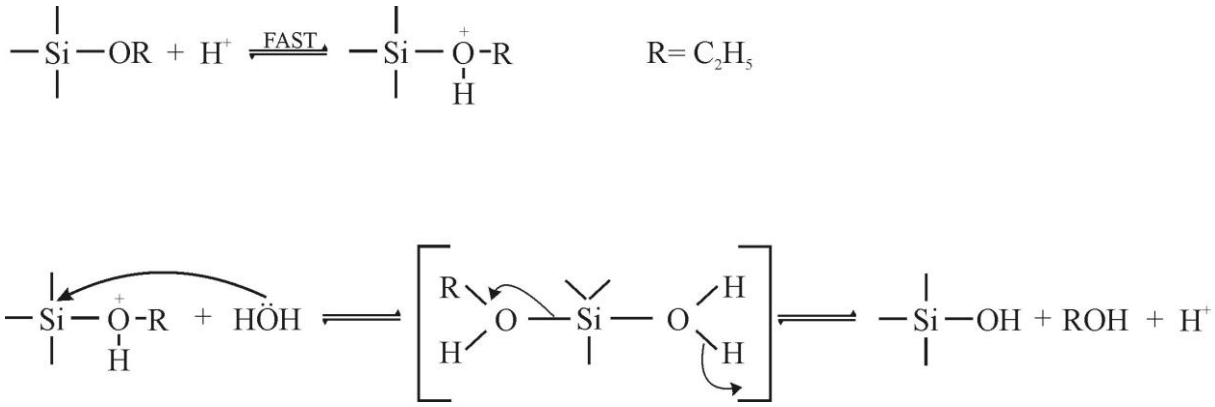

Figure 6: Acid-catalysed hydrolysis [37]

Base-Catalyzed Mechanism

The base-catalyzed hydrolysis of silicon alkoxides proceeds much more slowly than acid-catalyzed hydrolysis at an equivalent catalyst concentration [93]. Basic alkoxide oxygens tend to repel the nucleophile, -(OH^-). However, once an initial hydrolysis has occurred, the following reactions proceed stepwise, with each subsequent alkoxide group more easily removed from the monomer than the previous one [94]. Therefore, more highly hydrolyzed silicones are more prone to attack.

Thus, under basic conditions, it is likely that water dissociates to produce hydroxyl anions in a rapid first step. The hydroxyl anion then attacks the silicon atom. Again, an S_N2-type mechanism has been proposed in which the –OH displaces –OR with the inversion of the silicon tetrahedron, as shown in Fig. 7.

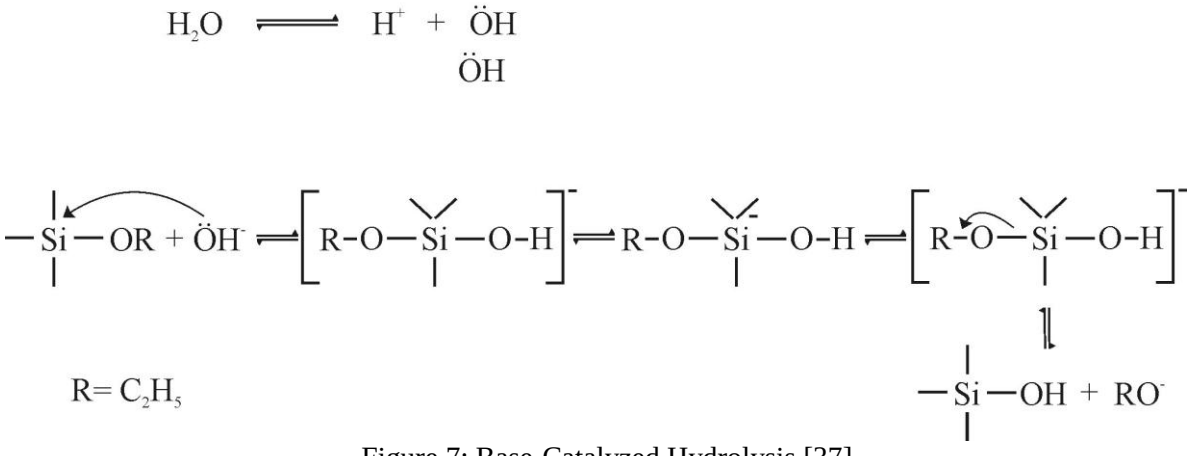

Figure 7: Base-Catalyzed Hydrolysis [37]

1.3.2.2 Condensation mechanism

The formation of siloxane bonds (Si-O-Si) through polymerization occurs by either an alcohol-producing or water-producing condensation reaction. It has been shown by Engelhardt [95] that a typical sequence of condensation products is monomer, dimer, linear trimer, cyclic tetramer, and higher order rings. This sequence of the condensation products requires both depolymerization (ring opening) and the availability of monomers which are in the solution [37].
The rate of these ring-opening polymerization and monomer addition reactions is dependent upon the environmental pH. In polymerization below pH 2, the condensation rates are proportional to the $[H^+]$ concentration. Because the solubility (Fig. 8) of silica is quite low below pH 2, the formation and aggregation of primary silica particles occur together and ripening (growth of a network) contributes little to the growth after particles exceed 2nm in diameter. Thus, the developing gel network is composed of small primary particles [37].

It is generally agreed that between pH 2 and pH 6 the condensation rates are proportional to the $[-OH^-]$ concentrations. Condensation preferentially occurs between more highly condensed and those less condensed species. This suggest that the rate of dimerization is low, however once dimmers forms, they react preferentially with monomers to form trimers, which in turn react with monomers to form tetramers.

Above pH 7, polymerization occurs the same as in the pH 2 to 6 range. However, in this pH range, condensed species are ionized and therefore mutually repulsive.

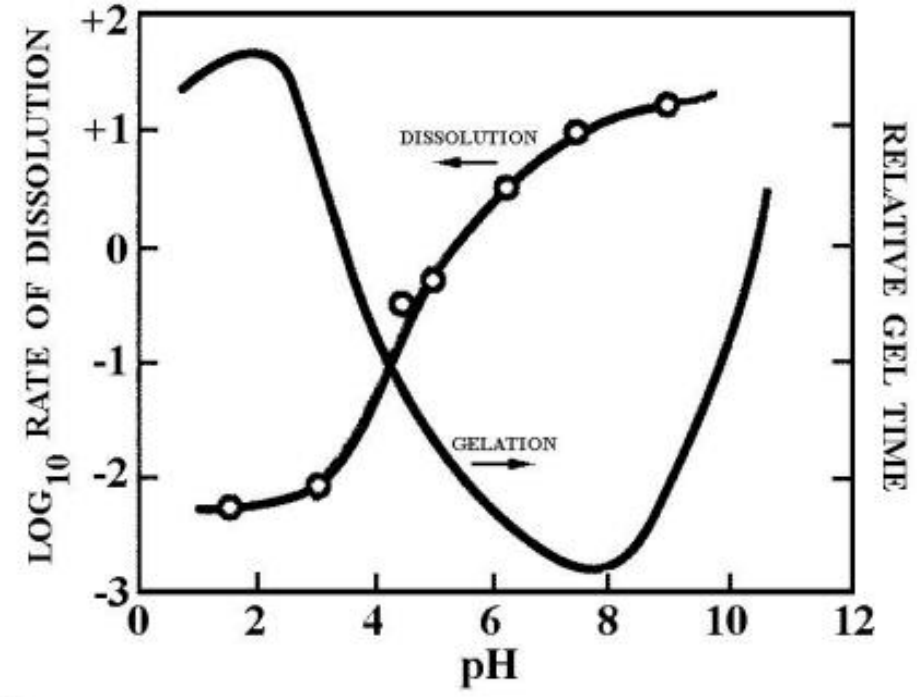

Figure 8: Dissolution rate and relative gel time as a function of pH [37]

Acid-Catalyzed Mechanism

In acid conditions and pH<2.5, silicon alkoxides condense through a two-step S_N2 mechanism. The first step consists in the protonation of the silanol group, which makes silicon more electrophilic and thus susceptible to nucleophilic attack. As a consequence, this protonated silanol combines with another silanol group while liberating an $[H_3O]^+$ ion. The two silicon atoms of the resulting polymer are then linked through an oxo bridge called a siloxane bond. The Si of the intermediary complex of this mechanism, as shown in Fig. 9 is

either tetra or penta-coordinated [96]. The most basic silanols species (silanols contained in monomers or weakly branched oligomers) are the most likely to be protonated. Therefore, the condensation reaction may occur preferentially between neutral species and protonated silanols situated on monomers or the end groups of a chain.

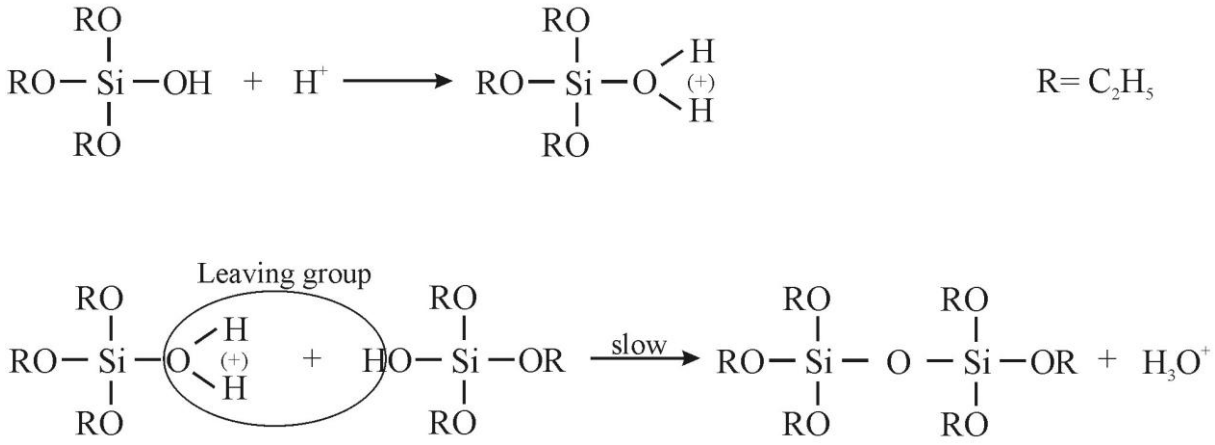

Figure 9: Acid-catalyzed condensation [37]

The rate of the condensation reactions depends on the second step of the mechanism as it is slower than the first one; it is, moreover proportional to the concentration of protons. Hence condensation is a slower transformation than hydrolysis. Furthermore, silanols are protonated more easily at the end of a polymer chain. The polymers obtained are therefore linear with scarcely any branching points.

Base-Catalyzed Mechanism

When the pH>2.5 the silanol groups are deprotonated according to reaction (11):

$(RO)_3 \equiv Si - OH \Rightarrow (RO)_3 \equiv SiO^- + HOH$ (11)

They build siloxane bridges by another S_N2 mechanism that involves two intermediary complexes with penta-coordinated silicons. This corresponds to the reaction in Fig. 10, as proposed by C. G. Swain [97]. When the pH>4 the condensation rate is not only proportional to the concentration of OH^- anions, but also superior to that of hydrolysis.

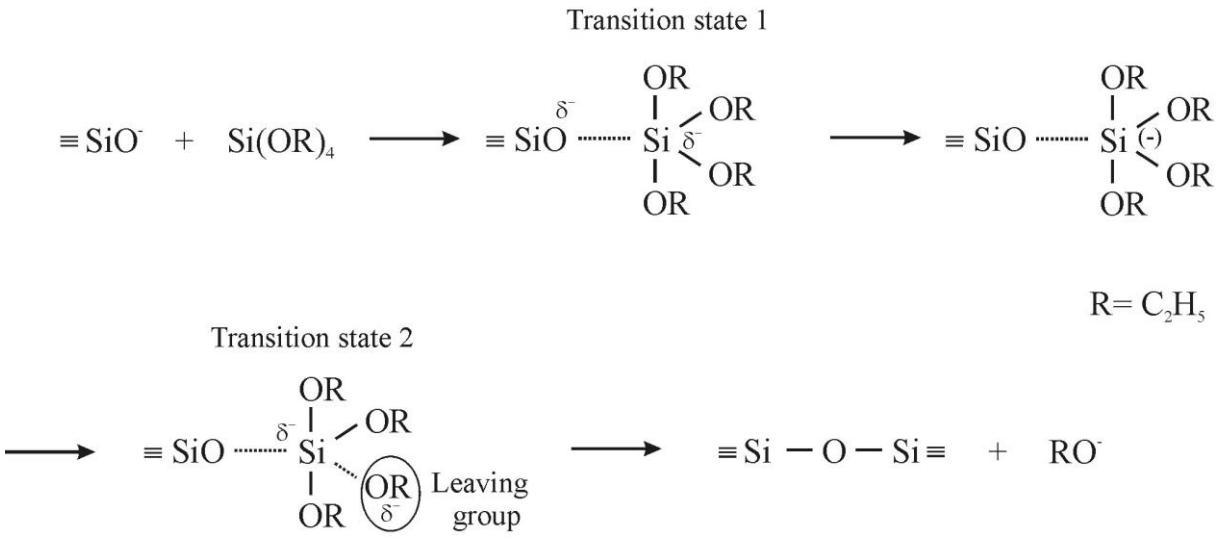

Figure 10: Based-catalyzed condensation [37]

1.3.3 Gelation

Gelation, the transition from a solution into a solid, involves the hydrolysis and condensation of alkoxides. According to Iler [92], sol-gel polymerization occurs in three stages:

1. the polymerization of the monomers to form particles.
2. the growth of particles.
3. the linking of particles into a chain, then networks that extend throughout the liquid medium, thickening into a gel.

Within the context of these stages, many factors affect the resulting silica network, such as, pH, temperature and time of reaction, reagent concentrations, additives, catalyst nature and concentration, $H_2O/Si(OR)_4$ molar ratio (R_h), aging temperature and time. Since it is the relative rates of hydrolysis (k_H) and condensation (k_C) that determine the structure of the gel, it is essential to understand the kinetics of the hydrolysis and condensation reaction and the ratio of the rate constants (k_H/k_C). According to G. Orcel [98] the shape and size of polymeric structural units are determined by the relative values of the rate constant for hydrolysis and polycondensations reactions, respectively. To reduce the particle size, k_H should be larger than k_C. Fast hydrolysis and slow condensation favour the formation of linear polymers. Vice versa, i.e., slow hydrolysis and fast condensation, lead to larger, bulkier and more ramified polymers.

The dominate factor in controlling the hydrolysis rate is the electrolyte concentration. The k_H increases linearly with the concentration of H^+ or H_3O^+ in acid media and with the concentration of OH^- in basic media. As already mentioned, acid or base catalysts can influence both hydrolysis and condensation rates and the structure of the condensed product. Acids serve to protonate the negatively charged alkoxide groups, enhancing the reaction kinetics by producing a good leaving group. The relative ease of the protonation of different alkoxide ligands (Fig. 11) can influence the condensation pathway, as demonstrated:

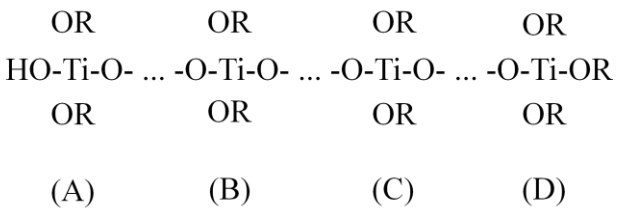

Figure 11: Partially hydrolyzed polymer [37]

The δ(OR) for the sites A-D calculated from the partial charge model are listed in Table 3.

Table 3: Charge distribution according to the partial-charge model within titanium oxo-polymer [37]

Site	δ(OR)	δ(OR)
A	−0.01	0.70
B	0.22	0.76
C	0.04	0.71
D	-0.08	0.68

The tendency of protonation decreases in the order D > A > C > B, which reflects the electron-providing power of ligands, which decreases as alkoxy, hydroxo, oxo. Therefore, acid-catalyzed condensation is directed preferentially toward the ends rather than the middles of the chain, resulting in more extended, less highly branched polymers [37].

As result, under acid-catalyzed conditions, they yield primarily linear or randomly branched polymers, which entangle and form additional branches resulting in gelation. On the other hand, silicon oxide networks derived under base-catalyzed conditions yield more highly branched clusters which do not interpenetrate prior to gelation and thus behave as discrete clusters (Fig. 12).

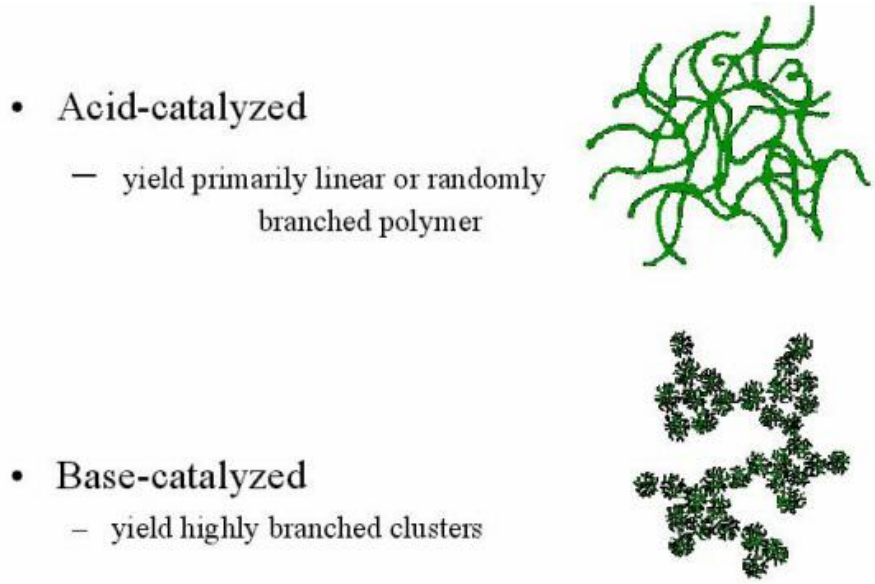

Figure 12: Gel structure in acid conditions and basic conditions [37]

The nature of the solvent and the temperature dependence of the reactions also have an effect on the relative rates of hydrolysis (k_H). The k_H varies in the different solvents as follows: acetonitrile > methanol > dimetylformamide > dioxane > formamide. The k_H for acetonitrile is about 20 times larger than the k_H for formamide [99]. An additional increase in k_H occurs when the temperature varies from 20°C to 45.5°C [100].

As already mentioned, the alkoxy groups on the silicon atoms also influence the relative rate of hydrolysis (k_H). As a general rule, the longer and the bulkier is the alkoxide group, the slower is the rate of hydrolysis [101]. For example, in the case of hydrolysis of $Si(OR)_4$ the k_H are listed in Table 4 [91].

Table 4: The k_H for acid hydrolysis of different alkoxysilanes [91]

R	k_H 10^2 (L mol^{-1} s^{-1} $[H^+]^{-1}$)
C_2H_5	5.10
C_4H_9	1.90
C_6H_{13}	0.83
$(CH_3)_2CH(CH_2)_3CH(CH_3)CH_2$	0.30

The amount of water for hydrolysis has a dramatic influence on gelation time (t_G). M. W. Colby [102] reported that for an R_h (moles of water / moles of TEOS) of 2, t_G is about 7 h and decreases to 10 min for R_h of 8. In addition A. Aelion reported that an increase of the R_h ratio from 1.86 to 3.72 induces k_H to increase from 0.042 to 0.059 ^{3} L mol^{-1} s^{-1} $[H^+]^{-1}$[103]. When R_h << 4 the alcohol-producing condensation is favoured, whereas the water-forming condensation reaction is favoured when the R_h >> 4. The excess water is expected to additionally promote hydrolysis.

In film coating the viscosity of the solution becomes a particularly critical parameter. There are many examples of the application of controlled hydrolysis to obtain a preferential molecular structure and a suitable viscosity of the solution in order to improve spinnability and coatability [104-106]. The aging time of sols is related to the viscosity. With time the viscosity of the sol increases. According to P. Fuierer [107] such an increase in the viscosity has an indirect effect on the final microstructural development of the deposited thin films. The viscosity of sols can also vary by the addition of a different additive, for example, a chelating additive, drying control chemical additive, etc, or by the concentration of the precursors used in the sol-gel process. It is preferable that for thin film deposition the viscosity of the sol varies from 1 to 10 mPas.

D. P. Partlow and B. E. Yoldas [108] have suggested that a gel can be created in two ways. In the first case, as the concentration of polymeric species increases upon removal of the solvent, the probability of crosslinking between the polymeric chains increases. When sufficient crosslinking occurs, a sol-gel transition is observed, beyond which the viscosity increases abruptly. Ageing of the solution, which allows the hydrolysis and condensation reaction to proceed, is another way to promote the polymerization reactions often catalyzed by acid or base. A network is built up as the polymerization reaction continues. Thus, polymeric gels are formed. In general, it can be said that the sol becomes a gel when it can support a stress elastically. This is typically defined as the gelation point or gelation time t_G.

The interaction between the polymeric species and the definition of the gelation point was studied by small-angel-X-ray scattering (SAXS). In this study the gelation process was defined by the particle size formed during gelation. The radius of the primary particles, R, was between 1 and 2 nm and can was modelled by rings and chains of three to four silica tetrahedra [98]. The secondary particles had a radius R of 5 – 20 nm, depending on the experimental conditions. Therefore, the gel structure is composed of different units, primary particles of about 2.0 nm diameter that agglomerate in secondary particles of about 6.0 nm diameter, as shown in Fig. 13. Gelation occurs when the secondary particles are linked to each other, forming a three-dimensional network across the sample.

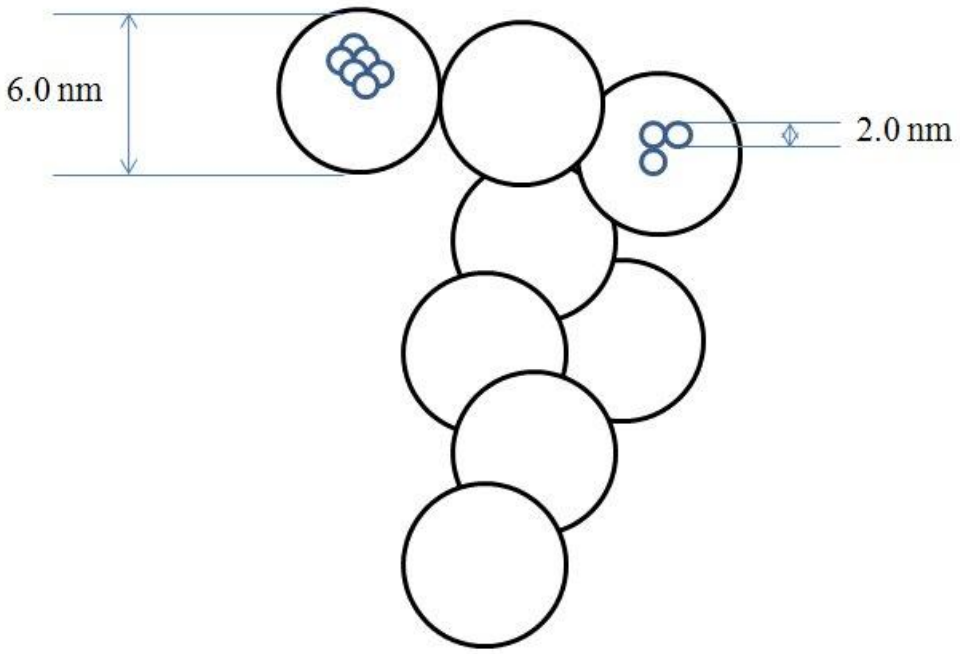

Figure 13: Schematic representation of primary and secondary particles in a TEOS-based alkoxide gel

1.4 Coating deposition

According to Cohen [109], some two dozen methods are available for applying a liquid coating to substrates; the best choice depends on several factors, including solution viscosity, desired coating thickness and coating speed. Sol-gel coatings are primarily deposited by spin and dip coating; however, spray coating [110] and ultrasonically pulverized aerosol spray [111] have also been tried. In these methods, the process of creating a layer of coating liquid and the drying of that layer overlap. Drying early in the process, before solidification, increases the concentration of the precursors and therefore accelerates the hydrolysis and condensation reactions. Drying leads to the capillary pressure and stresses; these collapse the porous gel structure.

1.4.1 Deposition methods

In **dip coating**, a substrate is immersed in a coating solution and withdrawn at a constant rate. Fig. 14 shows the schematic steps in a batch process and a continuous dip coating step [37].

Preparation by the dip coating technique may be divided into four stages:

1. the choice of the substrate,
2. the thin layer deposition,
3. the film formation,
4. the densification through thermal treatment.

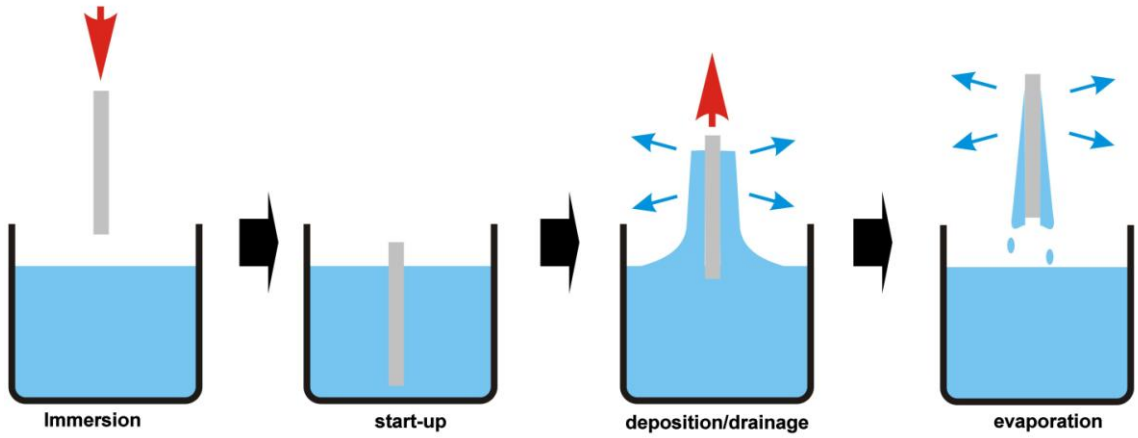

Figure 14: Stages in dip-coating process

According to a standard procedure shown in Fig. 14, the substrate is immersed in the coating solution and then during withdrawal, a layer of liquid is entrained. As the layer is drawn upward, viscous drag and gravitational forces determine the film thickness (h):

$$h = C_1 (\eta.U/\rho.g)^{0,5} \quad (12)$$

where η is the viscosity, U the withdrawal speed, ρ the density of the coating solution and C1 is a constant (approximately 0.8 for Newtonian fluids).

Spin coating is a combination of four stages, as shown in Fig. 15[37]:

1. the deposition,
2. the spin-up,
3. the spin-off,

4. the evaporation (which occurs during all stages).

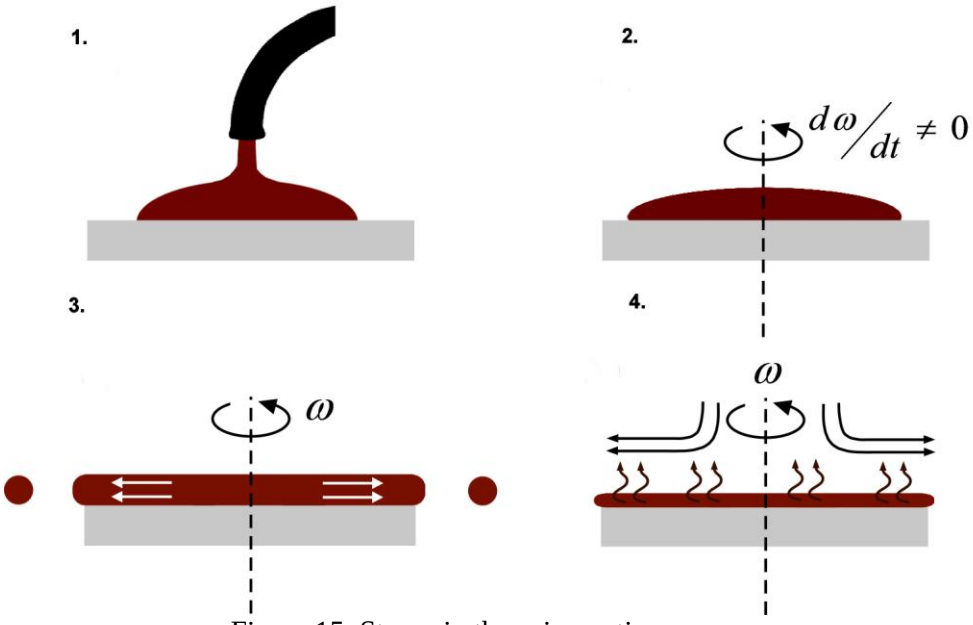

Figure 15: Stages in the spin-coating process

After delivering the liquid to the substrate, centrifugal forces drive the liquid across the substrate (during spin-up). The excess solution leaves substrate during spin-off. When flow in the coating is no longer possible, evaporation takes over as the main means of thinning the coating. Spin-cast layers have nearly uniform thickness if the viscosity of the solution is not dependent on the shear rate (i.e., Newtonian) and if the evaporation rate is independent of the position. Analytical expressions for the coating thickness have been derived. The final thickness (h) of a spin-cast layer is given by Eq. 13:

$$h = (1-\rho_A/\rho_A)\,(3\eta e/2\rho\omega^2) \qquad (13)$$

where ρ_A is the mass of volatile solvent per unit volume, ρ_A its initial value, ω the angular velocity; η the solution viscosity, and the evaporation rate. The equation demonstrates that the coating thickness can be controlled by adjusting the solution properties, and the deposition conditions.

1.4.2 The influence of the substrate on thin film preparation

The function of the substrate is to provide the base onto which the coatings are deposited. In addition, the substrate provides the necessary mechanical support and rigidity. The criteria for the substrates used to grow crack-free coatings are:

1. low surface roughness,
2. coefficient of thermal expansion matched with coating,
3. lattice parameter matched with coating
4. good mechanical strength,
5. optimal thermal conductivity,
6. inertness, or chemical stability,
7. low cost,
8. good uniformity.

The characteristic of ceramics coatings are very sensitive to the characteristics of the substrate. For example, I. Kawayama et al. [112] studied the influence of the lattice mismatch of substrates (MgO, $MgAl_2O_4$, $SrTiO_3$, $LaSrAlO_4$) and $SrBi_2Ta_2O_9$ (SBT) thin films on the

surface morphology of coatings. They observed that the surface morphology changed by using a different substrate. SBT thin film on MgO substrate, with a lattice mismatch of 7.6 %, contains islands, while on the $MgAl_2O_4$ substrate, with a lattice mismatch of 3.3 %, the SBT thin film is contains flat terraces.

In addition, the surface roughness of the coating has a direct influence on interface between the coatings and the electrodes and in this way influences the electrical or the optical properties of the coatings [113]. K.-S. Hwang et al. [114] studied the roughness of $LaNiO_3$ (LNO) thin films on various substrates ($LaAlO_3$ (100), $SrTiO_3$ (100), MgO (100) and sapphire (0001)). They observed that LNO thin films with a low surface roughness (6-8nm) were obtained by using $LaAlO_3$ and $SrTiO_3$ substrates having a similar lattice parameter and thermal expansion coefficient. Whereas, the LNO thin films on MgO and sapphire substrates contain abnormal grain growth, which resulted in high surface roughness (30-42 nm).

A. Simões [115] studied the influence of the thermal expansion coefficient and heat capacity of a silicon- and platinum-coated silicon substrate on the morphology of PLZT films. Crack-free thin films were obtained on silicon substrate, while on the platinum-coated silicon substrate some non-uniform, white regions were observed on the surface of the PLZT thin films. According to the author of [115] these defect were caused by differences in thermal properties (thermal expansion coefficient and heat capacity) of platinum ($9 \cdot 10^{-6}$ $°C^{-1}$ and 0.1338 J/g°C) and PLZT film ($5.6 \cdot 10^{-6}$ $°C^{-1}$ and 0.1045 J/g°C). These lead to a higher volatilization rate of the organic materials and compounds with a low vaporization temperature, like PbO. In contrast, the silicon substrate has a lower thermal expansion coefficient and heat capacity ($3 \cdot 10^{-6}$ $°C^{-1}$ and 0.0711 J/g°C) than the PLZT thin film. Therefore, the formation of a homogeneous surface of the PLZT thin film appeared.

1.5 Drying

Once we succeed in going from step one, forming a solution, through step two, gelation, the third step is drying. Drying is the term used for the removal of the solvent. The drying rate depends on the rate at which volatile components diffuse to the free surface of the coating and the rate at which the vapour is transported away in the gas. For example, at a high airflow rate, the external transport is fast so that the internal resistance (from the diffusion in the coating) controls the overall drying rate. The stages of drying are illustrated schematically in Fig.16 [116].

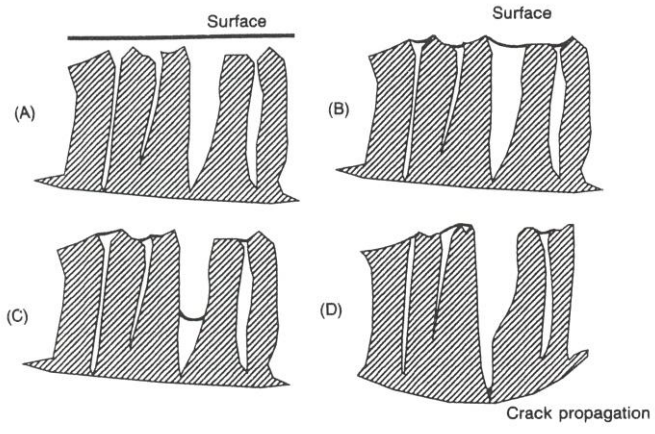

Figure 16: Stages in drying of a gel [116]

According to Yi et al. [116], the gel consists of two phases, the network solid phase and connected pores filled with liquid phase. In the initial stage the surface of the gel is covered

with liquid phase (Fig. 16(A)). With the evaporation of the liquid phase the solid phase is exposed (Fig. 16(B)). Since the solid network is wetted by the liquid phase, the liquid phase tends to cover the entire solid surface and a capillary force will be imposed on the solid network. The yielding gel network allows the gel to shrink under capillary force during liquid evaporation. As the gel shrinks, its stiffness increases because the solid network is becoming more tightly bound. When the gel is too stiff to contract under the capillary force, shrinkage stops and the meniscus of the liquid phase in the pores at the surface begins to recede into the interior of the gel. The menisci in the bigger pores have a greater radius of curvature so that the liquid phases in the bigger pores have a higher vapour pressure and therefore evaporate faster. If the bigger pore is connected with some smaller pores, the liquid in the bigger pore will flow to the smaller pores to compensate for liquid evaporated from there, since the liquid phase in the smaller pores is subjected to a greater capillary force. Therefore, the menisci in the bigger pores recede farther into the body so that bigger pores dry much faster, as shown in Fig. 16(C). When the bigger pores are dry, the interior wall of the bigger pores is not subject to the surface tension of the liquid, while the smaller pores around the bigger pores are still filled with liquid phase. The region with the smaller pores shrinks under the surface tension and usually causes a stress concentration at the bottom of the bigger pores. The bigger pore acts as a microscopic flaw and, when the stress concentration of the pore is great enough, a macroscopic crack will develop, as shown in Fig. 16(D). This is the reason why the gels with different pore sizes are easily cracked during drying. [116]

According to the literature [117] only gel films with a thickness less than 1 μm can be dried on the substrate without cracking. Since the stress concentration is caused by the capillary force and the variation of the pore size, the stress concentration should be reduced by limiting the interaction between the liquid phase and the pore walls, and by methods which reduce the variation of the pore size. Zarzycki [118] and Brinker et al. [119-120] have investigated this mechanism very thoroughly on SiO_2 gels and glasses. The chemical interactions of the liquid phase with the pore walls are based on the reaction of the pore wall OH group with water forming hydrogen bonds. The interaction depends on:
- the pore size, small pores are more efficient for interaction than large ones,
- the temperature, increases diffusion without increasing capillary forces,
- the chemical state of pore walls, number of OH groups or number of other hydrophilic group,
- the pore shape.

The stress occurring during drying could be reduced by the use of a surfactant [121], hypercritical drying and drying control chemical additive (DCCA) [81, 122]. A surfactant decreases the capillary force and in this way the stress concentration is reduced. In hypercritical drying, the film is dried by heating the gel under pressure to a point above the critical temperature and the pressure of the solvent. In this process there is no capillary force. The hypercritical dried gel has the same volume as the sol from which it is made. The DCCA, such as formamide, oxalic acid and etc., reduces the rate of hydrolysis and condensation reaction and produces larger and more uniform pores by interconnecting the gel structure.

The evaporation of the solvent and other volatiles influences the reaction rates in the coatings dynamic, which are changing inside the coating with time and depth. Cairncross et al. [123, 124] developed a model to investigate the competition between drying and reaction in a sol-gel coating. Their model considers the changes in thickness, compositions and structure as a layer of Si- alkoxide based coatings solution dries and reacts. The results of the model show the profound effect of drying on gelation. Fig. 17 a) shows the molecular weight distribution through the thickness of a coating and the thickness as a function of drying time (Fig. 17b)

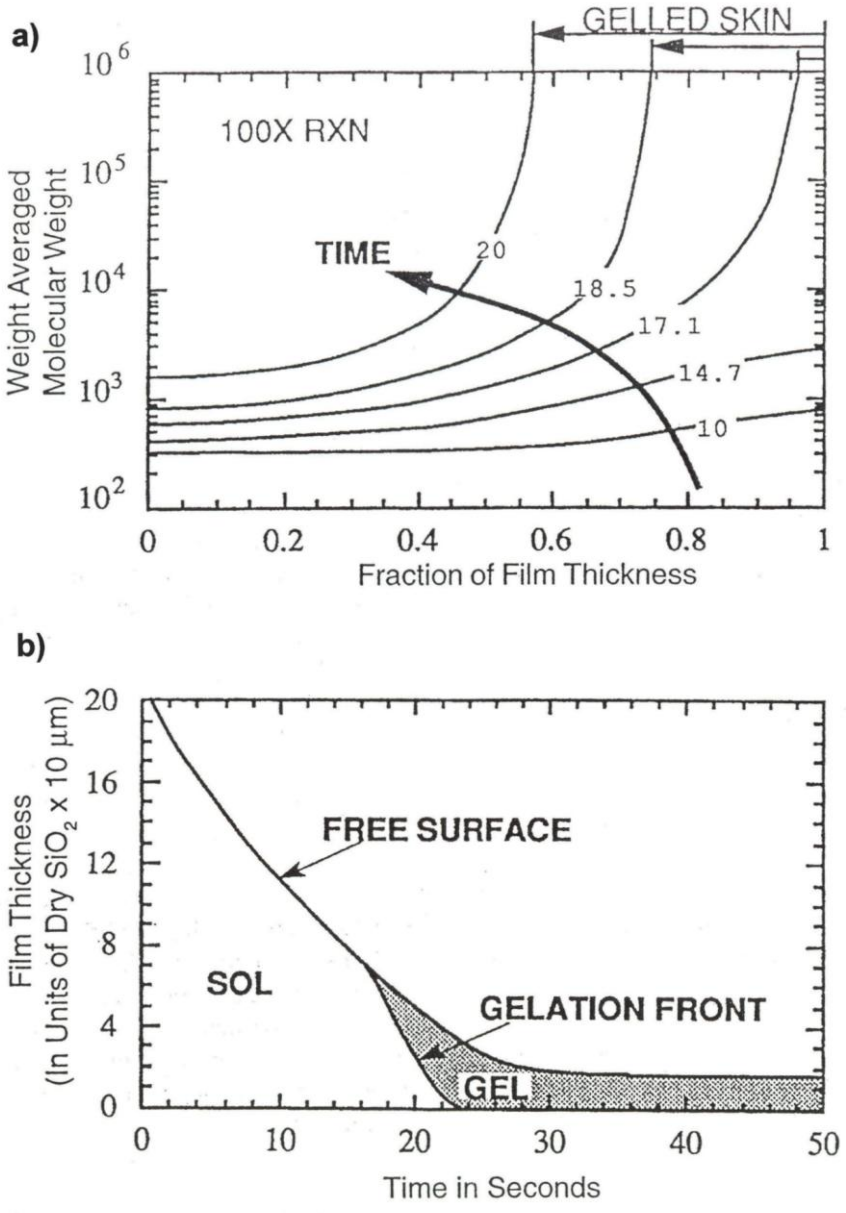

Figure 17: Gelation of drying sol-gel films from TMOS-based solution: a) molecular weight distribution for different elapsed times and b) change in film thickness with elapsed time [123]

Early in the process, the molecular weight is fairly constant; however, as time goes by the molecular weight at the coating surface grows. Drying increases the concentration of the alkoxide precursors at the surface, accelerating the reaction there. Eventually, the molecular weight diverges to infinity and a gel is formed. For this combination of reaction and drying conditions, the coating surface gels first, forming a skin. Fig. 17 b) shows how a gelation front propagates down from the surface to the substrate as the coating thins.

Fig. 18 shows the effect of coating thickness and drying rate on gelation phenomena in a coating.

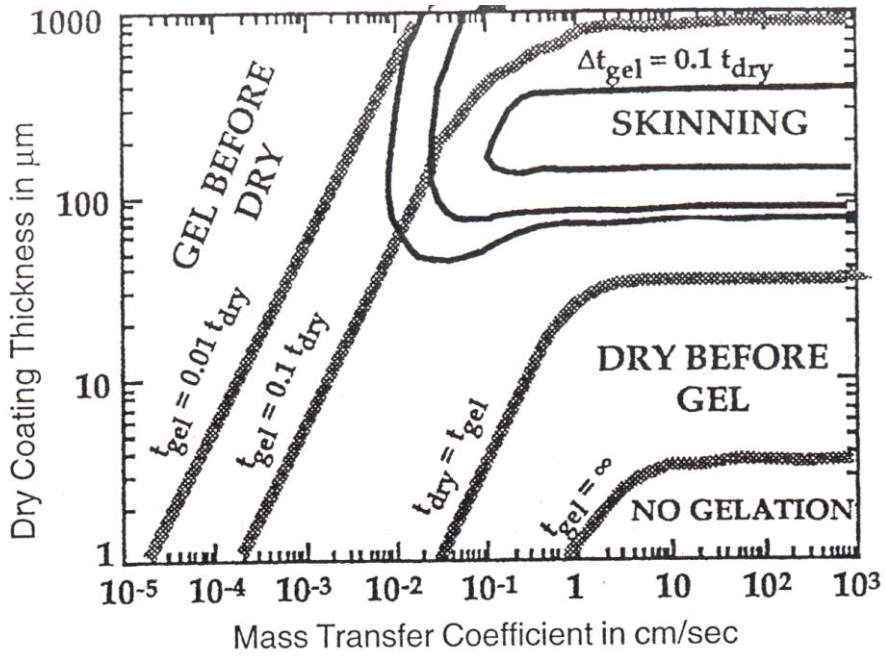

Figure 18: Drying regime map calculated for sol-gel coating from a TMOS-based solution prepared over a range of coating thicknesses and drying conditions [124]

When the drying rate is low or the coating is thick (the top and left of the diagram in Fig. 18), reactions that lead to gelation occur quicker than evaporation, and the coating gels before it dries. When the reactions are slow or the coating is thin (the bottom and right of the diagram in Fig. 18), drying is faster and less time is available for the reaction; therefore, these coatings dry before they gel or do not gel at all if water is evaporated. A coating that gels before much drying has taken place traps a large amount of solvent in the gelled structure and is likely to be porous after the drying is complete. By contrast, the coating that dries faster than it reacts will likely be denser because less solvent will need to be removed from the solidified structure.

According to Brinker [37] the competition between the evaporation and condensation reactions is establishing the microstructure development of the coatings. Evaporation and the attendant capillary forces compact the structure, while the condensation reactions stiffen the gel network and cause greater resistance to flow. The relative rates of these two processes are influenced by the properties of the precursor solution and the deposition conditions. Factors which increase the condensation rate in bulk gels should have a similar effect on the coatings. For example, greater amounts of water and the use of a base additive produce coatings which have higher condensation rates. This coating becomes rigid, gels before evaporation, compacts the structure, and is therefore more porous.

Cracks can develop at any stage of the process and limit the coating thickness. Whether or not a crack forms depends on the magnitude of the stress, the thickness of the coating and the material’s properties.

1.6 Thermal treatment and development of a crystalline microstructure of thin films

The as-deposited coating is porous, amorphous and contains residual organics material. The final ceramic thin film is organic free, dense and crystalline. Therefore, thermal treatments must impart tremendous physical and chemical changes.

To obtain the desired oxide phase, solvent remaining entrapped within the pore structure of the thin film and the organic compound associated with the gel network must be removed.

Typically, the oxide phase is obtained by heat treatment. Accompanying the conversation into the oxide phase, the rearrangement of the gel network through a variety of bond reorganizations and structural relaxation processes must take place. A proposed gel structure of the alkoxide salt method is shown in Fig. 19 [125].

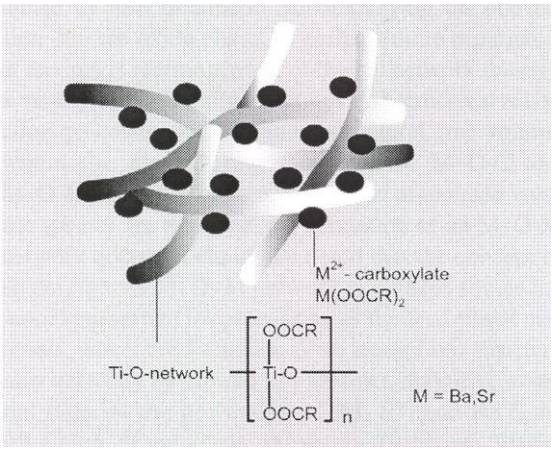

Figure 19: Ti-O network with absorbed strontium or barium carboxylate molecules [125]

During the process the M-O-C and M-O-H bonds are broken, and as associated volatile species are removed, the formation of the M-O-M network occurs. The general reactions that take place during the transformation include:

- thermolysis (formation of volatile organic species without oxygen),
- pyrolysis (formation of volatile organic molecules such as CO, CO_2...),
- dehydration (elimination of OH groups from the network as H_2O).

The most significant changes in the thin-film thickness and composition occur while the thin film is still amorphous and undergoing a thermal treatment in the range of room temperature up to 300°C. The heat treatment process can be divided in several regions as shown Fig. 20 [126].

From room temperature to about 150°C (region I) weight loss and shrinkage occur due to the removal of the adsorbed water and structural relaxation, respectively. The structural relaxation is the removal of free volume by bond restructuring. In region II continued condensation reactions and structural relaxation are responsible for the shrinkage, while weight loss results from the pyrolysis of residual organics, including condensation by-products, un-hydrolyzed alkoxy groups, and organic groups such as acetate. In region III, shrinkage occurs without weight loss. For some compositions, crystallization occurs in the same temperature regime.

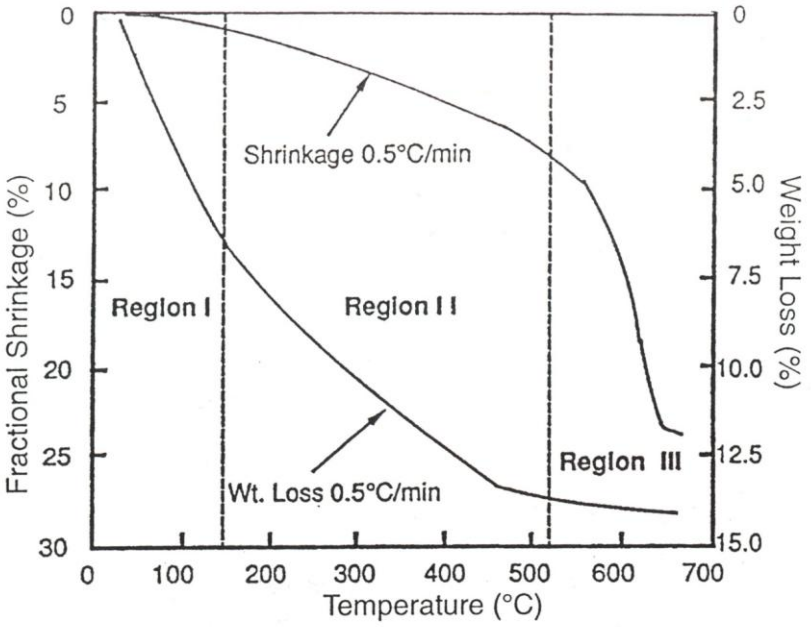

Figure 20: Structural evolution and weight loss in borosilicate gel [126]

Two approaches are commonly used to complete the transformation of the as-deposited coating into the crystalline ceramic:

- Two-step process. In this process the as-deposited coating is subjected to separate organics species (pyrolysis/thermolysis) prior to crystallization at higher temperatures. During the first step of the process, the coating is typically placed on a hot plate held at 200 to 400°C for the burnout of the organic species. It has been proposed that his approach allows for the removal of the organic constituents prior to the collapse of the amorphous network, thus minimizing cracking.
- One-step process. In this process the coating is heated directly to the crystallization temperature, which results in both organic removal and crystallization. Due to the single-step nature of this approach and the use of relatively high temperatures (700°C), a number of complex, and potentially overlapping, processes may occur during this process.

It is important that coatings adhere to the substrate during all the processing steps. The main adhesion mechanism can be explained by the reactions of the M-OH groups on the substrate surface with M-OH or M-OR groups of the gel coatings. In order to enhance the adhesion of the films to the substrate, oxidation or the introduction of OH groups onto the substrate surface is necessary.

Since pyrolyzed thin films are typically amorphous, the film crystallization process is described by the individual process of nucleation and growth. The theoretical description of nucleation and growth in solution derived coatings is analogous to that used to describe crystallization in traditional glasses, and the characteristics of the nucleation and growth process serve to define the resulting microstructure. Namely, thin films where only interface nucleation of the final crystalline phase occurs are show a columnar cross-sectional microstructure, whereas those in which nucleation occur throughout the film have a non-columnar cross-sectional microstructure. From a thermodynamic perspective, it has been demonstrated that the driving force that governs the transformation from amorphous (pyrolyzed) thin film into crystalline ceramic can play a significant role in defining the active nucleation events, and thereby, the film microstructure [127]. The diagram shown in Fig. 21, originally proposed by R. Roy [128], demonstrates the differences in free energy between the solution derived amorphous thin film and the crystalline ceramic phase.

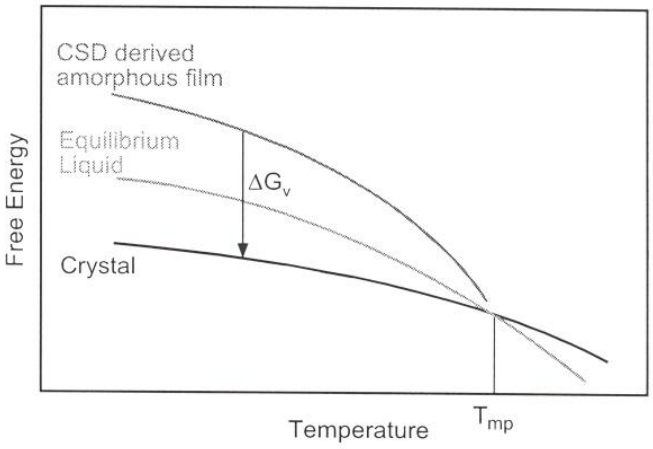

Figure 21: Schematic diagram of the free energies of a CSD-derived amorphous thin film, the ideal supercooled liquid, and a crystalline phase [128]

While this diagram (Fig. 21) does not necessarily provide insight into the transformation pathway the thin film undergoes, it is useful in understanding the role that driving force $-\Delta G$ (the energy difference between the amorphous and crystalline states) can have on the transformation process, and thus, the final microstructure of the ceramic thin film. Consideration of the driving force is important since it influences the barriers for the nucleation of the crystalline phase at different locations (substrate interface, surface, bulk) within the thin film, as well as the nucleation rate. The thermal energy available (via heat treatment during the crystallization anneal) to overcome these different nucleation barriers defines which events take place, and thus the resulting thin-film microstructure. Nucleation can occur as a homogeneous process in which nuclei form throughout the volume. For the coating, the volume is limited and much of the volume is not far from the surface and the interface with the substrate. In heterogeneous nucleation, the nucleation occurs preferentially on imperfections, substrate surface and intentionally added nucleating agents. After the formation of stable nuclei, the crystal growth continues the transformation process. The growth rate depends mainly on the rate at which an atom can cross the boundary between the amorphous and crystalline phase.

The chemical composition of the oxide coating, the solution chemistry, the coating conditions and thickness, the substrate or buffer layer, and the thermal treatment conditions can have a significant effect on the thin-film microstructural development.

Many researchers have studied the effects of processing variables on microstructure development.

L.B. Kong [129] reported that prolonged heating time for $Bi_4Ti_3O_{12}$ thin films did not promote grain growth (T=550°C, 100 nm), while heating at higher temperatures gave a larger grain size (T=600°C, 150 nm; T=650°C, 210 nm).

V. Joshi and M. L. McCartney [130] found that the use of lower R_h leads to smooth, dense polycrystalline thin films, while higher R_h results in more porous coatings with a larger grain size.

J. Zhai and H. Chen [131] studied the influence of sol concentration on the microstructural development of (Ba, Sr) TiO_3 thin films. In a diluted solution the single layer is very thin (e.g. ~8.5 nm for 0.1 M) and the rate of the condensation reaction is very slow, therefore local grain-on-grain, or homoepitaxy, grown at the interface between the thin film and the substrate would occur, thus resulting in highly preferred orientation. On the other hand, when the sol concentration is higher, the film becomes thicker (~30 nm for 0.3 M, ~110 nm for 0.6 M)

because of the large amount of precursor molecules. The rate of the condensation reaction is higher; consequently, random nucleation would occur, leading to a polycrystalline orientation. The grain size of the (Ba, Sr) TiO_3 thin film has increased with a decreasing of the sol concentration (30 nm for 0.6 M, 150 nm for 0.1 M).

D. J. Eichost [132] showed that the grain size of a lithium niobate thin film was larger for a thin film prepared from Li-Nb methoxyethoxide as compared with the thin films prepared from Li-Nb ethoxide sols. The difference in the microstructure could be due to a difference in the nucleation rate with the different alkyl group.

The substrate or buffer layer has a tremendous influence over the crystallization, orientation and microstructural development. S. Song [133] studied the effect of the buffer layer on the microstructural development of $BaTiO_3$ (BT) thin films. It was found that the grain size of the BT thin films deposited on LSCO-buffered Pt substrates was larger than that of the BT thin films deposited on Pt substrates, and the grain size of the BT thin films increased with an increasing of the LSCO buffer layer thickness from 10 nm to 150 nm. This was attributed to the different interaction strength between the substrate and deposited atoms, and the different lattice mismatch between the substrate and BT thin films, which directly influences the nucleation and growth dynamics. Atomic force microscopy was also used to estimate the surface roughness of the thin films. The average roughness parameter (R_a) was increased by increasing the buffer layer thickness. The parameter of the film surface roughness is extremely important for device performance since the dielectric properties depend not only on a well-defined microstructure, but also on the quality of the electrode-film interface. I. P. Koutsaroff [134] showed that the substrate material influences the kinetics of the film growth having a different thermal conductivity, specific heat and emissivity. A description of the grain growth in thin films requires a consideration of the dimensionality of the growth, substrate interfacial energy and surface energy [135]. For thin films, three dimensional normal growths can occur only when the grain size is smaller than the film thickness. Normal grain growth ceases in thin films when the size approaches the thickness, when the grains become columnar and all the grain boundaries intersect the top and bottom surfaces of the film.

2. Aim of the work

$Bi_{12}SiO_{20}$ (BSO), a member of the sillenite family, is an interesting material for a wide range of applications. Recently, however, sillenites have begun to be considered as useful dielectric materials in the field of electronics. Bulk BSO has been extensively studied by Valant and Suvorov [9, 10]. They evaluated the dielectric constant and the quality factor in the microwave region (5.5 GHz) to be 37.6 and 8100, respectively. In addition, the temperature coefficient of the resonant frequency is -20 ppm/K. Even though much work has been done on bulk BSO ceramics, only little attention has been given to thin films. Therefore, the focus of this thesis was on the preparation and characterization of BSO thin films prepared by the sol-gel method.

The first part of this thesis was the optimization of the synthesis parameters that led to the formation of dense BSO thin films. The characteristics of a particular sol-gel-derived thin films are related to a number of factors that affect the rate of hydrolysis and the condensation reactions of alkoxide, such as the pH of the sol, the stability of the sol, the reagent concentrations, the solvent, the H_2O/Si molar ratio (R_h), the addition of DCCA or chelating agents, the viscosity and aging of sols, which are believed to have a pronounced effect on the microstructural development of BSO thin films. Moreover, the drying and heat treatment of the thin film are also parameters that influence the microstructural development. Thus, by controlling these factors, it is possible to vary the microstructural development of BSO thin films.

For the application of BSO thin films in electronic devices, it is important to determine their dielectric properties. It was expected that the dielectric properties of BSO thin films, due to the size effect of the samples and the dielectric constant (ε = 37.6), will be difficult to measure. Therefore, part of the attention of the thesis was a focus on the problems of evaluating the dielectric properties of BSO thin films and selecting the optimal measurement configuration.

The results obtained during this thesis study are an important contribution to the interpretation of the capability of BSO thin films for applications in electronics technology.

3. Experimental work

The synthesis of the BSO thin films proceeds in several stages (Fig. 22):

1. selection of precursors, solvents and additives,
2. sol synthesis,
3. thin-film deposition,
4. heat treatment.

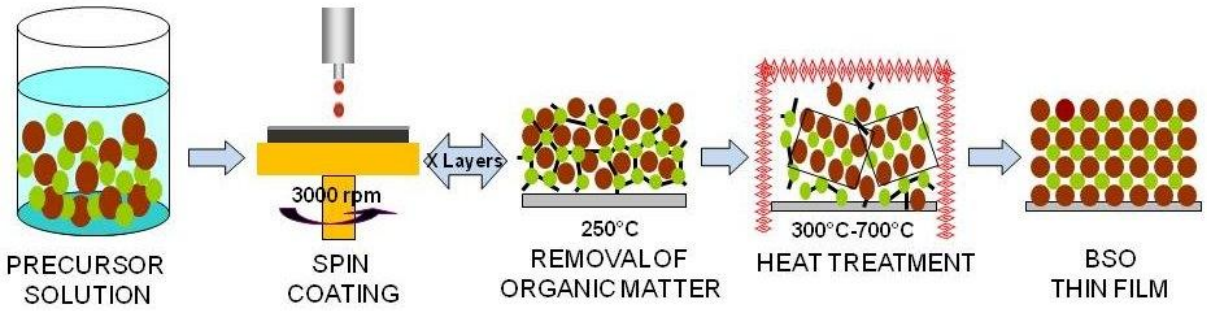

Figure 22: The synthesis scheme of sol-gel-derived BSO thin films

3.1 Selection of precursors, solvents and additives

In this thesis, for the bismuth containing compounds the selection of precursor was critical since bismuth alkoxide, $Bi(OR)_3$ (R= $-C_2H_5$ or C_3H_7) has been found to show a lack of reactivity towards a variety of metal alkoxides. Moreover the costs for an all-alkoxide method are also a problem, since some alkoxides may be very expensive. Therefore, to reduce the possibility of phase separation during hydrolysis or thermal treatment and to lower the production costs, a salt substitute for bismuth alkoxide was used.

In the alkoxide-salt method the alkoxide and salt are used as source for metal elements. The term salt basically refers to carboxylates but also includes the use of nitrate, sulphates, carbonates and hydroxides. In this thesis we used bismuth nitrate as a source for bismuth since it is commercially available and cheap. For the source of silicon elements a silicon alkoxide was used. To optimise the solubility and viscosity in order to obtain high quality thin films, we used acetic acid as the main solvent in combination with an alcohol. The chemicals used for the BSO sol synthesis are given in Table 5.

Table 5: Chemicals used in BSO sol-gel synthesis

Chemical	Chemical formula	Function	Producer
Metal alkoxide	$Si(OC_2H_4)_4$ (tetraethylorthosilicate)	Ceramic precursor	Alfa Aesar (98%)
Metal salt	$Bi(NO_3)_3 \cdot 5H_2O$ (bismuth nitrate penta hydrate)	Ceramic precursor	Alfa Aesar (98%)
Solvent	CH_3COOH (glacial acetic acid) $CH_3CH_2OCH_2CH_2OH$ (2-ethoxyethanol)	Diluents, Solvent, Decreases viscosity and concentration of sol	Alfa Aesar (99.7%) Alfa Aesar (99%)
Stabilizer agent	$H_2NCH_2CH_2OH$ (ethanolamine)	Decreases hydrolysis and condensation rates, Influences molecular structure	Alfa Aesar (98%)
Drying control chemical additive (DCCA)	$HCONH_2$ (formamide)	Decreases hydrolysis and condensation rates	Alfa Aesar (99%)

3.2 Sol synthesis

Sols were synthesised with three different molar ratios $R_h = [H_2O] / [TEOS]$:

1. sols with molar ratio R_h 60,
2. sols with molar ratio R_h 5,
3. sols with molar ratio R_h 60 using DCCA (drying control chemical additive).

3.2.1 Sols with molar ratio R_h 60

Bismuth nitrate $Bi(NO_3)_3 \cdot 5H_2O$ was dissolved in acetic acid CH_3COOH at 40°C with a constant stirring rate. The stoichiometric amount of tetraethyilorthosilicate $Si(OC_2H_5)_4$ was mixed with 2-ethoxyethanol $CH_3CH_2OCH_2CH_2OH$, then stirred for 10 minutes and subsequently slowly added drop wise to the Bi-acetic acid solution. This solution was stirred for 24 h to yield homogeneous solutions. The concentration and viscosity were adjusted with 2-ethoxyethanol. The scheme for the preparation of BSO sols with Rh 60 is shown in Fig.23.

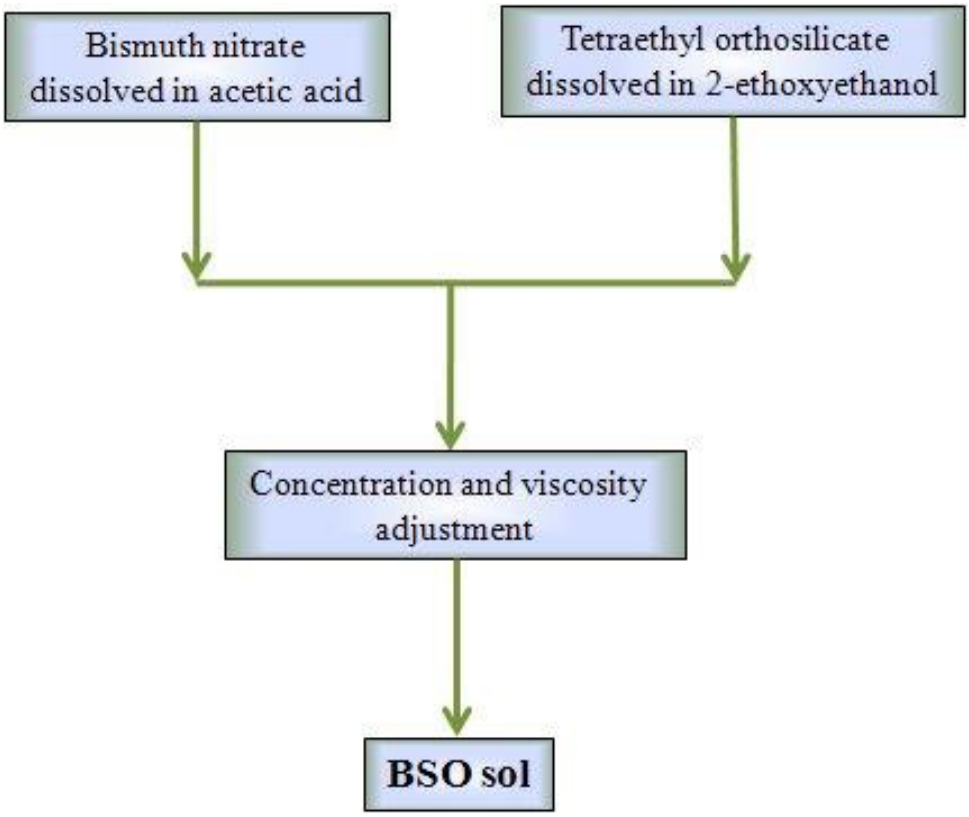

Figure 23: Scheme for synthesis of BSO sols

3.2.2 Sols with molar ratio R_h 5

Bismuth nitrate $Bi(NO_3)_3 \cdot 5H_2O$ was vacuum dried at 60°C for 96 hours. This procedure was used to remove the water from $Bi(NO_3)_3 \cdot 5H_2O$ and consequently lowering the R_h (molar ratio between water and TEOS) from 60 to 5. Dried bismuth nitrate was then dissolved in acetic acid CH_3COOH. Ethanolamine $H_2NCH_2CH_2OH$ was added drop wise under constant stirring at room temperature to prevent the uncontrolled hydrolysis of bismuth nitrate. The stoichiometric amount of tetraethylorthosilicate $Si(OC_2H_5)_4$ was mixed with 2-ethoxyethanol $CH_3CH_2OCH_2CH_2OH$, and stirred for 10 minutes. Then it was slowly added to the Bi-ethanolamine-acetic acid solution. The obtained solution was stirred for 24 h to achieve better homogenisation. The concentration and viscosity were adjusted with 2-ethoxyethanol. Fig. 24 shows the scheme for the preparation of BSO sols with Rh 5.

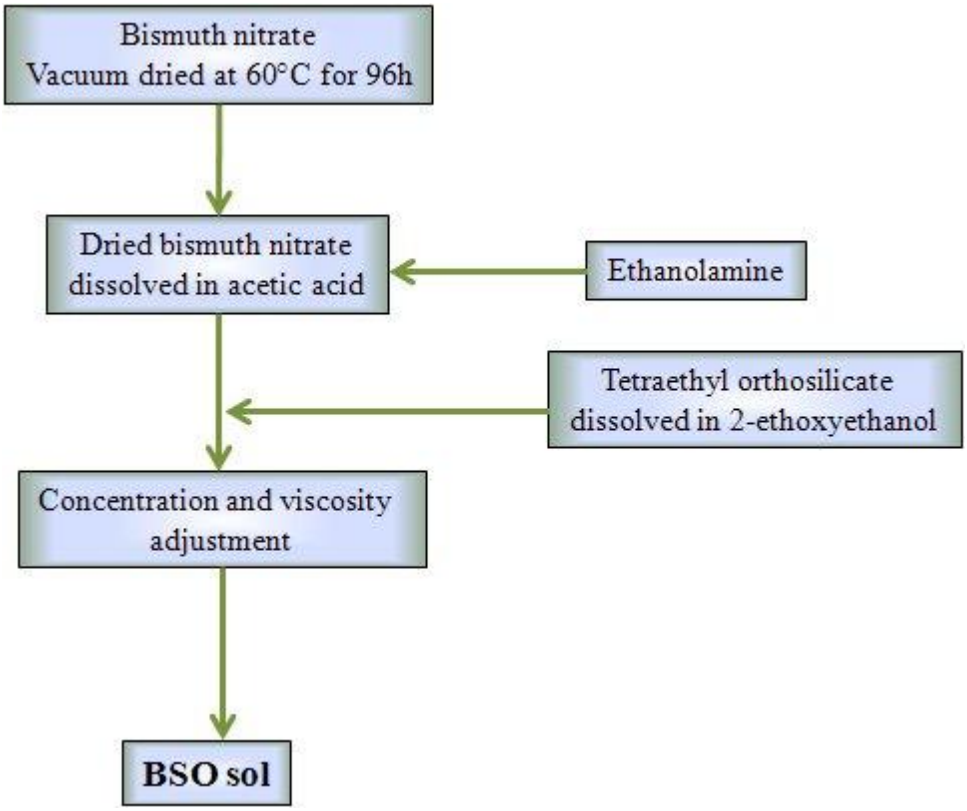

Figure 24: Scheme for synthesis of BSO sols

3.2.3 Sols with molar ratio R_h 60 using DCCA (drying control chemical additive)

Bismuth nitrate $Bi(NO_3)_3 \cdot 5H_2O$ was dissolved in acetic acid CH_3COOH at 40°C with a constant rate of stirring. The stoichiometric amount of tetraethylorthosilicate $Si(OC_2H_5)_4$ was mixed with 2-ethoxyethanol $CH_3CH_2OCH_2CH_2OH$ or acetic acid, stirred for 10 minutes and then slowly added drop wise to the Bi-acetic acid solution. A drying control additive (DCCA) formamide $HCONH_2$ was added in order to reduce the rate of hydrolysis and condensation. The obtained solution was stirred for 24 h for better homogenisation. The concentration and viscosity were adjusted with 2-ethoxyethanol. The scheme for the preparation of BSO sols with R_h60 using DCCA is shown in Fig. 25.

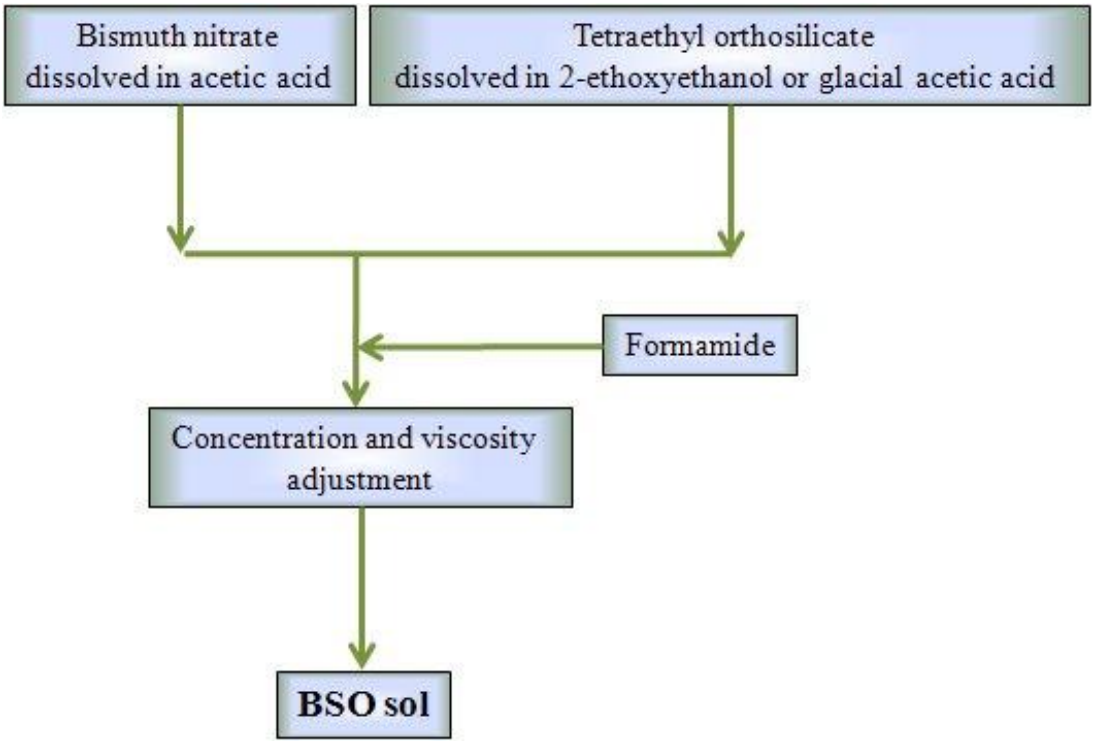

Figure 25: Scheme for synthesis of BSO sols

3.3 Thin-film deposition

Sols were deposited onto various substrates which were mounted on the sample holder of a spin coater using a vacuum and rotated at 3000–7000 rpm for 30 seconds. After each deposition the thin films were heat treated on a hot plate at 250°C for 2 minutes to evaporate the solvent and remove the residual organic. It is important to note that dust and other impurities in the working environment greatly influence the quality of the thin film. Therefore, the deposition of BSO thin films was performed in a controlled environment, i.e. a protective work-bench. A protective work-bench has a controlled level of contamination that is specified by the number of particles per cubic meter at a specified particle size. To give some perspective, the un-controlled ambient air contains 35 000 000 particles (0.5 μm and larger in diameter) per cubic meter, corresponding to ISO 9 cleanroom standards. The deposition of BSO thin films was conducted in a protective work-bench LFV 12, corresponding to ISO 4 cleanroom standards (10 000 particles/m^3, 0.1 μm and larger in diameter). In addition, dust and other impurities in the sols were removed from the sol by filtering through a 0.2-μm syringe filter during deposition. The deposition was repeated 4 times to produce the optimal density and thickness. Thin films were annealed at 700°C for 1h. From the literature it is known[112-115, 134] that the substrate may influence the microstructural development of BSO thin films, therefore BSO thin films were deposited on various substrates. Table 6 shows substrates that were used in the BSO thin films' deposition.

Table 6: Used substrates for deposition of BSO thin films in this study

Substrates	Unit cell	Cell parameter (Å)	Roughness (nm)
Sapphire	hexagonal	a= 4.75 b = 12.98	0.5
Si	cubic	5.85	0.5
Pt/TiO_2/SiO_2/Si	cubic	3.97	5
Spinel	cubic	8.08	0.5

3.4 Thin-film characterization

3.4.1 Structural characterization

3.4.1.1 Infrared spectroscopy study

Fourier transform infrared (FT-IR) spectroscopy measures polychromatic light absorption. The set of vibration of molecules or crystals are unique (providing fingerprints) to the particular material, which makes vibrational spectroscopy a valuble tool for molecule and phase identification. Besides, FT-IR spectroscopy is more sensitive to the local molecule structure compared to the X-ray diffraction method. In addition it is non destructive and it allows investigations of samples in any physical state and of any surface at any temperature and pressure.

The IR spectroscopy is the study of the interaction of infrared electromagnetic radiation with matter, specifically optical vibration of molecules or crystal. Vibrational energies lie in the energy order of 450-5000 cm^{-1} (or 0-60 kJ/mol) so they fall in the infrared region of the spectrum. A plot of measured infrared radiation intensity versus wavenumber is known as an infrared spectrum. Infrared spectra are conventionally plotted with a high wavenumber on the left and a low wavenumber on the right.

The reactions in the sols were investigated with help of an Attenuated Total Reflection Fourier Transform Infrared Spectroscopy (ATR-FT-IR) measurement. ATR attachment equipped with Ge ATR crystal (incidend angle 45°) was used. For sol and thin film investigations a Bruker IFS 66/S spectrometer (Bruker AXS Germany) was used.

3.4.1.2 X-ray diffraction study

X-ray diffraction is a non-destructive technique that reveals detailed information about the chemical composition and crystallographic structure of materials. The structure of thin films was studied using X-ray diffraction (XRD) analysis with a Cu-Kα (λ = 1.5406 Å) x-ray source and a Bruker X-ray diffractometer (ENDEAVOR D4, Bruker AXS, Germany). Ceramic thin films were measured at 2 angles from 20° to 60° with a step of 0.02 °/2 s.

The incidence angle of the emitted x-rays was constantly equivalent to the angle of x-ray detector (Bragg-Brenton configuration); therefore, the obtained x-ray reflections were the ones occurring on planes parallel to the bottom of the substrate. The drawback of this method is that because of large incidence angle of the x-rays we also obtain reflections from the substrate.

For the identification of the phase evolution of thin films we used PDF database (PCPDFWIN, version 2.2, June 2001, JCPDS-ICDD) and the computer program EVA (Bruker AXS, EVA Application, version 8.0, Release 2002).

3.4.1.3 Thermo-analytical study of thin films and xerogels

Thermal analyses (TA) consist of a group of techniques where a change in the sample properties is related to an imposed temperature alteration.

- Thermogravimetry (TG) is a technique in which the change in the sample mass is analysed while the sample is subjected to temperature alteration.
- Differential scanning calorimetry (DSC) is a technique in which the change in the heat flow rate to the sample and to a reference sample is analysed while they are subjected to a temperature alteration.
- Differential thermal analysis (DTA) is a technique in which the change in temperature of the sample and the reference sample is analysed while they are subjected to a temperature alteration.
- Evolved gas analysis (EGA) is a technique used to study the gas evolved from a heated sample that undergoes decomposition or desorption.

3.4.1.3.1 Thermo-analytical study of thin films

Thermogravimetrical analyses (TG) of thin layers on a $Pt/TiO_2/SiO_2/Si$ substrate were preformed with the instrument Mettler Toledo TGA / SDTA 851e (Mettler Toledo Corporation, Switzerland) in the temperature range from 25 to 600 °C. The rate of heating was 5 K / min. Differential dynamic calorimetry (DSC) of thin layers on different substrates was done on a Mettler Toledo DSC 822e (Mettler Toledo Corporation, Switzerland). The temperature range of the measurement was the same as termogravimetrical measurements.

3.4.1.3.2 Thermo-analytical study of xerogels

The sols were cast in petri dishes and left to gelate and dry. The thermal decomposition of the dried gel-xerogel was followed with TG, DTA and EGA. Dynamic thermo-analytical measurements were performed with a Simultaneos Thermal Analysis Instrument (STA) (Jupiter 449, Netzch, Germany) coupled with Mass Spectrometer (MS) (403C Aëoloss, Netzch, Germany) in the temperature range from room temperature to 600°C with a constant heating rate 5 K / min. The initial mass (10 mg) of the xerogel was weighed into a platinum crucible.

3.4.1.4 Atomic force microscopy studies of thin films

In order to study the surface morphology an Atomic Force Microscope (AFM) (VEECO DI3100, USA) was used. Commercially purchased microfabricated cantilevers with Si_3N_4 tips were used to image the thin films' surface in the tapping-mode configuration.

The AFM was operated in the tapping mode in order to avoid any damage to the film surface. In the tapping mode the cantilever is oscillating as it is dragged across the surface of the sample. As the tip comes across the surface features with varying heights the tip interacts with the surface, inducing a change in the amplitude of the oscillation. Such oscillations are detected by a laser spot reflecting at the back of the cantilever, which is probed by a photodiode and converted into surface-profile information.

3.4.1.5 Scanning electron microscopy studies of thin films

For the microstructural development of thin films deposited on various substrates a scanning electron microscope was used (JEOL – 5800, Japan).

Thin films deposited on a non-metallic substrate where coated with gold in order to avoid charging effects. When we used $Pt/TiO_2/SiO_2/Si$ as substrate the deposited thin films were sufficiently thin so that the charging effect did not appear.

The cross-sectional and surface analysis of the BSO thin films was preformed to obtain detailed information about the grain shape, grain size, film thickness and film density.

For our study we also used field-emission scanning electron microscopy (FE-SEM), (SUPRA 35VP, Carl Zeiss, Germany). It was operated in two modes: secondary electron imaging (SEI) mode and back scattered electron image (BSEI) mode. The SEI mode monitors secondary electrons, which are low-energy electrons emitted from very near the sample surface. This signal provides an image of the sample topography, and hence, the external morphology. The BSEI mode uses backscattered electrons, which have higher energies than secondary and are produce when electrons from the primary beam are bounced back out from the sample by elastic collisions with atoms. The number of backscattered electrons is proportional to the atomic number. This signal provides useful information about the composition of the material.

3.4.1.6 Transmission electron microscopy of thin films

The phase appearance after the deposition of the thin films was studied using transmission electron microscopy (TEM) (JEOL 2010, Japan) combined with energy-dispersive spectroscopy (EDS, JEOL, EX – 24063 JGT, Japan) analysis.

The thin films were first deposited on $Pt/TiO_2/SiO_2/Si$ substrates. Subsequently, the dried and pyrolysed thin films were scrubbed from the substrate into acetone in an ultrasound bath. The prepared dispersions were then dropped onto carbon-coated Cu-grids and analyzed with a transmission electron microscope.

3.4.2 Electrical characterization

The dielectric measurements were performed in a low-frequency region and in the microwave-frequency region. The dielectric measurements at 100 kHz - 1 MHz were performed with a parallel capacitor configuration (Fig. 26).

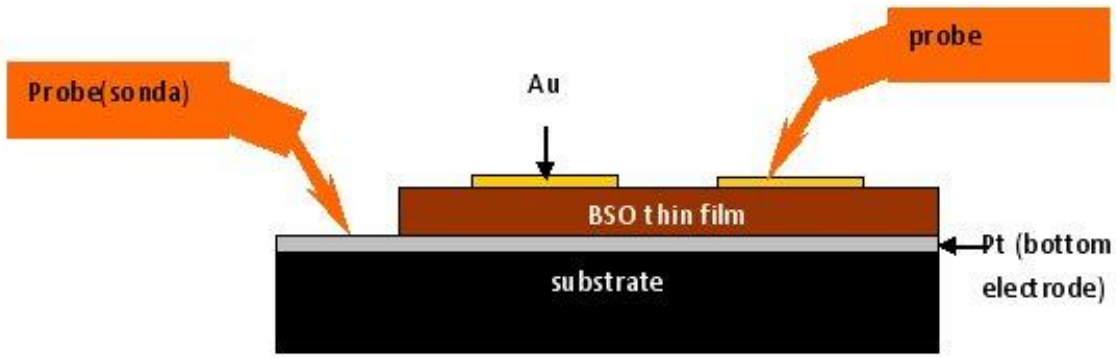

Figure 26: Configuration of the measuring system (measuring range: 40Hz-110MHz)

For the bottom electrode $Pt/TiO_2/SiO_2/Si$ was used and a Au electrode was sputtered on the top of the BSO thin film. The dielectric losses and the dielectric constant of the BSO thin films were measured with a Network analyzer Agilent 4294 (USA).

The dielectric properties of the thin films at the microwave frequency were measured with the spilt-resonator method at 10 GHz using a Network Analyzer HP-8720C (USA).The proposed geometry of the split-dielectric-resonator is shown in Fig. 27. The resonator mainly consists of two dielectric disks and a metal enclosure. The dielectric disks are thin and the height of the metal enclosure is relatively small.

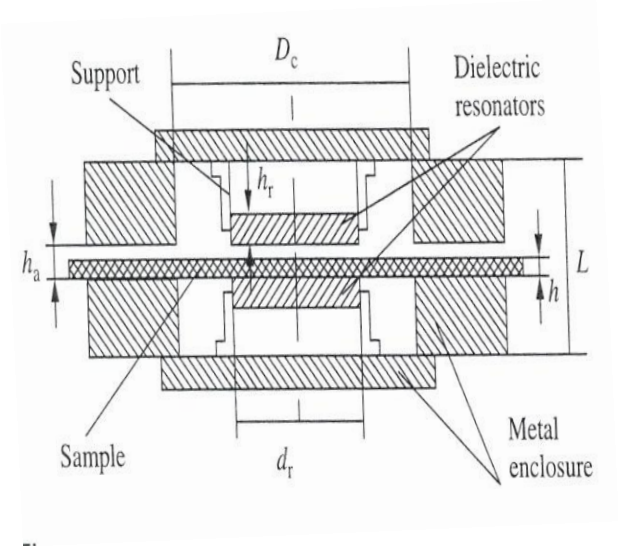

Figure 27: Scheme of split dielectric resonator system [149]

In addition, the microwave dielectric properties of the BSO thin films were also measured with the sputtered planar capacitor configuration. Fig. 28 shows the measuring system, which consists of an impedance analyzer (Aglient Tech. E4991A, USA) and a ground-source-ground (GSG) probe (DCP 100, Cascade Microtech, USA). The microwave dielectric properties were measured in the frequency range of 0.5 to 3 GHz.

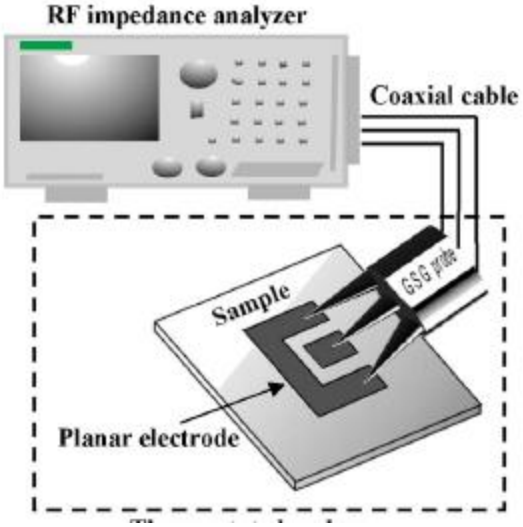

Figure 28: Configuration of the measuring system at microwave frequency [150]

A commercial, high-frequency planar analysis software (Sonnet Lite EM, Sonnet Software Inc, USA) was used to determine the permittivity of the sample by fitting the result of the electromagnetic field analysis to that of the experimentally obtained complex admittance.

4. Results and discussion

4.1 Sol-gel R_h 60

4.1.1 Sol synthesis

In this thesis the structural changes that occur during sol-gel synthesis were studied by means of FT-IR spectroscopy. The FT-IR analysis was focused on the observation of nitrate and carboxylate groups in the range from 2000 to 500 cm^{-1}. The first step in the synthesis of sol R_h 60 was dissolving $Bi(NO_3)_3 \cdot 5H_2O$ in glacial acetic acid (CH_3COOH). The ATR spectrum of $Bi(NO_3)_3 \cdot 5H_2O$ (spectrum (a) in Fig. 29) shows characteristic vibrational bands at 820, 1380 and 1620 cm^{-1}, which have been attributed to the modes of bending, stretching and harmonics of the N-O bond [136]. In addition, absorption band at 1760 cm^{-1} is attributed to the bending mode of the H-O-H bond [136]. In the ATR spectrum of the acetic acid (spectrum (b) in Fig. 29) the following characteristic bands of the carboxylate ligands were observed, carbonyl (C=O) at 1756 cm^{-1} and 1709 cm^{-1}, and the bands (C-O + O-H) at 1410 cm^{-1} and 1291 cm^{-1} [87]. The ATR FT-IR spectrum (c) in Fig. 29 corresponds to $Bi(CH_3COO)_3$. The $Bi(NO_3)_3 \cdot 5H_2O$-CH_3COOH ATR spectrum of the solution obtained after dissolving $Bi(NO_3)_3 \cdot 5H_2O$ in acetic acid is shown in spectrum (d) in Fig. 29. One can observe that the bands in the reference spectra of $Bi(NO_3)_3 \cdot 5H_2O$, acetic acid and $Bi(CH_3COO)_3$ (spectrum (a, b, c) in Fig. 29) are still present in the spectrum of the $Bi(NO_3)_3 \cdot 5H_2O$-CH_3COOH solution (spectrum (d) in Fig. 29), together with a new band at 1500 cm^{-1}, which can be attributed to carboxylate ligands [87].

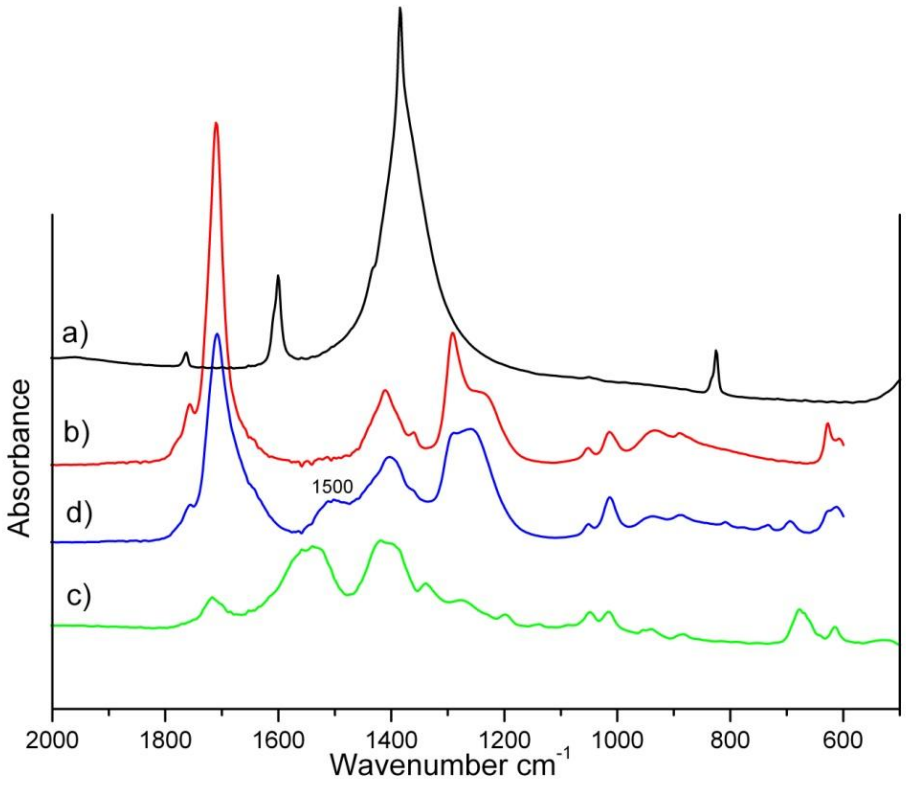

Figure 29: ATR FT-IR spectra of a) $Bi(NO_3)_3 \cdot 5H_2O$, b) CH_3COOH, c) $Bi(CH_3COO)_3$ and d) $Bi(NO_3)_3 \cdot 5H_2O$-CH_3COOH

The carboxylate ligands can coordinate in one or more modes [87], as shown in Table 7.

Table 7: Coordination modes of carboxylate ligands

Coordination mode:			Δν (cm^{-1})
Monodentate:	M–O–C(=O)–CH_3	I	425
Bidentate	M(O)(O)C–CH_3	chelating II	80
Bidentate	M–O, M←O, C–CH_3	bridging III	160

The coordination mode of carboxylate ligands can be determined with the difference between the frequencies (Δν) of the asymmetric $\nu_{asym}(COO)$ and symmetric $\nu_{sym}(COO)$ stretching vibration in the frequency range from 1750 to 1300 cm^{-1}. In the ATR FT-IR spectrum of the $Bi(NO_3)_3 \cdot 5H_2O$-CH_3COOH solution (spectrum (d) in Fig. 29) the frequency separation (Δν=80) between $\nu_{asym}(COO)$ at 1500 cm^{-1} and $\nu_{sym}(COO)$ at 1420 cm^{-1}, suggested that carboxylate ligands are bidentately coordinated to the bismuth ion (Eq. 14,15).

$$Bi(NO_3)_3 \cdot 5H_2O \rightarrow Bi^{3+} + 3(NO_3)^{-1} + 5H_2O \quad (14)$$

$$Bi^{3+} + CH_3COOH \rightarrow \quad Bi\langle O \rangle C - CH_3 \quad (15)$$

To decrease the time of gelation and the concentration of sol R_h 60 the 2-ethoxyethanol ($C_4H_{10}O_2$) was added to the solution of $Bi(NO_3)_3 \cdot 5H_2O$-CH_3COOH. The structural changes

that appear after adding 2-ethoxyethanol to the $Bi(NO_3)_3 \cdot 5H_2O$-CH_3COOH solution were determined by means of ATR FT-IR spectroscopy. Initially, the possibility of the reaction between 2-ethoxyethanol and acetic acid was investigated. In the 2-ethoxyethanol ATR FT-IR spectrum (spectrum (a) in Fig. 30), there are characteristic bands of the CH stretch, the CO stretch and the various bending vibrations. Fig. 30 spectrum (b) shows the ATR FT-IR spectrum of the already mention acetic acid. The spectrum of the solution of 2-ethoxyethanol-acetic acid (spectrum (c) in Fig. 30) shows typical bands of acetic acid and 2-ethoxyethanol, together with new bands at 1373 and 1272 cm^{-1}, belonging to the stretching vibration of ester (C-O-C) [138]. With the appearance of these two bands (1373 and 1272 cm^{-1}) the reaction between the acetic acid and the 2-ethoxyethanol (Eq. 16) was confirmed.

$$CH_3COOH + C_4H_{10}O_2 \rightarrow CH_3\text{-}CO\text{-}O\text{-}CH_2\text{-}CH_2\text{-}O\text{-}CH_2\text{-}CH_3 + H_2O \qquad (16)$$

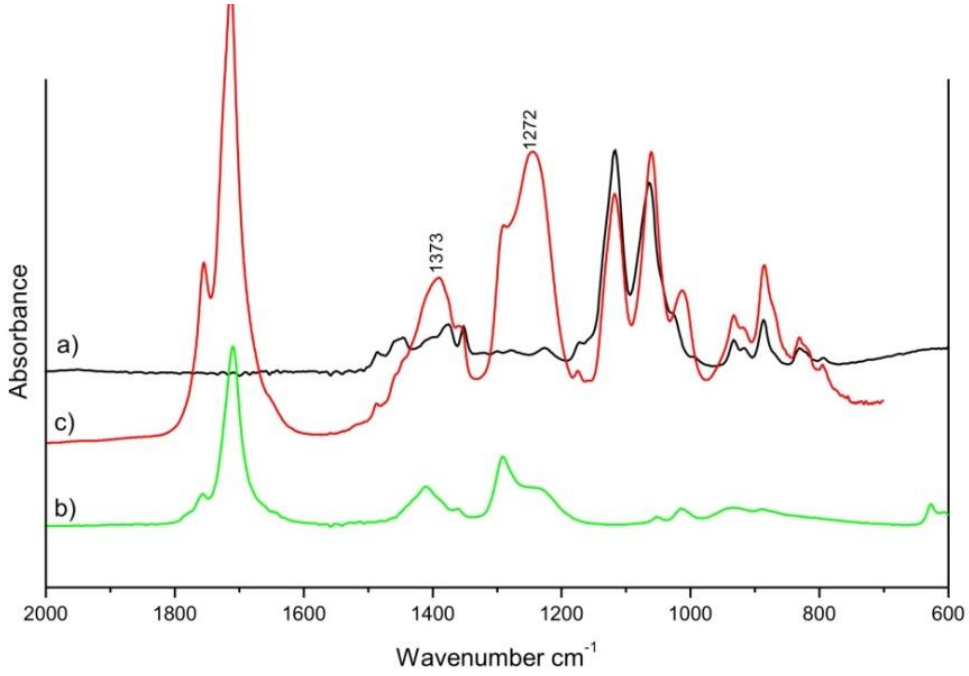

Figure 30: ATR FT-IR spectra of a) $C_4H_{10}O_2$, b) CH_3COOH and c) CH_3COOH-$C_4H_{10}O_2$

Fig. 31 shows an ATR FT-IR spectrum of the $Bi(NO_3)_3 \cdot 5H_2O$-CH_3COOH-$C_4H_{10}O_2$ solution. One can observe that after adding 2-ethoxyethanol to the $Bi(NO_3)_3 \cdot 5H_2O$-CH_3COOH solution the ester bands at 1373 and 1272 cm^{-1} are still present in the spectrum, indicating that the 2-ethoxyethanol reacted with the acetic acid.

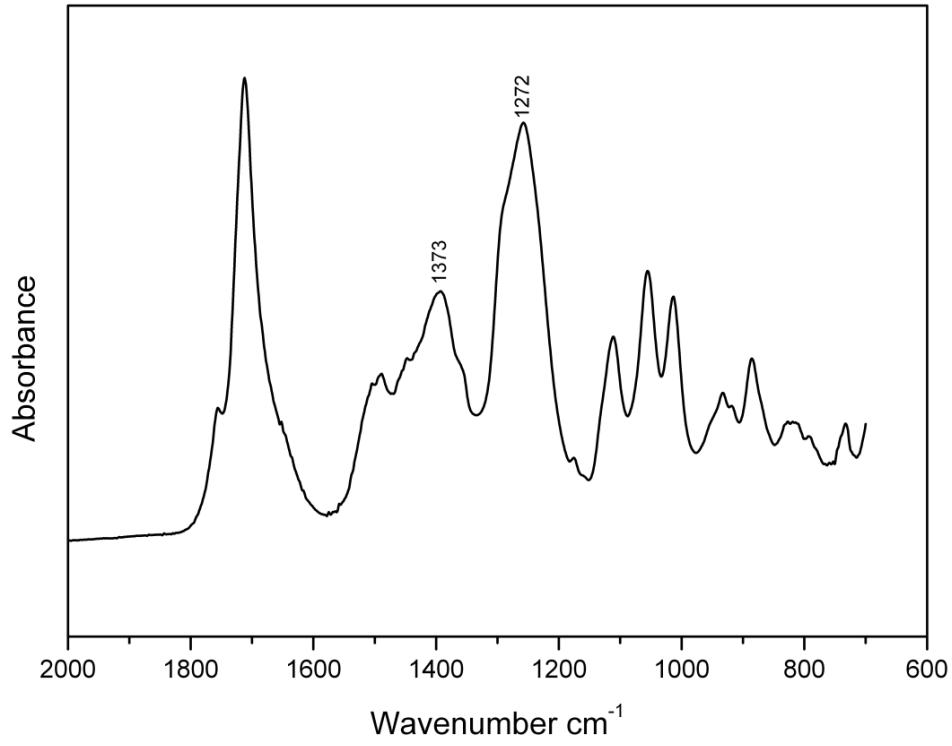

Figure 31: The ATR FT-IR spectrum of the $Bi(NO_3)_3 \cdot 5H_2O$-CH_3COOH-$C_4H_{10}O_2$ solution

The final step in the synthesis of sol R_h 60 was the addition of TEOS to the $Bi(NO_3)_3 \cdot 5H_2O$-CH_3COOH-$C_4H_{10}O_2$ solution. To understand the reactions occurring in the sol after the addition of TEOS, the possible reaction between the 2-ethoxyethanol and TEOS was studied. Fig. 32 shows the ATR FT-IR spectra of a) TEOS, b) 2-ethoxyethanol and c) TEOS-2-ethoxyethanol solution. From Fig. 32 it can be seen that all three spectra simply overlap, which indicates that there is no interaction between the TEOS and the 2-ethoxyethanol.

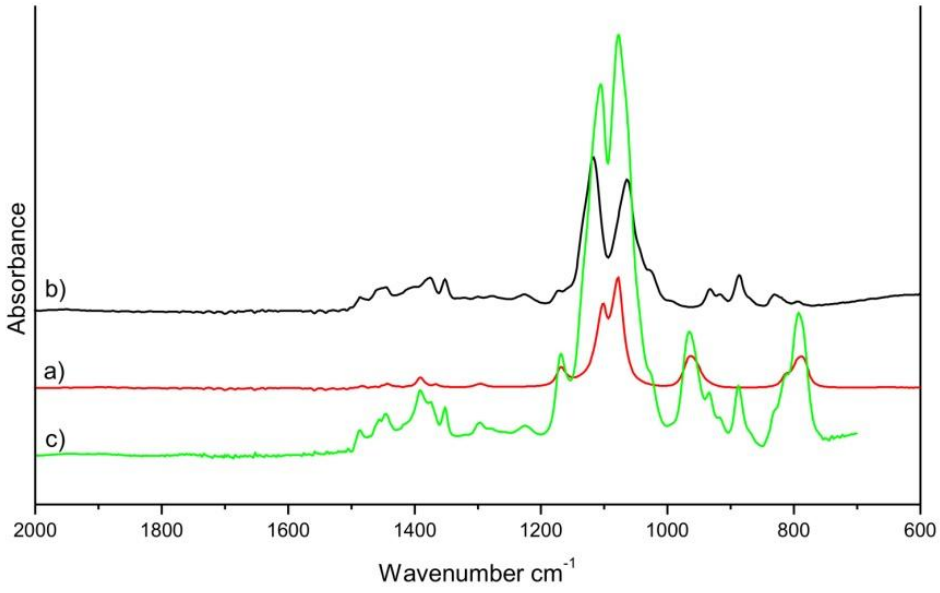

Figure 32: ATR FT-IR spectra of a) TEOS (non-hydrolyzed), b) $C_4H_{10}O_2$, c) TEOS- $C_4H_{10}O_2$ solution

For the CH_3COOH-TEOS solution (spectrum (c) in Fig. 33) similar results were observed. The ATR spectra of acetic acid (a), TEOS (b) and acetic acid-TEOS solution (c) (Fig. 33) overlap, and no additional bands are observed, which indicates that there is no reaction between TEOS and acetic acid at room temperature.

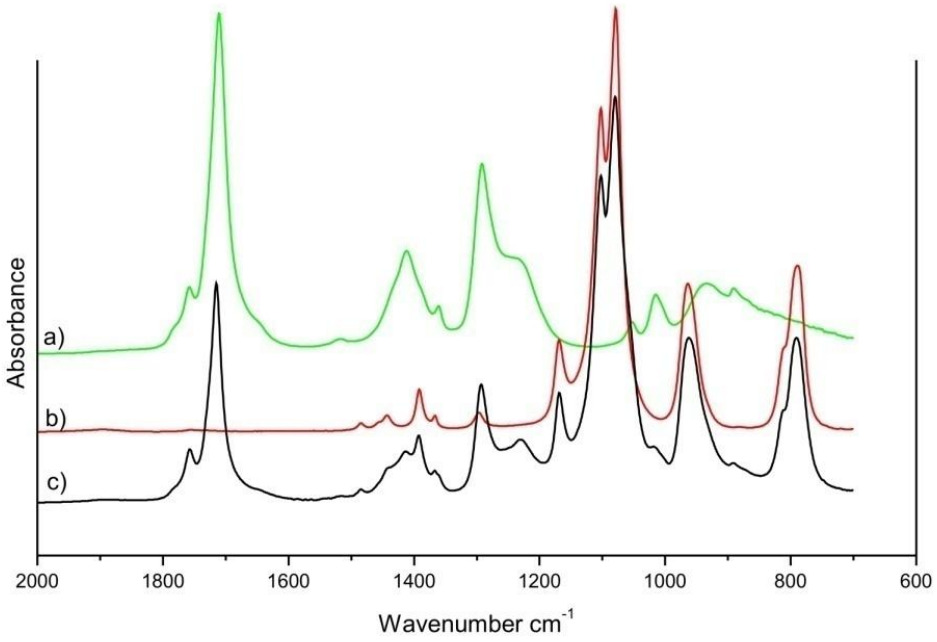

Figure 33: ATR FT-IR spectra of a) CH_3COOH, b) TEOS and c) CH3COOH-TEOS solution

In the ATR FT-IR spectrum of sol R_h 60 (spectrum (e) in Fig. 34) the bands mainly overlap with the spectra of a) TEOS-$C_4H_{10}O_2$, b) TEOS-CH_3COOH, c) CH_3COOH- $C_4H_{10}O_2$, d) $Bi(NO_3)_3{\cdot}5H_2O$- CH_3COOH, that were already previously described. However, some significant differences were observed in the ATR spectrum of sol R_h60 (spectrum (e) in Fig. 34) which was not present in the previously observed and described spectrums. Namely, after adding the TEOS and 2-ethoxyethanol to the $Bi(NO_3)_3{\cdot}5H_2O$-CH_3COOH solution the bismuth coordination sphere changes. The carboxylate ligands are no longer bidentately coordinated to bismuth. This was confirmed with the disappearance of the peak at 1500 cm^{-1} (spectrum (e) in Fig. 34). A similar observation was reported by Yi and Sayer [139] as they studied the modification of Zr and Ti alkoxide with acetic acid, where a carboxylate group was removed from the alkoxide coordination sphere by the esterification.

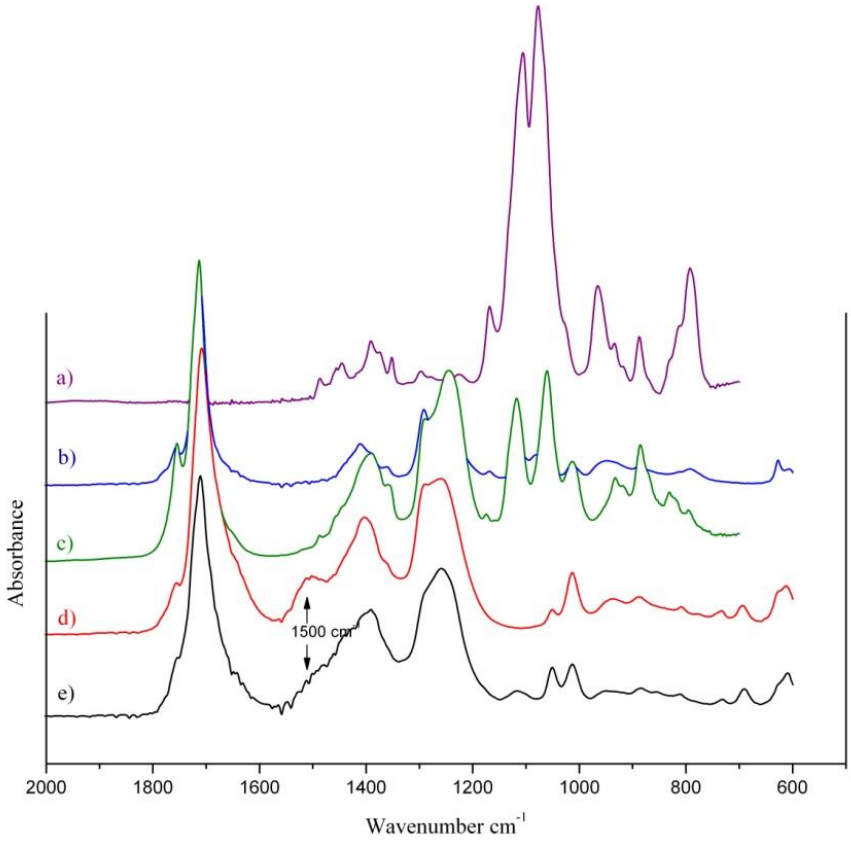

Figure 34: FT-IR spectra of a) TEOS-$C_4H_{10}O_2$, b) TEOS-CH_3COOH, c) CH_3COOH- $C_4H_{10}O_2$, d) $Bi(NO_3)_3{\cdot}5H_2O$- CH_3COOH and e) sol R_h60

To obtain homogeneity in sols with R_h 60, the precursors must be equally distributed in the sol. This distribution in the sol may lead to the reaction between precursors, TEOS and $Bi(NO_3)_3{\cdot}5H_2O$, forming a bismuth silanolate $[Bi(OSiEt_3)_3]$. The formation of the $[Bi(OSiEt_3)_3]$ was determined with FT-IR spectroscopy by M. Mehring et al. [140]. In the FT-IR spectrum of $[Bi(OSiEt_3)_3]$ they determined absorbance bands at 1414, 1237, 1015, 974, 954, 878, 846, 828 and 736 cm^{-1}, respectively [140]. However, the formation of $[Bi(OSiEt_3)_3]$ (Fig. 35) in sol R_h 60 cannot be determined using FT-IR spectroscopy, due to the small amount of silicon atoms, the large amount of solvents and the overlapping bands.

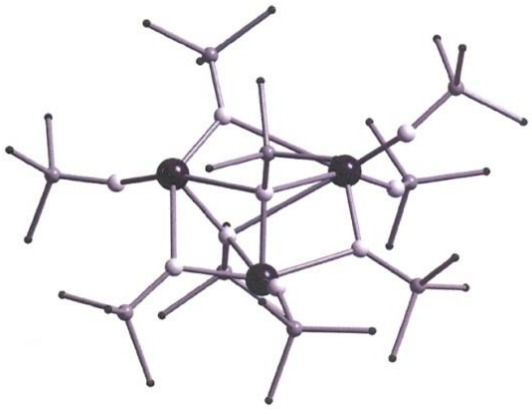

Figure 35: Molecular structure of trimeric $[Bi(OSiEt_3)_3]$. The large black spheres correspond to Bi atoms and the smaller ones to C atoms, while O and Si atoms are represented by different shades from brighter to darker, respectively [140]

It has been reported [140] that the hydrolysis of bismuth silanolates proceeds by the formation of small aggregates of bismuth-oxo(hydroxy) siloxides, which are further linked by hydrolysis-condensation reactions to give compounds of the general type $[BiO_x(OH)_y(OSiEt)_{z-y-2x}]_n$ [140], as presented in Eq. 17.

$$n[Bi(OSiEt_3)_3] + (\ell + m)H_2O \rightarrow [Bi_nO_\ell\,(OH)_m(OSiEt_3)_{3n-(2\ell+m)}] + (2\,\ell + m)R_3SiOH \quad (17)$$

Thermal decomposition of the hydrolysis products $[Bi_nO_\ell\,(OH)_m(OSiEt_3)_{3n-(2\ell+m)}]$ gave α-Bi_2O_3, β-Bi_2O_3, $Bi_{12}SiO_{20}$ or $Bi_4Si_3O_{12}$, depending on the triorganosilanolate ligand, the amount of water and the temperature. At this point we assumed that the interaction of the bismuth and silicon ions in the sols with R_h 60 occurred by forming bismuth silanolates, which was later confirmed with TEM analysis of the dried thin films (pp. 13-14).

In sol-gel derived thin films the stability and viscosity of the sols have a significant influence on further microstructural development. Therefore, it is essential to determine the influence of the sol's concentration on the stability and viscosity of the sol and the time of gelation (Fig. 36 and Fig. 37). Fig. 36 shows that the viscosity of the just formed sol strongly depends on the amount of 2-ethoxyethanol in the sol. Diluting the sols with R_h 60 to the concentration of 0.76 M causes a rapid decrease in the sol viscosity. With a further dilution below the concentration of 0.76 M, we observed the formation of unstable sols. A rapid decrease in the viscosity of the sols that appears due to dilution with 2-ethoxyethanol, resulted from the retardation of the condensation reaction rate of the hydrolysed silanol products.

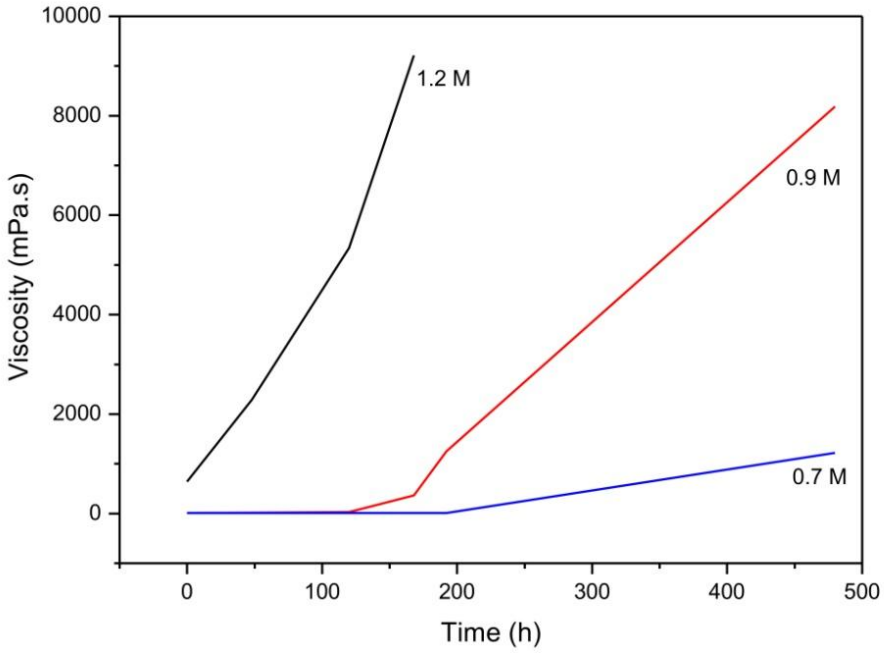

Figure 36: Dependence of the sol concentration on the viscosity of sol R_h 60

The time of gelation also depends on the amount of 2-ethoxyethanol in the sol (Fig. 37). When the sols were diluted with 2-ethoxyethanol to the 0.76 M sol concentration the time of gelation increased. Sols with a concentration of 1.2 M gelated in 5 h, while sols with a concentration 0.76 M gelated in 470 h.

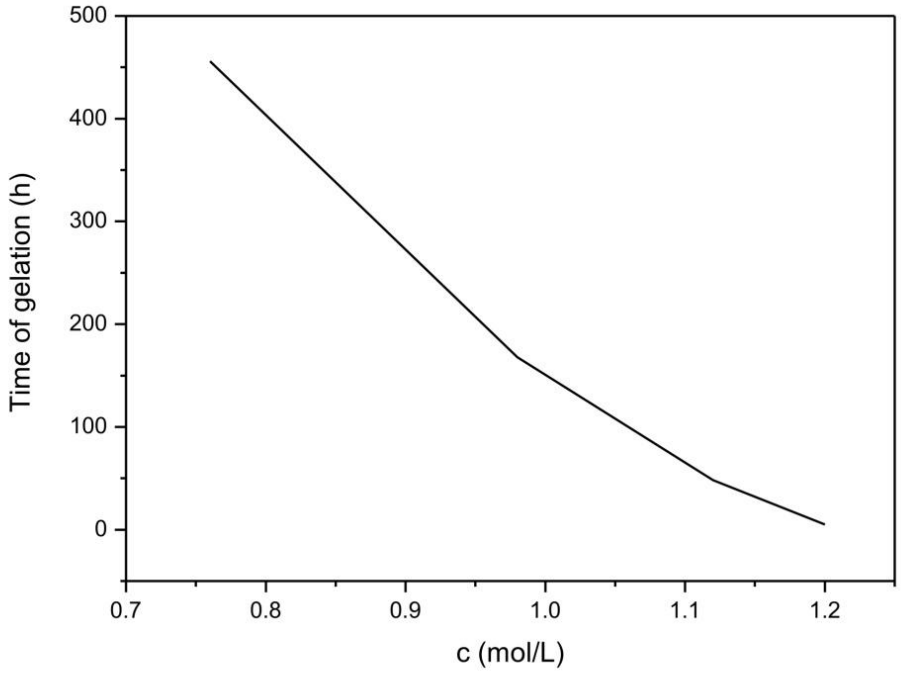

Figure 37: Dependence of the sol concentration on the time of gelation of sol R_h 60

With further dilution of the sol with 2-ethoxyethanol, below a concentration of 0.76 M, the formation of precipitates was observed. Fig. 38 spectrum (a) shows the FT-IR transmission spectrum of the isolated precipitate with the following bands at 1670, 1620, 1380 and 820 cm^{-1}. The FT-IR transmission spectrum of pure $Bi(NO_3)_3 \cdot 5H_2O$ is shown in Fig. 38 spectrum (b). By comparing the spectrum (a) and spectrum (b) from Fig. 38 it can be clearly seen that the spectrums of $Bi(NO_3)_3 \cdot 5H_2O$ and the precipitate simply overlap. This observation suggested that $Bi(NO_3)_3 \cdot 5H_2O$ precipitates from the sol below a 0.76 M concentration.

It has already been reported that bismuth nitrate easily hydrolyzes in acid/water conditions, resulting in the formation of precipitates [63, 64]. The reaction between acetic acid and 2-ethoxyethanol in the sol leads to the in-situ formation of water, which enables reaction with bismuth ion and causing the formation of precipitates. Therefore, in the higher sol concentration $c \geq 0.76$ M the amount of water formed as by product of esterification is still small enough so that precipitation does not occur. In contrast for sols with concentration $c \leq 0.76$ M the esterification produces a critical amount of water, which allows $Bi(NO_3)_3 \cdot 5H_2O$ to precipitate.

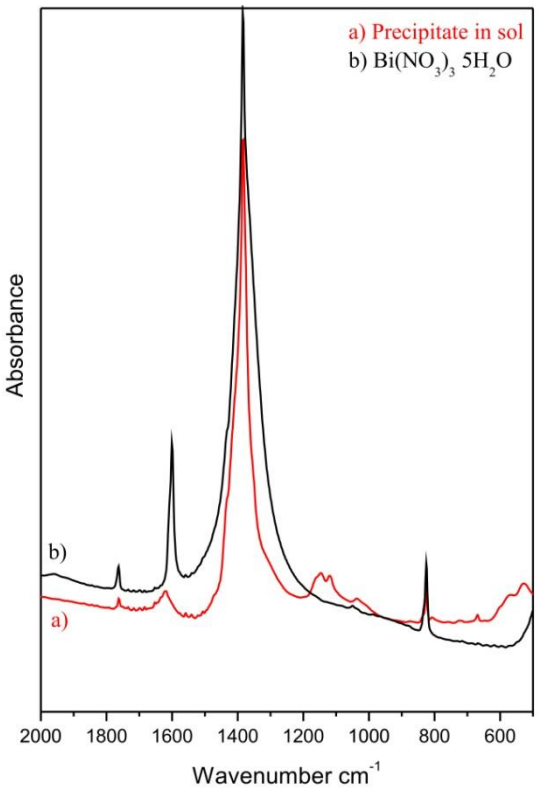

Figure 38: FT-IR transmission spectra of a) precipitate in sol R_h 60 and b) $Bi(NO_3)_3 \cdot 5H_2O$

4.1.2 Thin-film deposition

After synthesis of the sol R_h 60 the deposition of a thin film with spin-coating method was carried out. The FT-IR transmission analysis was also used for thin film investigation to determine the structural changes after the deposition. The FT-IR transmission spectrum of the dried thin film deposited on the silicon substrate is shown in Fig. 39. The observed band at 1754 cm^{-1} is related to the stretching vibration of acetic acid which still remains in the amorphous thin film [87]. The band at 1632 cm^{-1} is related to stretching vibration of water [141]. The absorption bands located at 1383, 1291,808 and 732 cm^{-1} are assigned to the stretching vibrations, out of plane and in-plane bend vibration of N-O ligands that are coordinated to bismuth ions[141]. The band at 1041 cm^{-1} is related to the asymmetric stretch of Si-O-Si bond [141]. Bands located at 700 cm^{-1} and 569 cm^{-1} are assigned to the stretching vibration of the Bi-O bond [142].

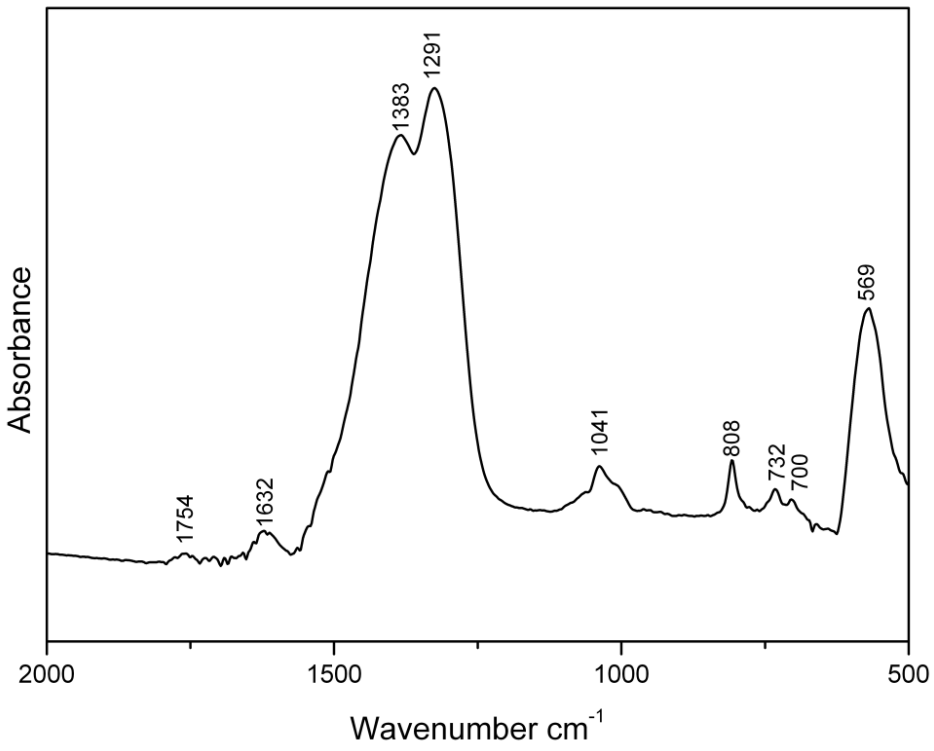

Figure 39: FT-IR transmission spectrum of thin film deposited from sol R_h 60

As already mentioned, due to small amount of silicon atoms, large amount of solvent and the overlapping bands, the presence of $[Bi(OSiEt_3)_3]$ could not determined by the FT-IR analysis. Therefore, the presence of $[Bi(OSiEt_3)_3]$ in dried thin films was investigated by TEM analysis.

Fig. 40 a) shows a typical TEM morphology of dried thin film, which consists of the amorphous phase. In addition some bigger crystalline particles were observed in the dried thin film, as shown in Fig. 40 b). The area of darker contrast for the particles corresponds to thicker particles.

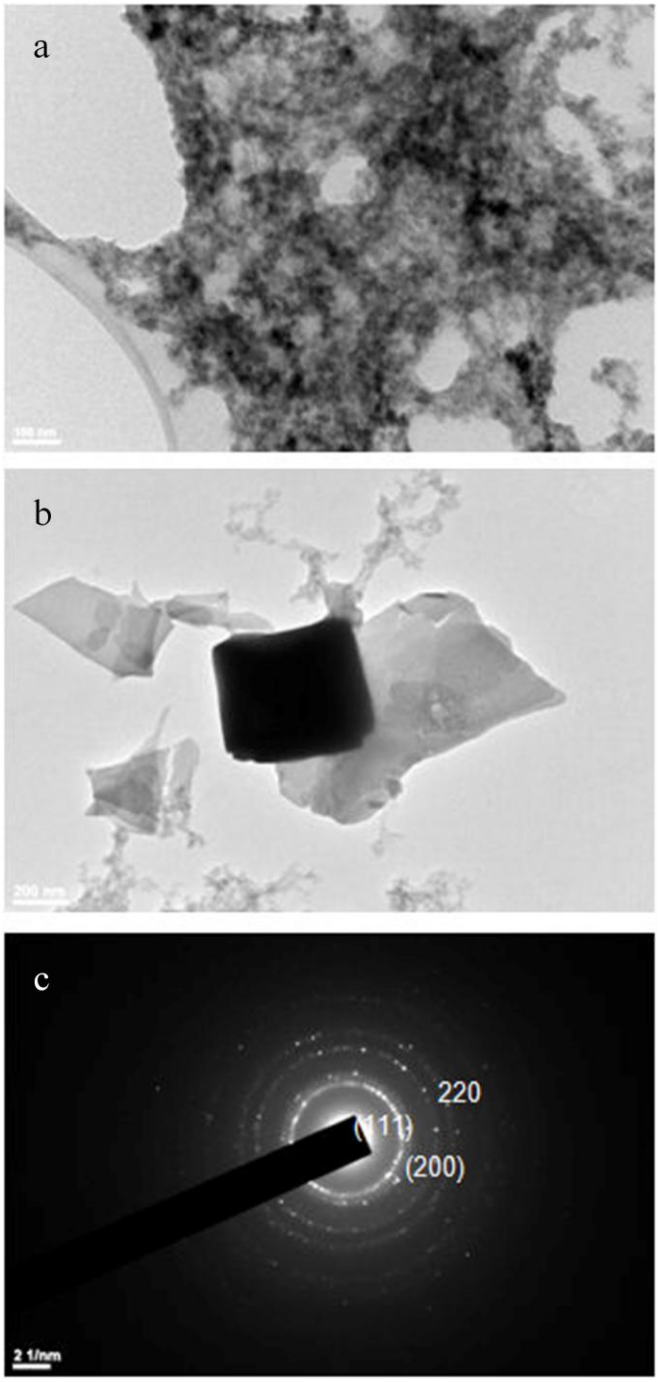

Figure 40: TEM analysis of a) and b) dried thin film deposited from sol R_h 60 and c) electron diffraction pattern of the crystalline particle (Fig. 31 b)

The electron diffraction pattern of the particles (Fig. 40 c) shows that the crystalline phase corresponds to the δ-Bi_2O_3. The δ-Bi_2O_3 is not stable at room temperature, therefore, we assumed that it was stabilised with silicon atoms. This assumption was confirmed with energy-dispersive spectroscopy (TEM-EDS) analysis of a crystalline particle (Fig. 41).

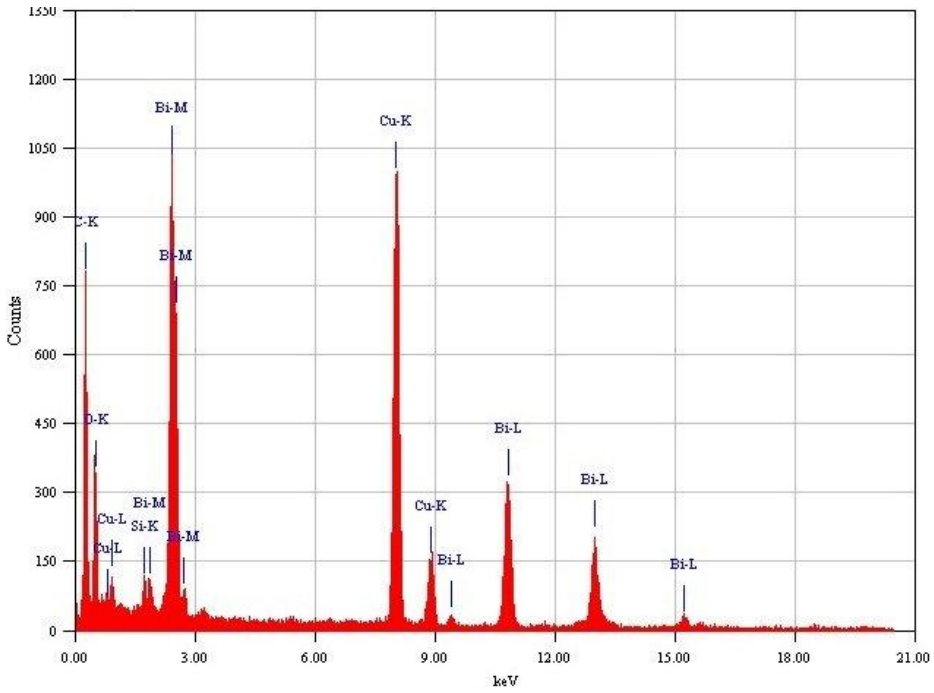

Figure 41: The EDS spectrum of crystalline particle shown in Fig. 40 b.

In the EDS spectrum (Fig. 41) the bismuth and silicon peaks were detected. In addition, copper peaks were observed which come from the Cu-grid. This result, together with electron diffraction pattern, confirmed that δ-Bi_2O_3 is stabilized with silicon atom. The formation of δ-Bi_2O_3 indicates a reaction between the TEOS and $Bi(NO_3)_3{\cdot}5H_2O$.

In addition, when dried thin film deposited from sol R_h 60 was aged for 24 h, the formation of $[Bi(OSiEt_3)_3]$ resulting from the reaction between the TEOS and $Bi(NO_3)_3{\cdot}5H_2O$, was confirmed by the TEM analysis. Fig. 42 a) and b) shows a typical TEM morphology of the dried thin film aged for 24 h, which consisted of 10 nm size particles. The corresponding electron diffraction pattern (Fig. 42 c) shows that the crystalline particles belong to the eulytite phase. The TEM results and the reported data of the decomposition behaviour of $[Bi(OSiEt_3)_3]$ [140] confirm the formation of $[Bi(OSiEt_3)_3]$ in sol R_h 60.

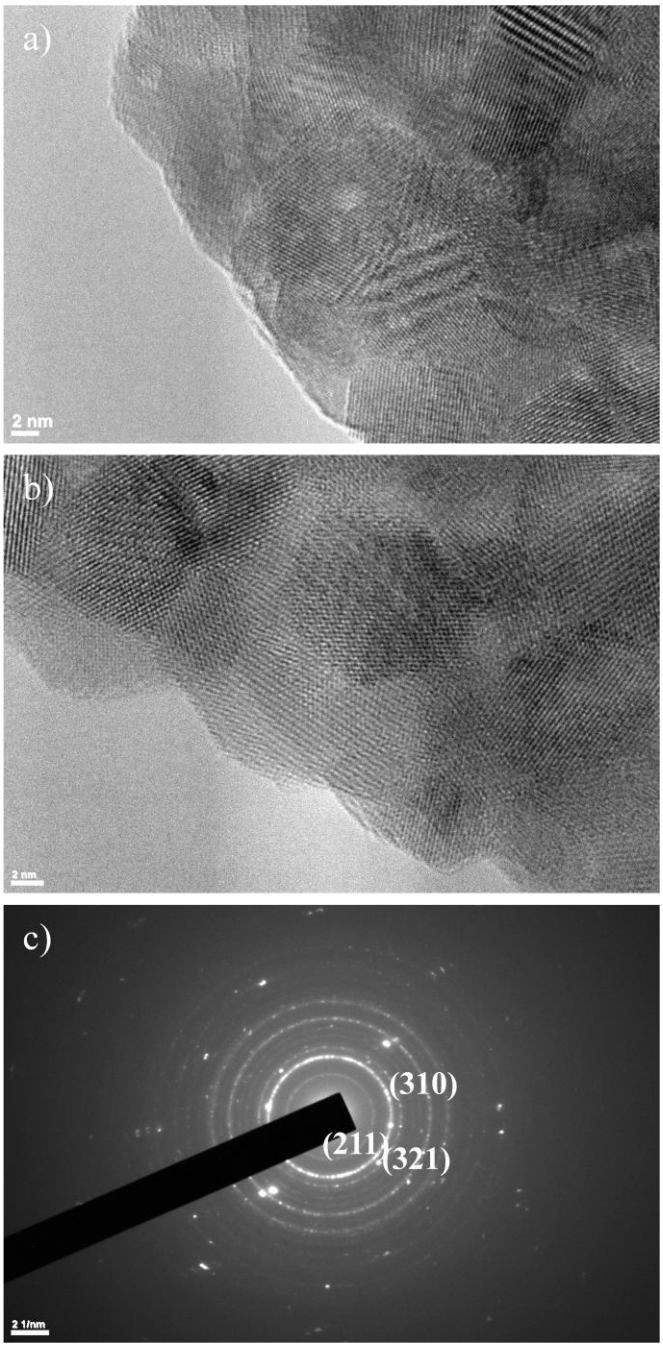

Figure 42: TEM analysis of a) and b) dried thin film deposited from sol R_h 60 aged for 24h and c) electron diffraction pattern of the crystalline particle (Fig. 42 b)

The crystallization of $Bi_{12}SiO_{20}$ (BSO) could occur via two routes: 1) direct crystallization of BSO phase from the amorphous form or 2) formation of individual elements or oxide of one or more elements and their subsequent reaction to form the BSO phase. In order to study the formation of the BSO phase the X-ray diffraction analysis was used. The thin film deposited on a sapphire substrate was annealed at temperatures ranging from 300°C to 700°C.

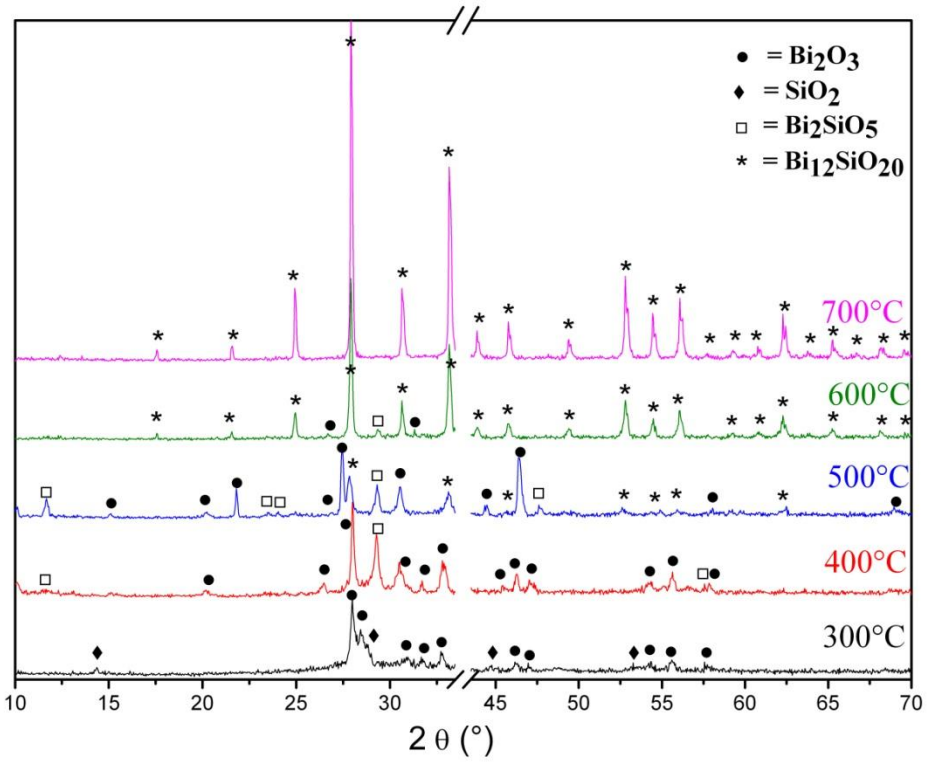

Figure 43: X-ray diffraction patterns of thin films deposited on a sapphire substrate and heated at various temperatures

The results of the XRD analyses are shown in Fig. 43. After the deposition of the sol R_h 60 with a concentration of 0.76 M on a sapphire substrate the solvent started to evaporate and the gel forms. During the drying and heating the organic part decomposes and the amorphous layer crystallize. At 300°C we observed the presence of bismuth oxide and silicon oxide phases. An increased annealing temperature up to 400°C leads to the disappearance of silicon oxide x-ray reflection peaks and the formation of the bismuth silicate phase (Bi_2SiO_5). After heating at 500°C the formation of a new phase, $Bi_{12}SiO_{20}$ (BSO), was confirmed. At 600°C the majority of the x-ray reflections are assigned to the BSO phase. However, there are still traces of the bismuth oxide and bismuth silicate phases present. When the annealing temperature was increased to 700°C the only detected phase was BSO.
In the sol-gel derived thin films the formation of BSO goes through the following reactions (Eq. 18-19):

$$Bi_2O_3 + SiO_2 \rightarrow Bi_2SiO_5 \text{ starting at T} \sim 400°C \quad (18)$$

$$Bi_2SiO_5 + 5Bi_2O_3 \rightarrow Bi_{12}SiO_{20} \text{ starting at T} \sim 500°C \quad (19)$$

In the solid state synthesis the formation of BSO goes trough following reactions (Eq. 20-24) [143]:

$$6Bi_2O_3 + SiO_2 \rightarrow Bi_{12}SiO_{20} \text{ starting at T} \sim 600°C \quad (20)$$

$$Bi_2O_3 + SiO_2 \rightarrow Bi_2SiO_5 \text{ starting at T} \sim 650°C \quad (21)$$

$$2Bi_2O_3 + 3SiO_2 \rightarrow Bi_4Si_3O_{12} \text{ starting at T} \sim 750°C \quad (22)$$

$$Bi_2SiO_5 + 5Bi_2O_3 \rightarrow Bi_{12}SiO_{20} \text{ starting at T} > 800°C \quad (23)$$

$$Bi_4Si_3O_{12} + 16Bi_2O_3 \rightarrow 3Bi_{12}SiO_{20} \text{ starting at T} > 800°C \quad (24)$$

By comparing the formation reactions of BSO by the sol-gel process to solid-state synthesis it can be seen that in the sol-gel process the BSO phase forms at a much lower processing temperature than during solid state synthesis. The crystallization of sol-gel derived BSO thin films goes through path 2, which is through the formation of an individual oxide and their subsequent reaction to form the BSO phase.
Under annealing conditions at 700°C/1h, no significant evaporation or sublimation of Bi_2O_3 from the thin films was observed, as only the single BSO phase formed and no secondary Bi-deficient phases were detected. The same phase evolution was observed for the spinel and $Pt/TiO_2/SiO_2/Si$ substrates.
In contrast, thin films deposited on a silicon substrate annealed at 700°C/1h resulted in the formation of the eulytite ($Bi_4Si_3O_{12}$) phase instead of the $Bi_{12}SiO_{20}$ phase (Fig. 44).

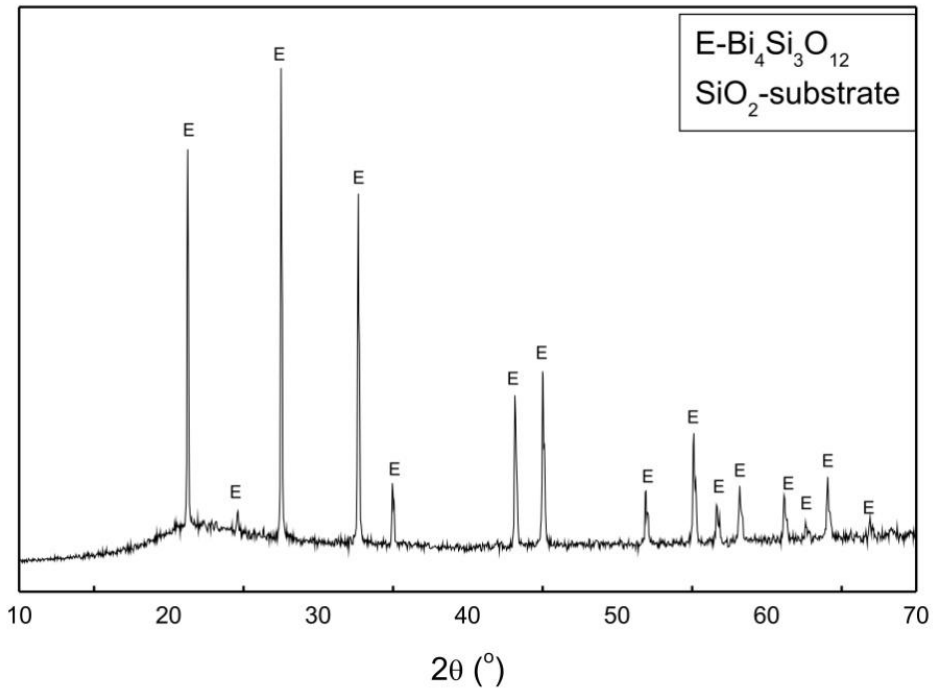

Figure 44: X-ray diffraction patterns of thin films deposited on a silicon substrate annealed at 700°C, 1h

The formation of the eulytite phase in thin films deposited on a silicon substrate can be understood by examining the binary diagram of the Bi_2O_3-SiO_2 system in which three compounds with Bi_2O_3 : SiO_2 molar ratio = 6 : 1 ($Bi_{12}SiO_{20}$), 2 : 3 ($Bi_4Si_3O_{20}$) and 1 : 1 (Bi_2SiO_5) have been reported to exist (Fig. 45) [144]. From the binary diagram of Bi_2O_3-SiO_2 (Fig. 45), it can be seen that the eulytite phase forms in a silicon-oxide-rich part of the diagram.

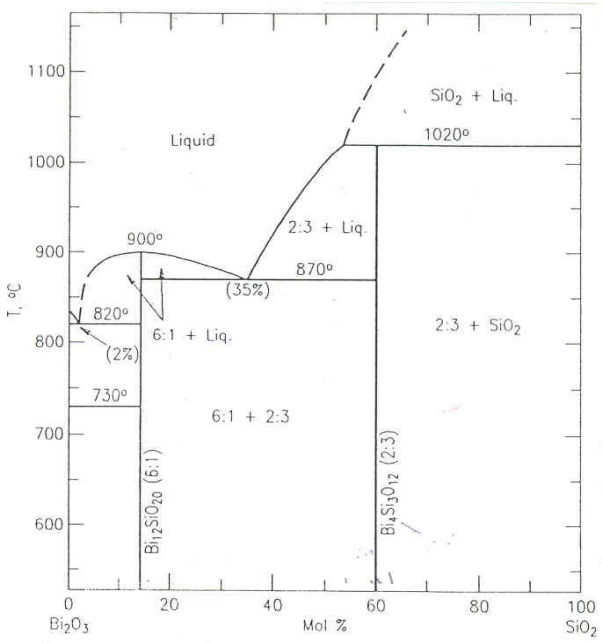

Figure 45: Binary phase diagram of Bi_2O_3-SiO_2 system [144]

We believe that the formation of the eulytite phase can be attributed to the reaction between the substrate and the thin film. This reaction can be determined by the deposition of a sol on an inert substrate, such as metal gold (Au). The deposited thin films on the Au substrate were annealed at 700°C/1h. The XRD results of annealed thin film on the Au substrate showed the formation of a single BSO phase (Fig. 46). This observation confirmed that in case of using a silicon substrate for the deposition the thin film reacts with the substrate during annealing.

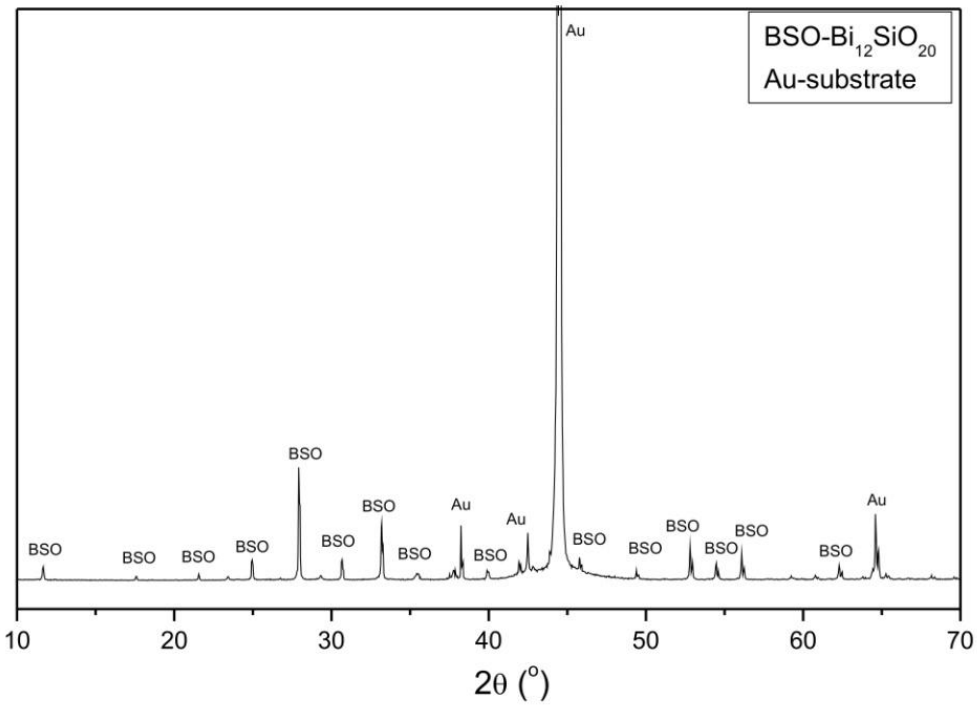

Figure 46: X-ray diffraction patterns of BSO thin films deposited on the Au substrate annealed at 700°C/1h

The influence of different substrates ($Pt/TiO_2/SiO_2/Si$, sapphire, spinel) on the microstructural development of the BSO thin film annealed at 700°C, deposited from a sol with a concentration of 0.76 M, were studied with FE-SEM (Fig. 47). BSO thin films ($Pt/TiO_2/SiO_2/Si$, sapphire, spinel) show a high porosity. We believe that the obtained porous microstructure after annealing is due to the high polymerization rate, which causes entrapment of a large amount of solvent in the film during gelation.

In addition, no significant variation in the microstructural development of the BSO thin films on the various substrates was observed (Fig. 47), which implies that the influence of the substrate on the microstructure is reduced during the pre-heating and annealing of thin films.

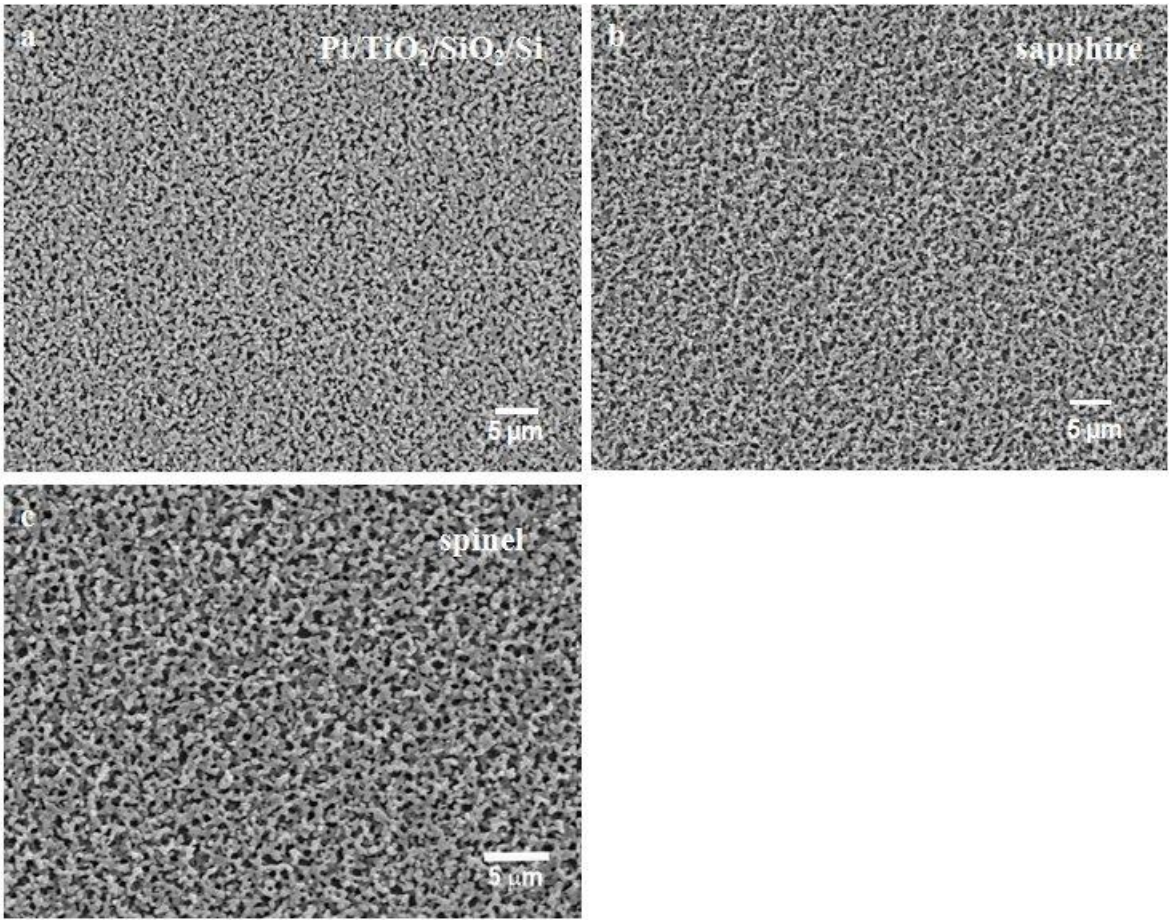

Figure 47: FE-SEM micrographs of the microstructure of thin films annealed at 700 °C deposited on substrate a) $Pt/TiO_2/SiO_2/Si$, b) sapphire, c) spinel

A large amount of water and an acid environment leads to the high condensation rate, which causes the formation of a rigid network and porous microstructure of thin films.
To obtain denser BSO thin films the rate of hydrolysis and condensation reactions of TEOS must be decreased, which can be done by reducing the R_h value or by adding the chelating agent or DCCA to the sol [72-74, 81-83].

4.2 Sol-gel R_h 5

4.2.1 Sol synthesis

One approach to circumvent the problem with the precipitation and a too excessive hydrolysis and condensation reaction was to reduce the R_h value. The R_h value can be reduced by vacuum drying of $Bi(NO_3)_3 \cdot 5H_2O$. The dried $Bi(NO_3)_3 \cdot 5H_2O$ was dissolved in acetic acid. However, such a solution was unstable and decomposed in only a few seconds due to the reaction between the Bi^{3+} ions and the water. In an acid environment, Bi^{3+} ions react easily with water to yield a white precipitate of $BiONO_3$ (Eq. 25) [63, 64].

$$Bi(NO_3)_3 + H_2O \rightarrow BiONO_3 + 2HNO_3 \quad (25)$$

According to S. H. Kim [65] stable sols can be obtained by adding the ethanolamine ($H_2NCH_2CH_2OH$) in the solution. Ethanolamine reduces the hydrolysis and condensation reaction, because it reacts with acetic acid (Eq. 26):

$$H_2NCH_2CH_2OH + CH_3COOH \rightarrow CH_3COONH_2CH_2CH_2OH \quad (26)$$

With this reaction the catalytic effect of acetic acid is reduced, therefore, the rates of the hydrolysis and condensation reactions are retard.
On the other hand, the ethanolamine is an effective complex agent of bismuth [65]. In an acidic solution the Bi^{3+} ions react with ethanolamine to yield a stable bismuth complex as follows (Eq. 27):

$$Bi^{3+} + 4\ H_2NCH_2CH_2OH \rightarrow [Bi(H_2NCH_2CH_2OH)_4]^{3+} \quad (27)$$

Ethanolamine as a complexing agent induces two major effects, that are steric hindrance and inductive effects, which reduce the reaction of water with the bismuth precursor and provides the stability of sol with time. In addition, the ethanolamine also reduces the catalytic effect of the acetic acid.
In order to confirm the formation of stable complex $[Bi(H_2NCH_2CH_2OH)_4]^{3+}$ sol R_h 5, the ATR FT-IR analysis of was preformed. Fig. 48 spectrum (a) shows the ATR FT-IR spectrum of sol R_h 5 deposited on a silicon substrate.

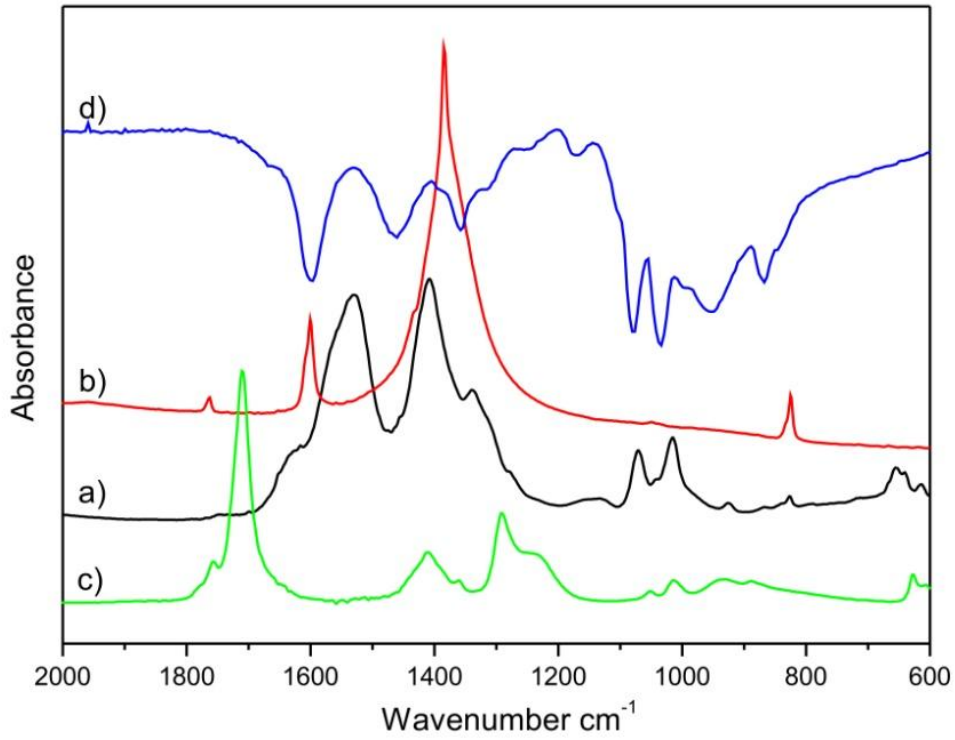

Figure 48: ATR FT-IR spectra of a) sol R_h 5 b) $Bi(NO_3)_3 \cdot 5H_2O$, c) CH_3COOH and d) ethanolamine

The formation of $[Bi(H_2NCH_2CH_2OH)_4]^{3+}$ in sol R_h 5 (spectrum (a) in Fig. 48) was confirmed by the appearance of a band at 650 cm^{-1} which is attributed to the Bi-N stretching vibrations [63]. Due to complexity of the system of sol R_h 5 were number of parallel reaction occurs, caused by use of several solvents (2-ethoxyethanol, acetic acid and ethanolamine), it is hard to determined all the bands in this spectrum. Spectra (b), (c) and (d) in Fig. 48 are attributed to $Bi(NO_3)_3 \cdot 5H_2O$, acetic acid and ethanolamine, respectively.

TEOS in the sol hydrolyzes with water and subsequently polymerizes to a three-dimensional network structure. We proposed that $[Bi(H_2NCH_2CH_2OH)_4]^{3+}$ is combined with the tetravalent silicon ion to form complex coordination, which distributes evenly in the solution.

In ordered to prepare dense and crack-free BSO thin films a study of the sols' stability, viscosity and the time of gelation must be performed. Added ethanolamine (25°C: η = 19.7 mPAs), in order to prevent the Bi^{3+} ion from hydrolysis, causes an increase in the viscosity of sol. The increased viscosity further influences the wettability of the sol and also the microstructural development of BSO thin film. We investigated the viscosity of the sols as a function of the concentration of the sol and time (Fig. 49). Fig. 49 shows that by diluting the sol with 2-ethoxyethanol, to obtain an optimal concentration for the deposition of BSO thin films, the viscosity decreases.

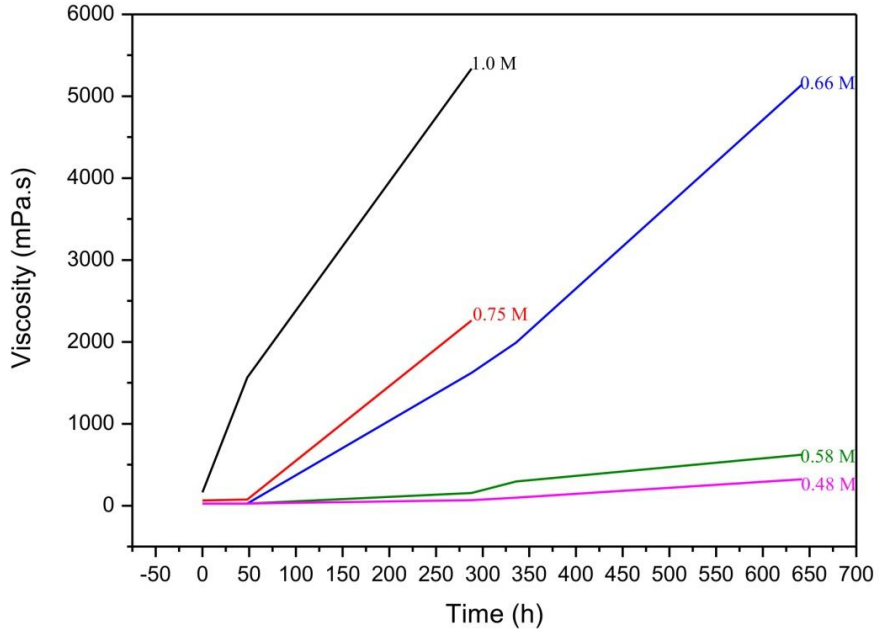

Figure 49: Dependence of the sol concentration on viscosity of sol of sol R_h 5

Important parameters for thin film deposition are also the stability of the sols and the time of gelation as a function of sol concentration (Fig. 50). Sols with R_h 5 were stable across the whole concentration range due to protection of bismuth ions with ethanolamine forming a bismuth complex which prevents the hydrolysis of the trivalent bismuth ion. An investigation of the influence of sol concentration on the time of gelation revealed the same tendency of increasing the time of gelation by decreasing the sol concentration as in sols with R_h 60. The time of gelation determined for the R_h 5 sol with a concentration of 1.1 M was 220 h, while the R_h 5 sols with a concentration of 0.48 M gelated in 723 h.

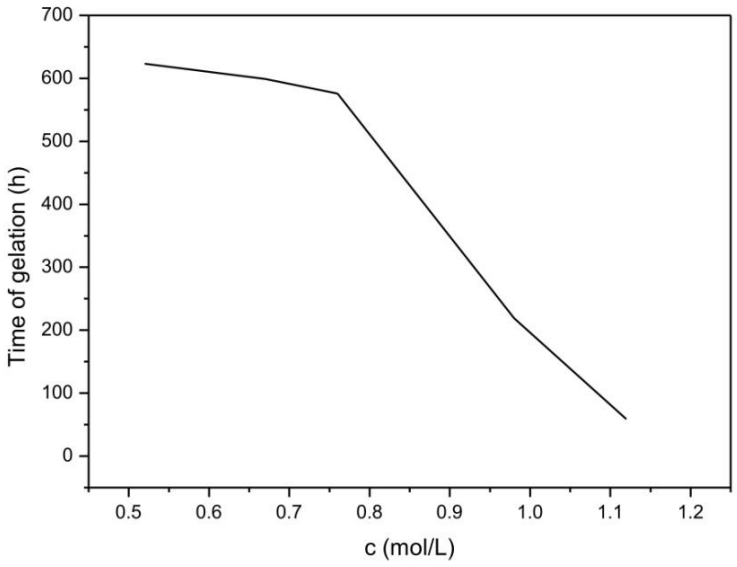

Figure 50: Dependence of the sol concentration on the time of gelation of sol R_h 5

4.2.2 Thin film deposition

Once we succeeded in going from step one (formation of stable sols), through step two (control the rate of hydrolysis and condensation), the third step is the deposition of the thin film. The FT-IR transmission spectrum of the dried thin film deposited from sol R_h 5 is shown in Fig. 51 spectrum (a).

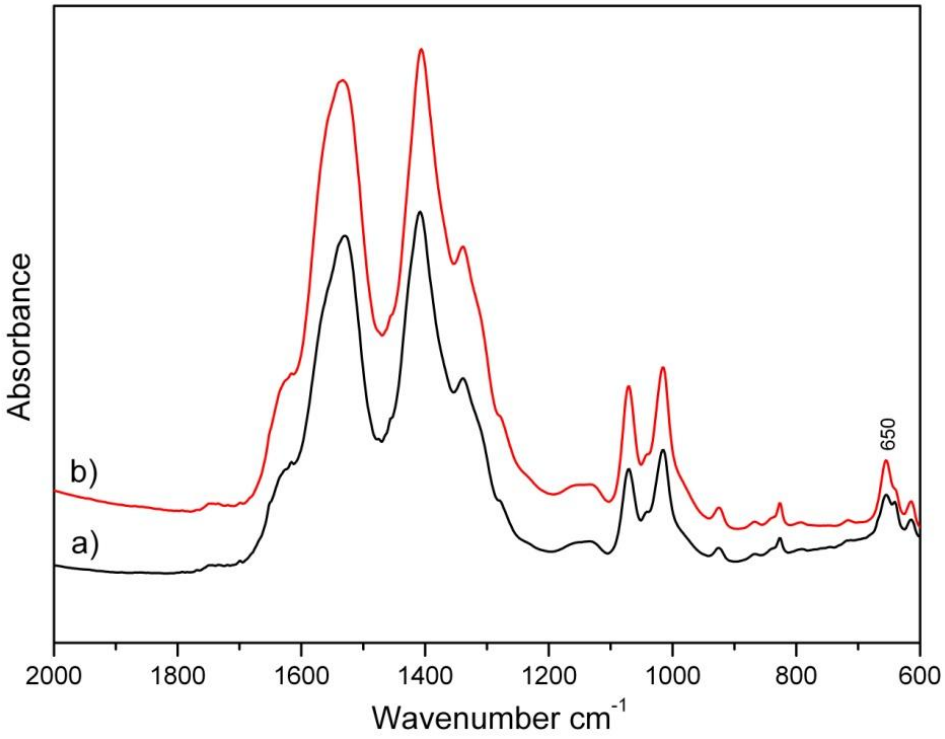

Figure 51: FT-IR of a) transmission spectra of dried thin film deposited from sol R_h 5 and b)ATR spectra of sol R_h 5

The ATR FT-IR spectrum of sol R_h5 (spectrum (b) in Fig. 51) and FT-IR transmission spectrum of dried thin film (spectrum (a) in Fig. 51) deposited from sol R_h 5 are nearly identical. A band at 650 cm^{-1} belonging to Bi-N stretching vibration, indicating that a new compound, $[Bi(H_2NCH_2CH_2OH)_4]^{3+}$ is also present in the dried thin film.

In order to determine the phases present in the dried thin film a TEM analysis was performed, shown in Fig. 52. The dried thin film consisted of small particles (nucleus), which are the agglomerate and the amorphous phase. Due to small particle size the electron diffraction of the particle together with energy-dispersive spectroscopy could not be carried out. Therefore, the phase structure and composition were not determined.

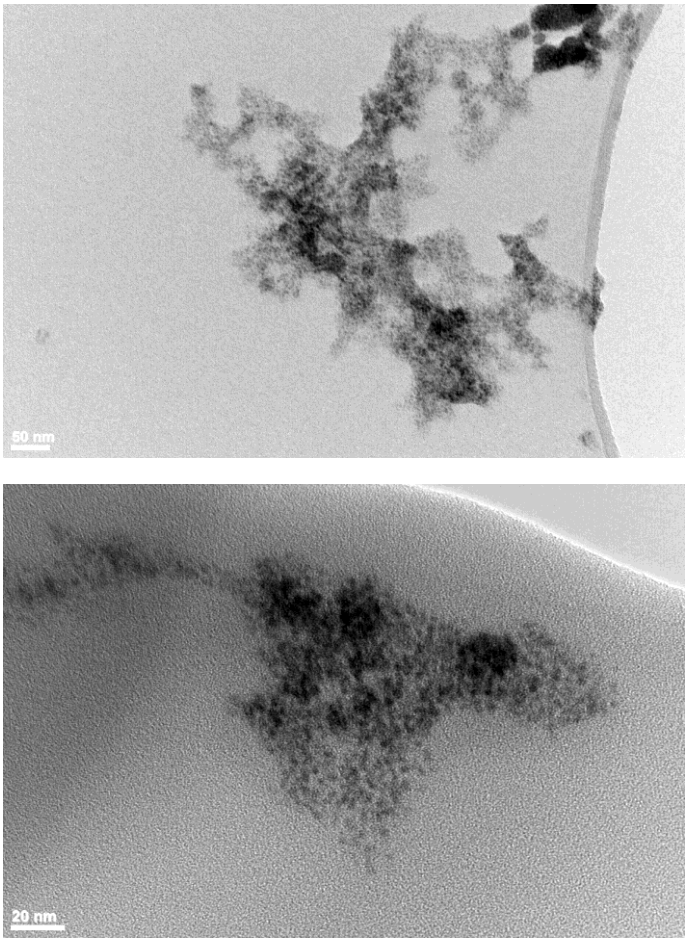

Figure 52: TEM analysis of dried thin film deposited from sol R_h 5

The next step in thin film synthesis is pre-heating of the thin film. During the pre-heating (pyrolysis), two mechanisms occur, i.e., gelation and solvent evaporation, which have great influence on the subsequent microstructural development. The pre-heating temperature of BSO thin films was determined with the help of thermoanalysis (TA) of xerogels and thin films. Thermoanalytical studies of the changes in the thin films are difficult due to the small sample size. Therefore, it was initially done on xerogels to determine their decomposition behavior. The obtained TA results of xerogels helped us in the determination of the thin films decomposition behavior and the pre-heating temperature.

Results from the thermogravimetric (TGA) and differential analysis (DTA) curves and the corresponding evolved gas analysis curves (EGA) of the xerogel of the sol R_h 5 are shown in Fig. 53. The mass peaks of water H_2O ($m/e^+ = 18$), carbon dioxide CO_2 ($m/e^+ = 44$) and nitrogen dioxide NO_2 ($m/e^+ = 46$) were followed on the EGA curves. The decomposition process has been divided into four consecutive steps. The highest weight loss, 31%, observed in the first step starting from room temperature up to 120°C is believed to be due to the volatilisation of water, which is associated with a small endothermic peak recorded in the DTA curve. In addition, the decomposition of the inorganic and organic matter begins. The subsequent weight losses, 19 % and 16 %, are accompanied by an exothermic process. In these steps the EGA curves show the evolution of water and carbon dioxide. The nitrogen dioxide is also detected. The main exothermic process detected in the temperature range between 245°C and 360°C, with weight loss 8 %, corresponds to the nitrate elimination and is accompanied by the elimination of CO_2 and H_2O. The thermal decomposition of the xerogel's sol R_h 5 was completed at 550°C. Aşmall weight loss of 1.1 %, due to elimination of nitrates, was detected. This weight loss is accompanied by a small DTA peak.

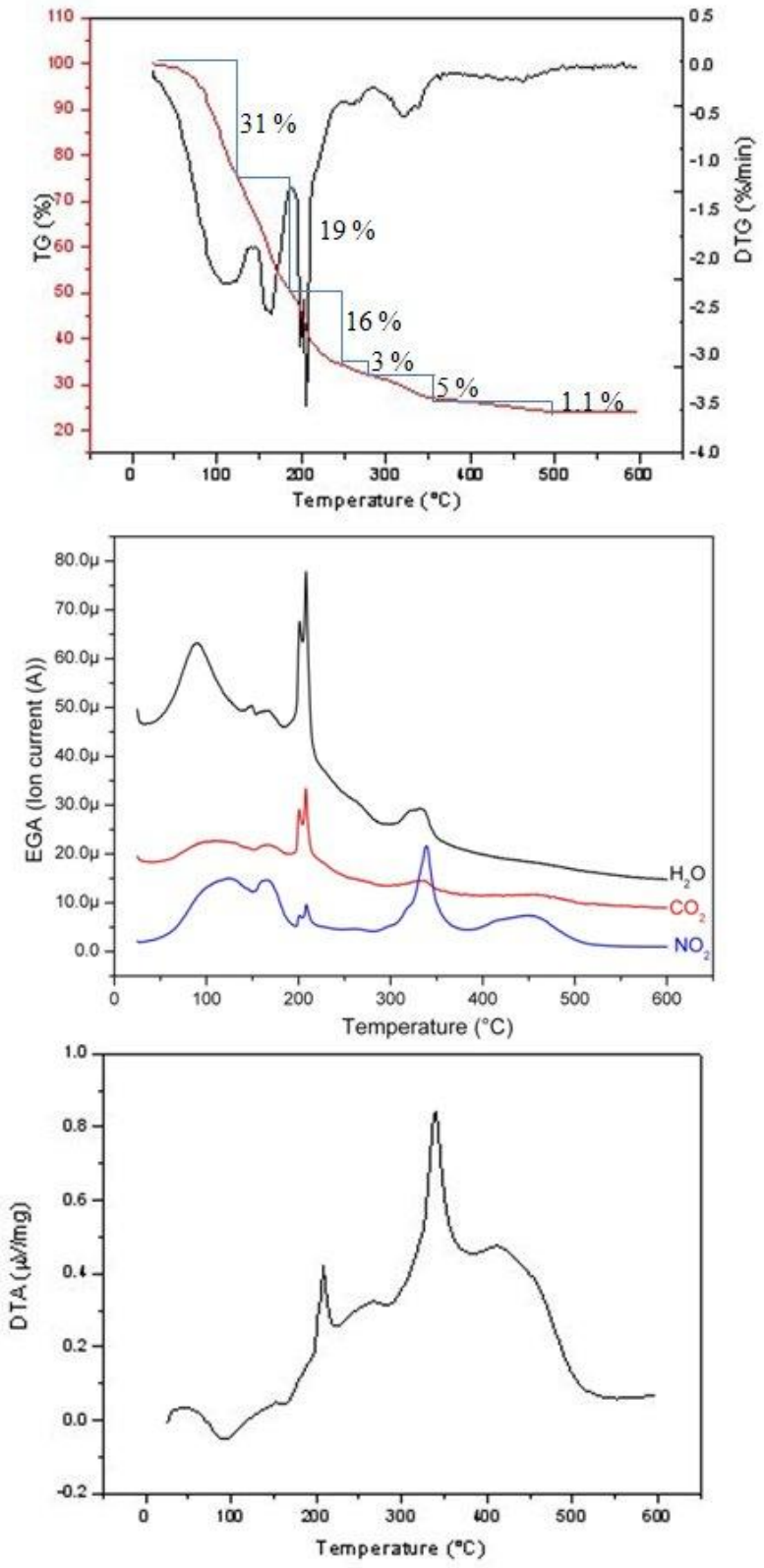

Figure 53: TG/DTG/EGA/DTA curves of xerogel of sol R_h 5

When the sample is prepared as a thin film or in powder form, the differences in the particle size and in the microstructure of the two forms led to different thermal stabilities [45]. The decomposition temperatures decrease with decrease in the particle size of the sample [45]. Due to the nano-dimensions of the thin films the thermal decomposition occurs at a lower temperature than that of xerogels. The determination of thin films' pre-heating temperature from the obtained thermoanalysis (TA) of xerogels can lead to a misinterpretation

of the results. Therefore, it was essential to perform the TG/DSC analysis on thin films deposited from sol R_h 5. The TG and DSC analyses of the thin film deposited from the sol R_h 5 are shown in Fig. 54.

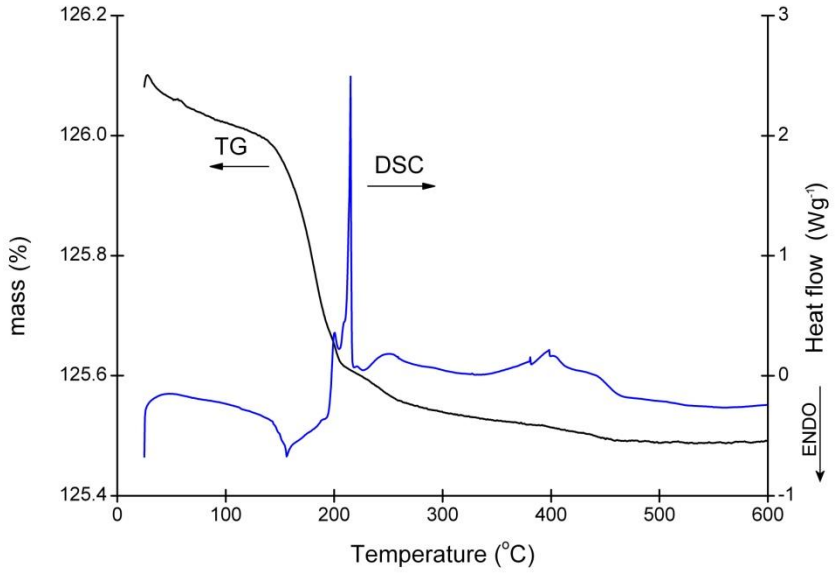

Figure 54: TG/DSC curves of thin film deposited from sol R_h 5

The results of the TG analysis shows a small decrease in the weight up to 150°C which can be attributed to the evaporation of water. While a large decrease in the weight in the temperature range between 150 and 240°C corresponds to decomposition of organic and inorganic matter. In the DSC curve the large exothermic peaks were observed at 200°C and 220°C. In addition, a series of small exothermic peaks from 240°C and 450°C were observed. From the TG/DTA/EGA result of the xerogel (Fig. 53) these peaks can belong to a decomposition of the remaining inorganic and organic matter. The thermal decomposition of the BSO thin film was completed at 500°C. By comparing the thermoanalysis results of the xerogel and thin film, we observed that the most intensive decomposition occurs for the thin film at lower temperature than for the amorphous xerogel. From these results, we determined that the pre-heating temperature for the preparation of BSO thin films was 250°C.

As already mentioned, the pre-heating temperature of the BSO thin film is a very important parameter of sol-gel derived BSO thin film. Too low a pre-heating temperature usually results in a porous microstructure of the thin films, while too high a pre-heating temperature might results in stress formation, causing peeling of the BSO thin film from the substrate. Fig. 55 shows a SEM micrograph of a BSO thin film deposited on a $Pt/TiO_2/SiO_2/Si$ substrate, pre-heated at 300°C and annealed at 700°C. Too high a pre-heating temperature caused rapid volatilization of the solvent, residual organic and nitrate groups, as a consequence too much stress forms during the decomposition and as a final result peeling of BSO thin film from the substrate occurs. The high interfacial adhesion strength is desirable and critical in order to avoid any delamination, cracking or peeling of the BSO thin film from the substrate or a suitable pre-heated temperature has to be chosen.

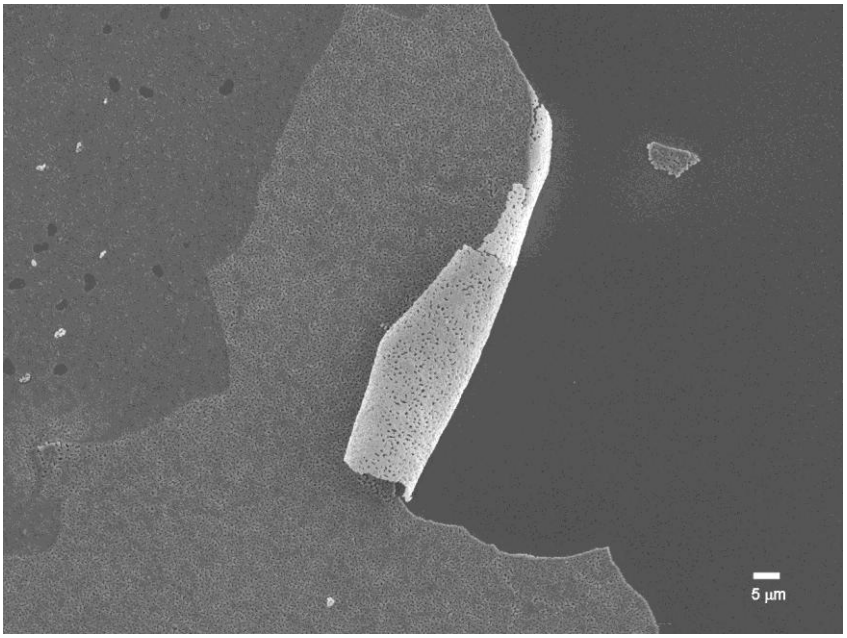

Figure 55: SEM micrograph of peeling of BSO thin film deposited on $Pt/TiO_2/SiO_2/Si$ substrate, pre-heated at 300°C and annealed at 700°C

To obtain a single BSO phase in pre-heated thin films annealing at 700°C must be carried out. The X-ray diffraction pattern of the thin film annealed at 700°C for 1 h shows the formation of a single phase BSO thin film (Fig. 56). The same result was observed when sapphire and spinel substrates were used.

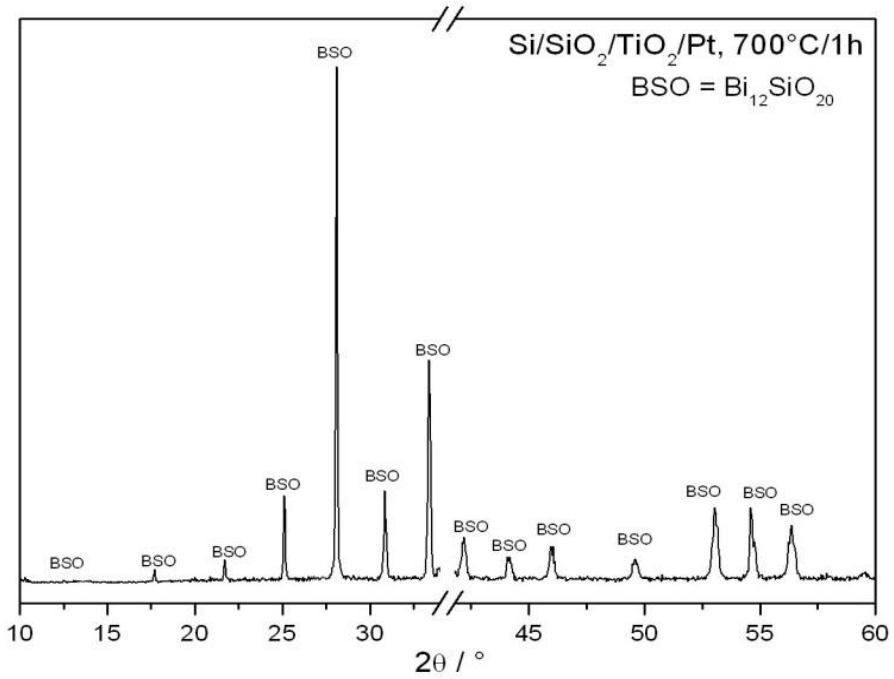

Figure 56: X-ray diffraction pattern of BSO thin film deposited on $Pt/TiO_2/SiO_2/Si$ substrate annealed at 700°C, for 1

In order to study the influence of the substrate on the microstructural development of BSO thin films they were characterized by FE-SEM. Fig. 57-59 show FE-SEM micrographs of the microstructures and cross-sections of BSO thin films prepared on $Pt/TiO_2/SiO_2/Si$, sapphire and spinel substrates and annealed at 700°C for 1h. On the $Pt/TiO_2/SiO_2/Si$ substrate (Fig. 57)

a 200 nm thickness of thin film was obtained. The deposition of the BSO thin film on the sapphire substrate under the same conditions (Fig. 58) resulted in 400 nm thickness, while on the spinel substrate (Fig. 59) the thickness of the BSO thin film was 300 nm.
Fig. 57 shows the homogeneous bimodal microstructure of the BSO thin film on a $Pt/TiO_2/SiO_2/Si$ substrate, where grains with an average size from 500 to 1000 nm were observed and the presence of pores was apparent. The microstructures of the BSO thin films deposited on sapphire substrates, as shown in Fig. 58, does not result in a dense BSO thin film. Meanwhile, the microstructure of a BSO thin film deposited on a spinel substrate, as shown in Fig. 59, shows grains with an average size from 200 to 400 nm and a rather dense microstructure.

From the observed microstructures of the BSO thin films (Fig. 57-59) one can conclude that the rate of hydrolysis and condensation is reduced by the reaction between acetic acid and ethanolamine (Eq. 26, pp. 20). Therefore, solvents evaporates before the gelation is completed, resulting in dense thin films.

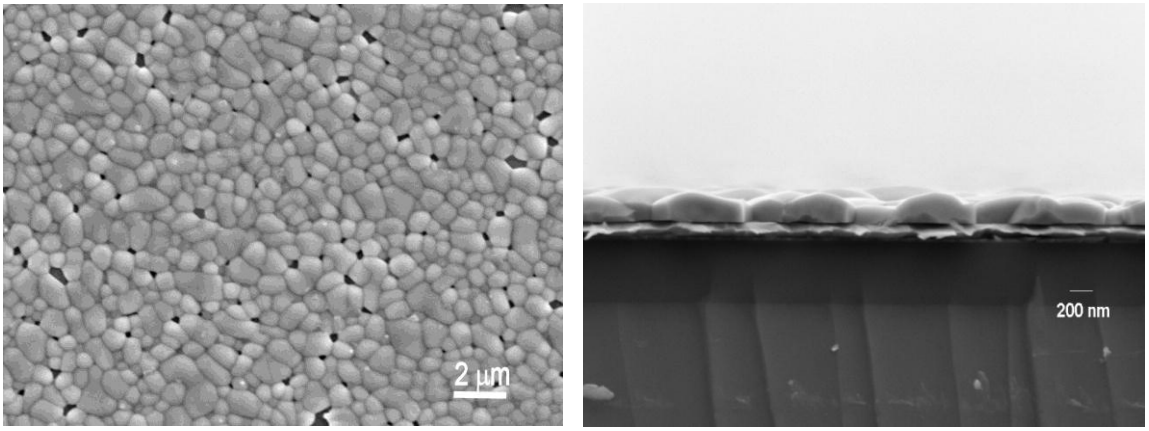

Figure 57: FE-SEM micrographs of the microstructures and cross-sections of BSO thin films prepared at 700°C for 1h, deposited from the R_h 5 sol on a $Pt/TiO_2/SiO_2/Si$ substrate

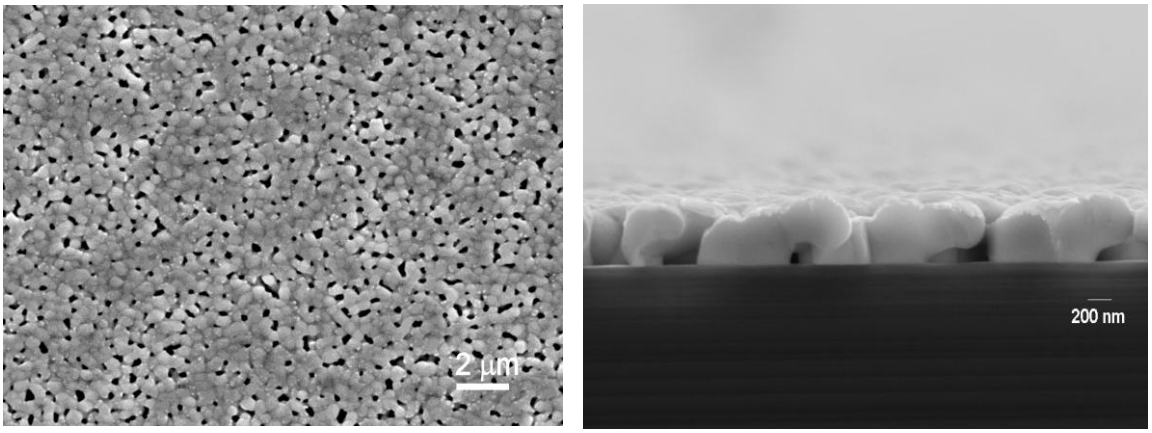

Figure 58: FE-SEM micrographs of the microstructure and cross-sections of BSO thin films prepared at 700°C for 1h, deposited from the R_h 5 sol on a sapphire substrate

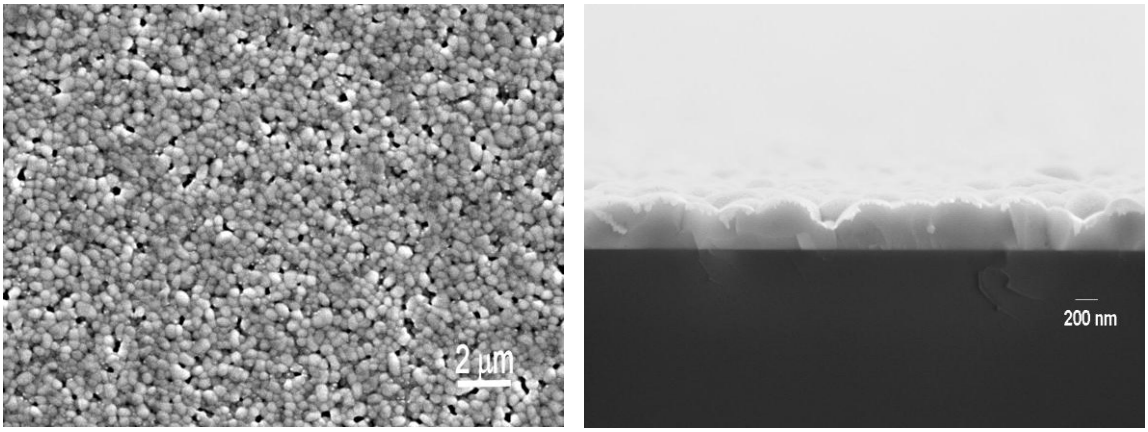

Figure 59: FE-SEM micrographs of the microstructures and cross-sections of BSO thin films prepared at 700°C for 1h, deposited from the R_h 5 sol on a spinel substrate.

As evident from Fig. 57-59, the grain size of the BSO thin film deposited on $Pt/TiO_2/SiO_2/Si$ substrate was larger than that of the BSO thin film deposited on sapphire or spinel substrates. In addition, the porosity of the BSO thin films vary depending on the selected substrate. The differences of the morphology of BSO thin films on different substrates were attributed to several different effects, such as the thermal conductivity of the substrate, the interfacial energy between the BSO thin film and the substrate, the elastic strain energy of the thin film and the substrate and different lattice mismatch between the substrate and BSO thin film, which are directly influencing the nucleation and growth dynamics.

A cross-section of the sol-gel-derived BSO thin films on $Pt/TiO_2/SiO_2/Si$, spinel and sapphire substrate shows a columnar microstructure. Fig. 60 shows the results of a modelling study for the columnar microstructure evolution of BSO thin films. In columnar growth the nucleation occurs only at the substrate interface caused by the heterogeneous nucleation. Grain growth from these nuclei proceeds toward the surface. Because of such a type of nucleation and growth behaviour, BSO thin films are one single grain thick. Speck and co-workers [145] have shown that for materials which formed from individual elements or oxides of one or more elements the crystallization driving force is reduced by the formation of this phase, resulting in films that display only heterogeneous nucleation at the substrate interface and by this causing the columnar structure of the thin film. Their observation additionally confirms the columnar growth of the BSO thin films.

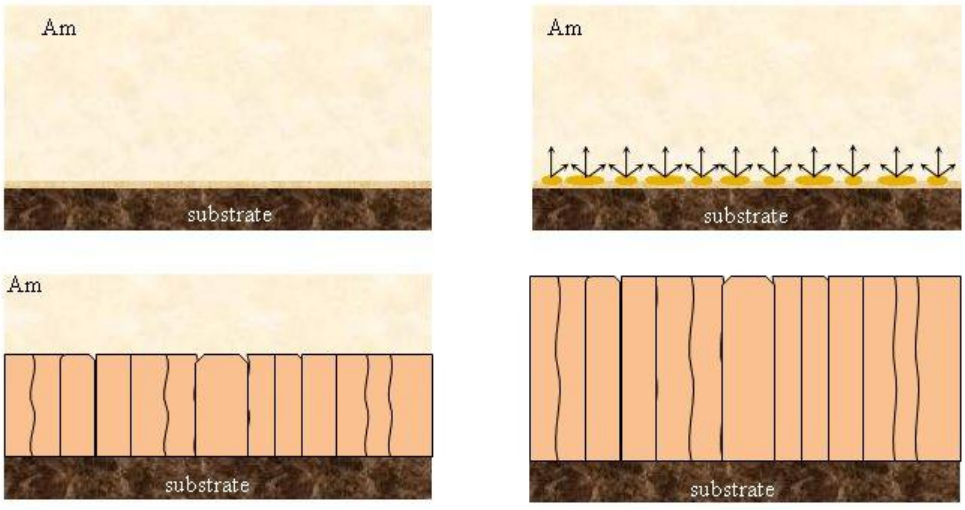

Figure 60: The image of the modelling study of the microstructure evolution of BSO thin film

Atomic force microscopy (AFM) was used to evaluate the surface roughness of the synthesized BSO thin films. Roughness of thin film is extremely important for device performance since dielectric properties depend not only on a well-defined microstructure but also on the quality of the electrode–thin-film interface. Fig. 61 shows atomic force micrographs of BSO thin films deposited on $Pt/TiO_2/SiO_2/Si$, sapphire and spinel substrates and annealed at 700°C for 1h. On the $Pt/TiO_2/SiO_2/Si$ and spinel substrates the surfaces of the BSO thin films appear to be smooth, while on the sapphire substrate the surface is relatively rough. The average roughness (R_a) measured by AFM ranged from 50 to 60 nm for the $Pt/TiO_2/SiO_2/Si$ substrate and 20 to 30 nm for the spinel substrate, while the average roughness (R_a) of the BSO thin film deposited on the sapphire substrate was as high as 100 to 120 nm.

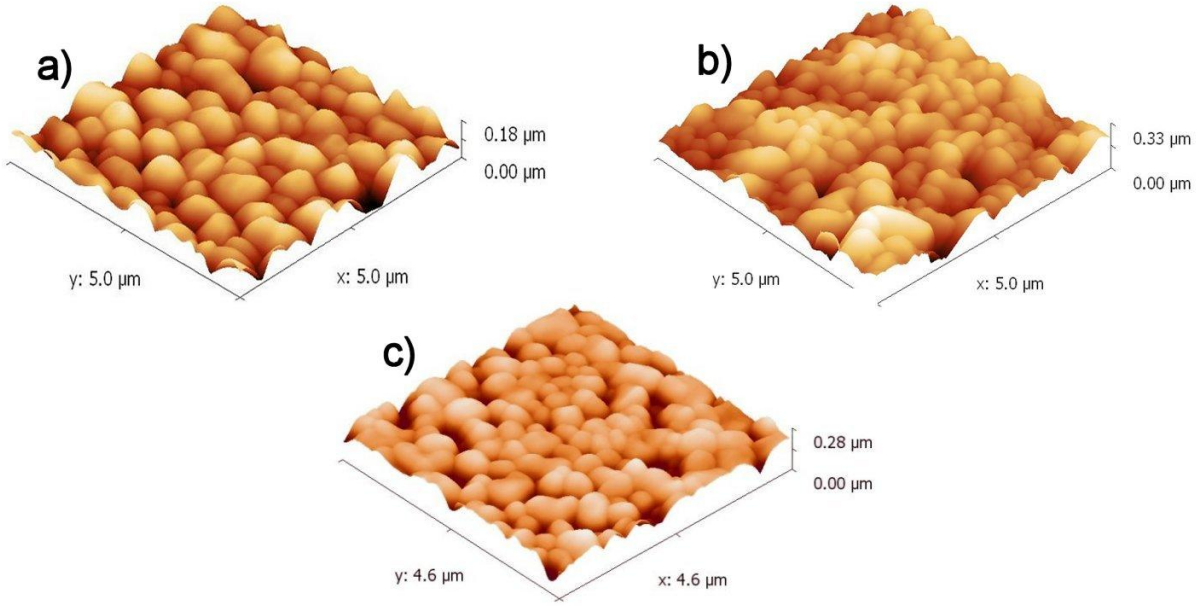

Figure 61: AFM micrographs of BSO thin films annealed at 700°C, deposited from the R_h 5 sol on a) $Pt/TiO_2/SiO_2/Si$, b) sapphire and c) spinel substrates

The microstructural development of BSO thin films deposited from sol R_h 5 is strongly influenced by the substrate. We believe that the influence of the substrate on thin films is preserved due to poor wettability of sol R_h 5. The wettability characteristic can be evaluated from the SEM analysis of thin films containing one layer or multi-layers. Fig. 62 shows the microstructure of 1-layer and 3-layered BSO thin films deposited on sapphire substrate and annealed at 700°C for 1 h. In the 1-layer thin film (Fig. 62 a) we observed that the sol R_h 5 is not homogeneously spread throughout the substrate. A further deposition of the sol fills the empty spaces between the drops of the thin film (Fig. 62 b). This result suggests that the influence of the substrate is preserved through the pre-heating and annealing of the BSO thin film.

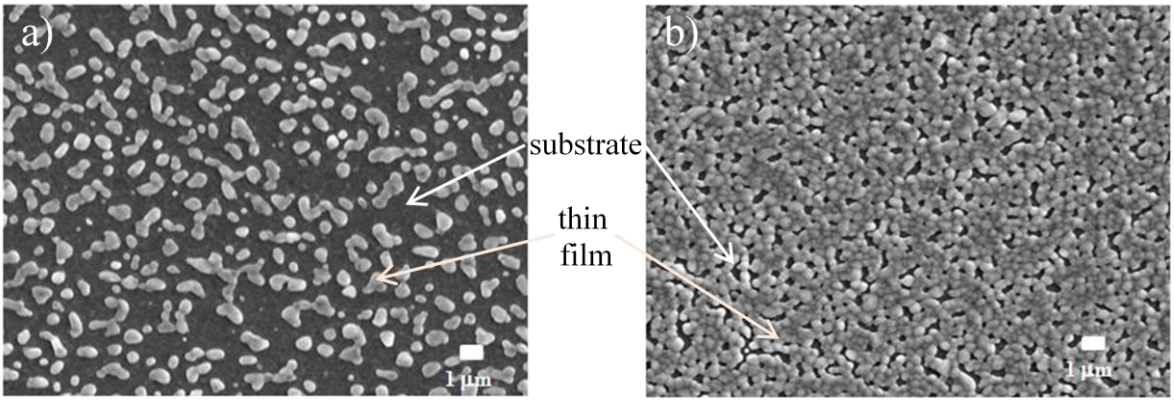

Figure 62: SEM micrograph of a) 1-layer BSO thin film and b) 3-layer BSO thin film deposited on sapphire substrate and annealed at 700°C, for 1 h

4.3 Sol-gel R_h 60 with DCCA

4.3.1 Sol synthesis-AcOH

Acetic acid (AcOH) as solvent

Base on results achieved in syntheses of sol R_h 60 and R_h 5 carried out in this thesis one can conclude that bismuth nitrate is prone to re-crystallization and forming precipitates in sols. In addition, 2-ethoxyethanol promotes the re-crystallization of bismuth nitrate by esterfication. Furthermore, sols with R_h 60 exhibit a high rate of the hydrolysis and condensation reaction. In contrast, in sol R_h 5, the ethanolamine reacts with bismuth nitrate forming a stable complex and in this way preventing the formation of precipitates in sols. The disadvantage of using ethanolamine as a stabilizer is in its high viscosity, consequently causing the high viscosity of the sol and by this poor wetability of the substrate. In addition, to reduce the amount of water in the sol the $Bi(NO_3)_3{\cdot}5H_2O$ must be vacuum dried for at least 96 h. After dissolving dried $Bi(NO_3)_3$ in acetic acid, and before ethanolamine is added, bismuth nitrate has a very high tendency for re-crystallization.

Due to the precipitation of bismuth nitrate in sols with R_h 60 and R_h 5 and esterification of 2-ethoxyethanol, we have tried to prepare a stable sol using only acetic acid as the solvent and un-dried $Bi(NO_3)_3{\cdot}5H_2O$ as the precursor. In addition, an aprotic solvent formamide, which belongs to the group of drying controlled chemical additives (DCCA), was used to retard the acid-catalyzed condensation [81]. Under acid conditions the hydroxylated monomer is formed from protonated alkoxide group where the electron density is withdrawn from the silicon atom, making it more electrophilic and thus more susceptible to attack from water. The condensation reaction continues from these hydroxolated monomers. The aprotic solvent, formamide (DCCA), implies a slight change in the catalytic effect of acetic acid, by bonding to protons and as a consequence, retarding the rate of hydrolysis and condensation reactions. It is known [116] that in general, the gel consists of two phases, the network solid phase and of connected pores filled with liquid phase [116]. When the heat-treatment is applied, the gel shrinks under capillary force as the liquid evaporates. The addition of formamide (DCCA) to the precursor solution is believed not only to reduce the catalytic effect of the acetic acid and narrow the distribution of pore sizes but also to increase the pore size, which then reduces the drying stress and capillary force in pore formation.

The structural changes that occur in the sol synthesis were studied with ATR FT-IR spectroscopy. Fig. 63 show the ATR FT-IR spectrum of sol R_h 60 with DCCA (formamide).

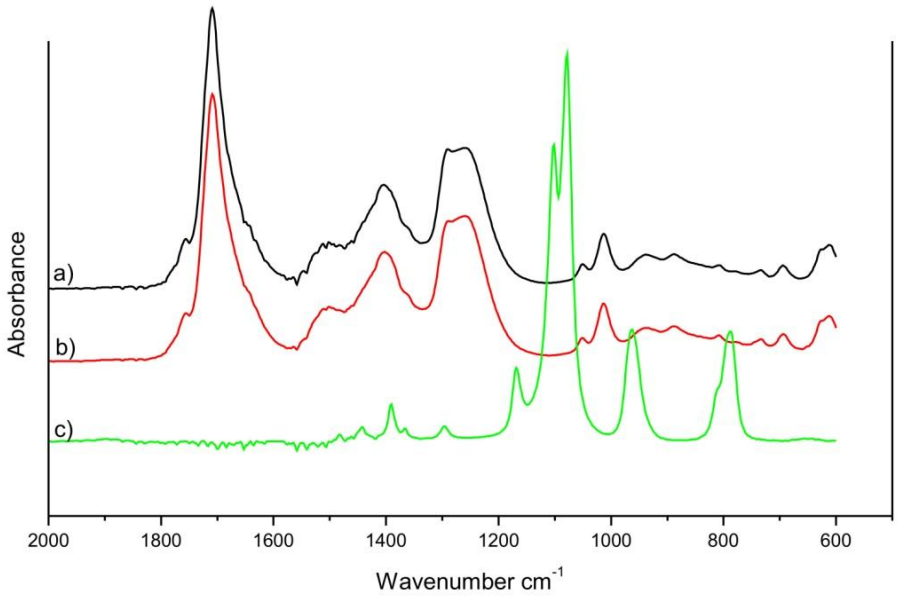

Figure 63: ATR FT-IR spectra of a) sol R_h 60 with DCCA b) $Bi(NO_3)_3 \cdot 5H_2O$-CH_3COOH solution c) TEOS

The ATR FT-IR spectrum (a) of sol R_h 60 with DCCA exhibits absorption bands at 1756, 1708, 1505, 1403, 1290, 1260, 1053, 1013, 973, 887, 808, 734, 694 and 612 cm^{-1}. Fig. 63 spectrum (b) and Fig. 63 spectrum (c) show spectrums of already-described $Bi(NO_3)_3 \cdot 5H_2O$-CH_3COOH solution and TEOS, respectively. It is important to note that the ATR FT-IR spectrum of the sol R_h 60, with DCCA (spectrum (a) in Fig. 63) and the spectrum of $Bi(NO_3)_3 \cdot 5H_2O$-CH_3COOH solution (spectrum (c) in Fig. 63) overlap, no additional bands are observed. As already described, in the spectrum of the $Bi(NO_3)_3 \cdot 5H_2O$-CH_3COOH solution (Fig. 29), carboxylate ligands are bidentately coordinated to the bismuth ion. The same coordination of bismuth ions appears in sols R_h 60 with DCCA, which indicates that the coordination sphere of the bismuth remains unchanged after the sol synthesis. The above ATR FT-IR results indicated that DCCA (formamide) does not have a significant influence on the coordination sphere of the bismuth ions. The predominant effect on the coordination in sol R_h 60 with DCCA comes from the acetic acid. Because the carboxylate groups act as bidentate chelating ligands and by this forming stable complex, the precipitates in the sol do not appear. Therefore, sols R_h 60 with DCCA are stable in the whole concentration range.

The influence of the concentration of sols on the viscosity of the sols as a function of time is shown in Fig. 64. The concentration of the sol was varied from 0.5 M to 1.2 M. We observed that the viscosity of the sol decreases with the decreasing sol concentration and the increase with time due to the expanding condensation reaction.

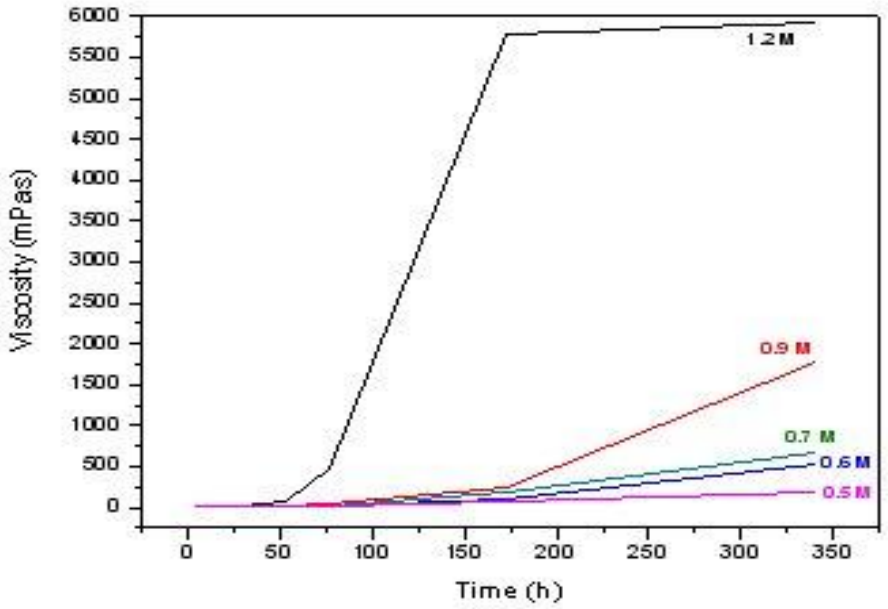

Figure 64: Dependence of the sol concentration on the viscosity of sol R_h 60 with DCCA

Fig. 65 shows the influence of sol concentration on the time of gelation. One can observe that by decreasing the sol concentration the time of gelation is increasing. In addition, sols R_h 60 with DCCA are stable in the whole concentration range. The time of gelation for the sol with concentration of 1.2 M was 28 h, while the sol with a concentration of 0.5 M gelated in 350 h.

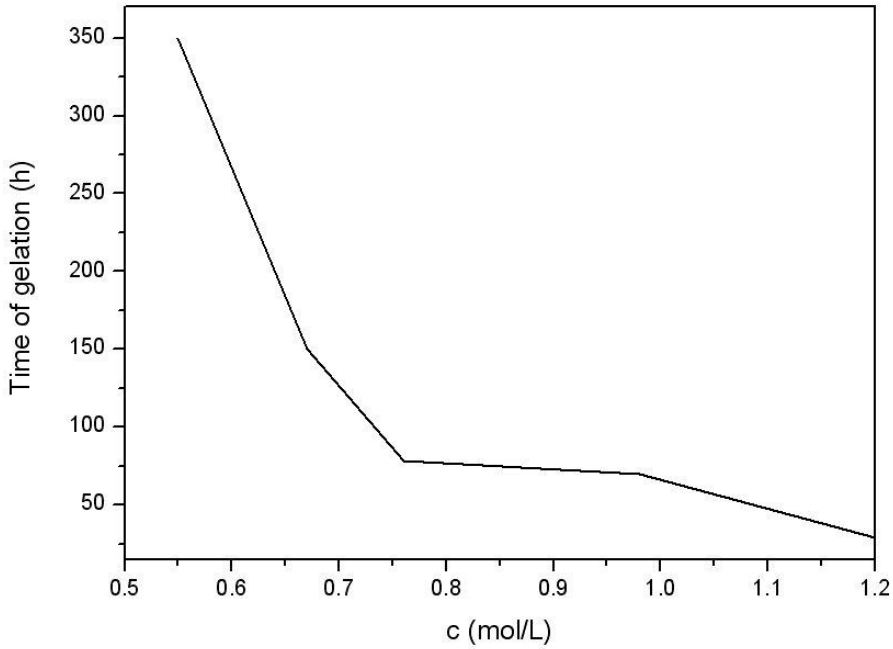

Figure 65: Dependence of the sol concentration on the time of gelation of sol R_h 60 with DCCA

4.3.2 Thin film deposition-AcOH

After the sol synthesis the deposition of the thin film takes place. During the deposition the solvent evaporates, therefore the concentration of precursor increases, causing an acceleration of the hydrolysis and condensation reactions.

The FT-IR transmission spectrum of the thermally untreated thin film deposited from the sol R_h 60 with DCCA shown in Fig. 66, exhibits bands located at 1670 cm^{-1} and 1288 cm^{-1}, which are ascribed to the asymmetric and symmetric vibrations of the C=O groups bonded on the organic (-CH_3) groups and monodentately coordinated to the bismuth ion [87]. The bands at 1575 cm^{-1} and 1490 cm^{-1} are attributed to the asymmetric (ν_a(COO)) and symmetric (ν_s(COO)) vibrations of the carboxylate groups [87]. The frequency separation $\Delta\nu$=80 suggest that the bismuth ion is bidentately coordinated [87]. The absorption band centered at 1087 cm^{-1} was attributed to the Si-O-Si asymmetric stretching vibration [141]. The bands located at 1018 cm^{-1}, 697 cm^{-1} and 621 cm^{-1} were associated with the vibration of the acetate groups bonded to the bismuth ion. The bands at 805 cm^{-1} and 734 cm^{-1} were related to the vibration of the N-O out-of-plane and in-plane bands [141]. From FT-IR results one can see that the coordination of the bismuth ion remains unchanged after the deposition of the sol R_h 60 with DCCA.

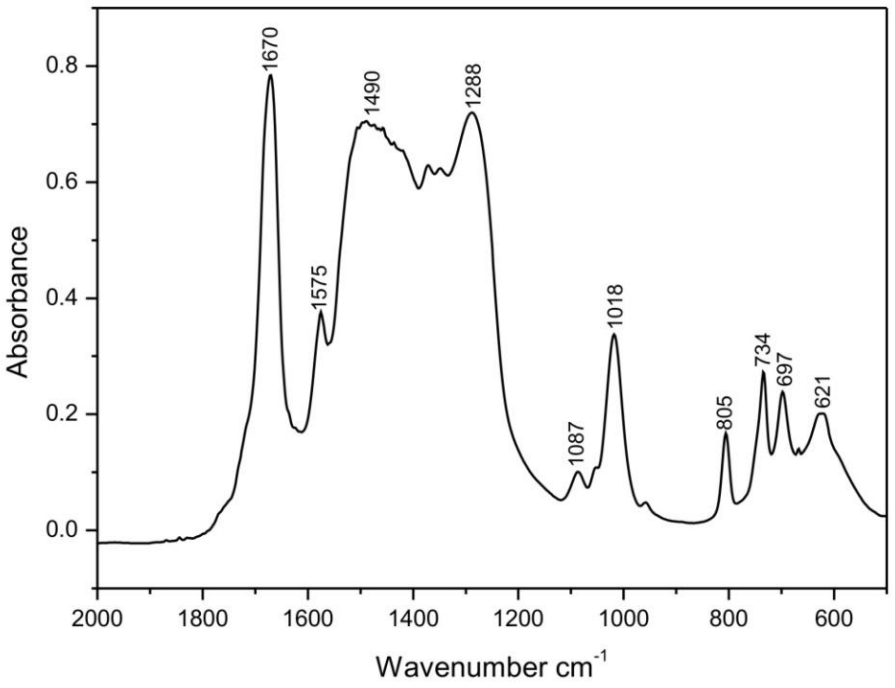

Figure 66: FT-IR transmission spectra of thin film deposited from sol R_h 60 with DCCA deposited on the silicon substrate

Fig. 67 shows a TEM micrograph of dried thin film deposited from sol R_h 60 with DCCA. TEM micrograph of dried thin film reveals nano-sized particles, which are agglomerated. No crystalline particles of δ-Bi_2O_3 were observed in the dried thin film, so we presumed that at the given conditions using only acetic acid as a solvent the growth of the crystallites is stopped. The same behaviour was also observed for thin films deposited from sol R_h 5 (Fig. 52). It seems that in the case when the bismuth forms a stable complex, causing stable sols,

the growth of the particles is hindered and very small particles are formed in the dried thin films.

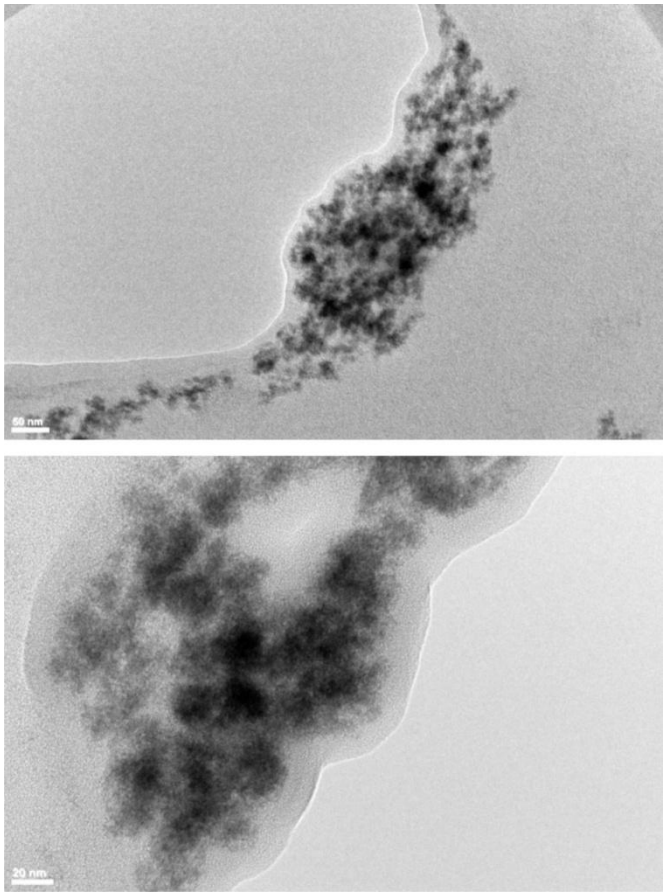

Figure 67: TEM analysis of dried thin film deposited from sol R_h 60 with DCCA

In a sol-gel process, before the thin film is subjected to high-temperature annealing, the BSO thin film would predominantly contain a network of Bi, Si and O atoms in amorphous form. To determine the pre-heating temperature of the BSO thin film a thermoanalysis of xerogel and thin film was preformed.

The thermoanalysis TG/DTG/EGA/DTA curves of the xerogel are shown in Fig. 68. The sample loses 44.95 % mass upon heating to 550°C. The thermal decomposition occurs stepwise: the mass loss from room temperature to 185 °C is 3.3 %, from 185 to 270°C 26.8 %, from 270 to 330°C 7.9 %, from 330 to 445°C 4.6 % and upon further heating to 550°C 2.27 %. The thermal effects recorded by DTA include an endothermic effect at 95°C, and a succession of exothermic peaks between 170 and 500°C, with the strongest peaks at 245°C and 295°C. We followed the mass peaks of water ($m/e^+ = 18$), carbon dioxide ($m/e^+ = 44$) and nitrogen dioxide ($m/e^+ = 46$). Between room temperature and 170°C, the first step of the mass loss was due to the evaporation of solvents. In addition, nitrate groups and some organic matter starts to decompose. In the second two step of mass loss, between 170°C and 330°C, water, nitrogen dioxide and carbon dioxide are evolved. Upon further heating to 550°C only the nitrogen dioxide peaks are detected.

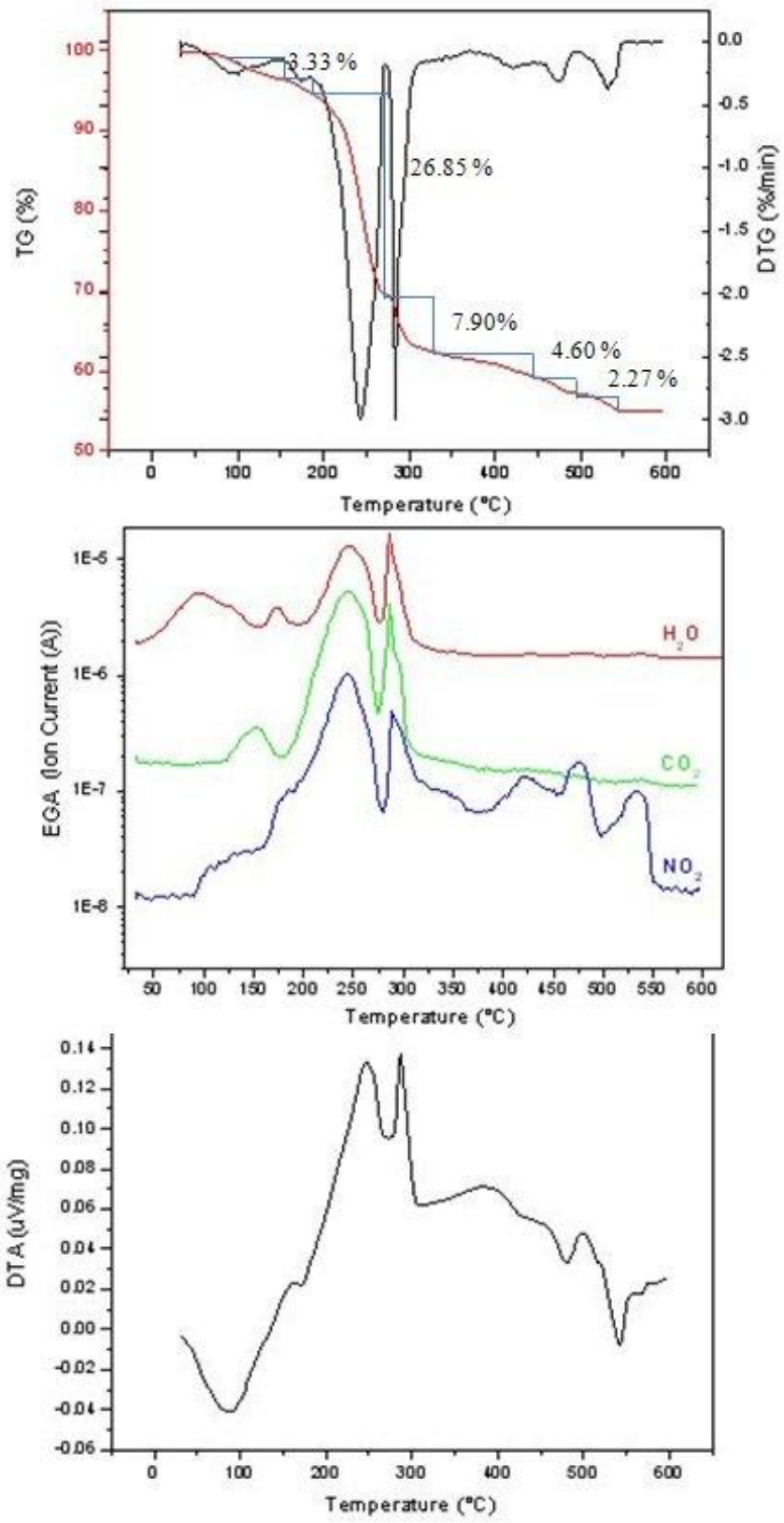

Figure 68: TG/DTG/EGA/DTA curves of xerogel of sol R_h 60 with DCCA

The TG/DSC analysis of the thin film deposited on the $Pt/TiO_2/SiO_2/Si$ substrate from sol R_h 60 with DCCA is shown in Fig. 69.

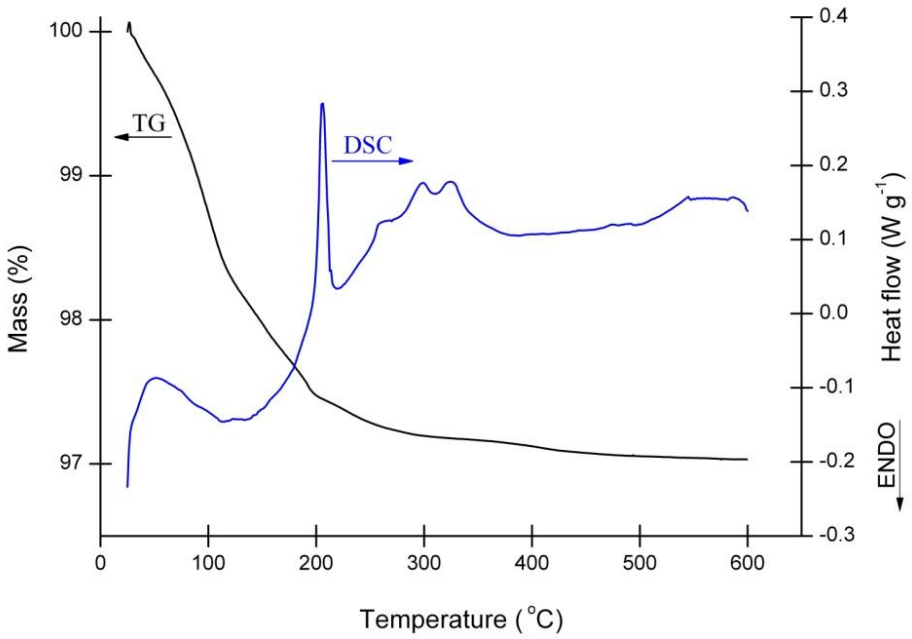

Figure 69: TG/DSC curves of thin film deposited from sol R_h 60, with DCCA

From the TG curve it was observed that a large decrease in the weight takes place in the temperature range between room temperature and 250°C, corresponding to the evaporation of water, residual organic and nitrate compounds. In the DSC curve the large exothermic peak is observed at 220°C and a succession of small exothermic peaks between 250 and 350°C. We believe that the exothermic peak at 200°C corresponds to the decomposition of organic and nitrates compounds, whereas the peaks between 250 and 350°C correspond to the evaporation of nitrogen dioxide. The thermal decomposition of the BSO thin film was completed at 500°C. From the results of the TG/DTG/EGA/DTA of xerogel (Fig. 68) and TG/DSC of thin film (Fig. 69) the pre-heating temperature of 250°C was used for the BSO thin-film preparation.

The X-ray pattern of the thin film deposited on the $Pt/TiO_2/SiO_2/Si$ substrate annealed at 700°C for 1 h is shown in Fig. 70.

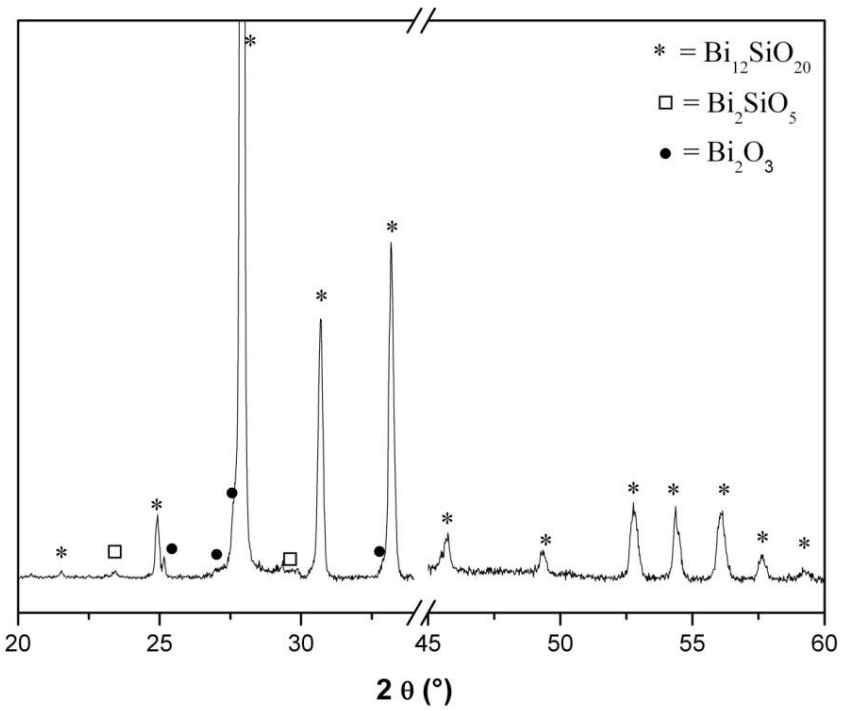

Figure 70: X-ray diffraction pattern of thin film deposited on a sapphire substrate annealed at 700°C/1 h

From Fig. 70 one can see that most of reflections belong to the sillenite phase, however the formation of secondary phases Bi_2O_3 and Bi_2SiO_5 was also observed. We believe that the formation of secondary phases resulted from the change in the coordination sphere of the bismuth. According to S. Tirumala and co-workers [146], the extent of the oligomerization of Bi-precursor influences the crystallization kinetics of the $SrBi_2Ta_2O_9$ thin films. High oligomerization of Bi-precursor leads to the formation of a large amount of secondary phases in the $SrBi_2Ta_2O_9$ thin films. In the case of the BSO thin film synthesis, where acetic acid was used as a solvent, the FT-IR transmission analysis of dried BSO thin film (Fig. 66) reveals that bismuth is no longer coordinated with nitrate ligands. Acetic acid serves as a chelating agent and carboxylate bidentately coordinates bismuth ions. With this coordination the bismuth precursor has the opportunity to oligomarate. Extended oligomerization of bismuth precursor causes the appearance of secondary phase in the BSO thin films.

To optimize the amount of formamide in the sols, the microstructural development of BSO thin films was studied by FE-SEM. Fig. 71 shows the microstructural development of a BSO thin film deposited on a $Pt/TiO_2/SiO_2/Si$ substrate from the sol R_h 60 with 4 % of formamide (DCCA). The BSO thin film was annealed at 700°C for 1h.

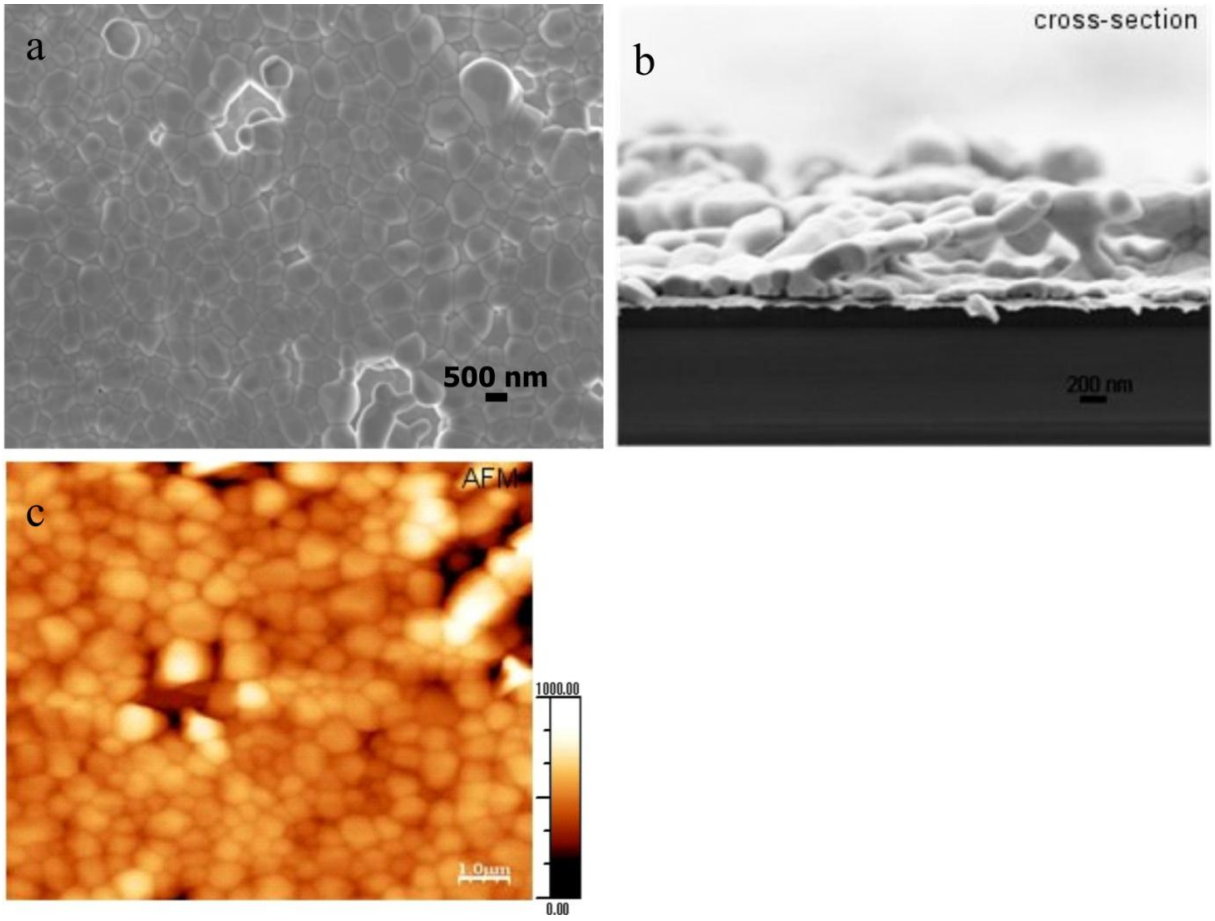

Figure 71: FE-SEM micrographs of the a) microstructure, b) cross-section and c) AFM of BSO thin film deposited from sol R_h 60 with 4 % of formamide (DCCA) on a $Pt/TiO_2/SiO_2/Si$ substrate

The BSO thin film showed a porous microstructure (Fig. 71 a) with an approximate thickness of 300 nm (Fig. 71 b) and an average roughness (R_a) of 270 nm (Fig. 71 c). The microstructure of the BSO thin film indicates that the film transforms to a gel before it dried. As a consequence a lot of solvent was trapped in the thin film during the evaporation and heat-treatment processes, and a high porosity resulted.

With increasing the amount of formamide from 4 to 6 % a significant improvement in the microstructural development of the BSO thin film (Fig. 72) was observed. A comparison between the FE-SEM micrographs (Fig. 71 and Fig. 72) of the BSO thin films clearly indicates that 6 % of formamide (DCCA) suppresses the polymerization during the thin film synthesis. Therefore, the BSO thin film dries before it gels and thus, forms a dense BSO thin film. However, cracks in thin film appeared. Cracking in the thin film (Fig. 72) can be attributed to the high vapour pressure of the acetic acid and an unevenly distributed pore size in the film, causing stress concentration of the pores to be great enough so that cracks develop. In addition, the acetic acid serves as a catalyser and the network structure is too stiff, so that generated stress cannot be released throughout the network. With a further dilution using formamide the viscosity of the sol increases, causing poor wetability of the substrates. Therefore, for the preparation of the BSO thin film from sols with R_h 60, with DCCA, the optimal amount of formamide was estimated to be 6 %.

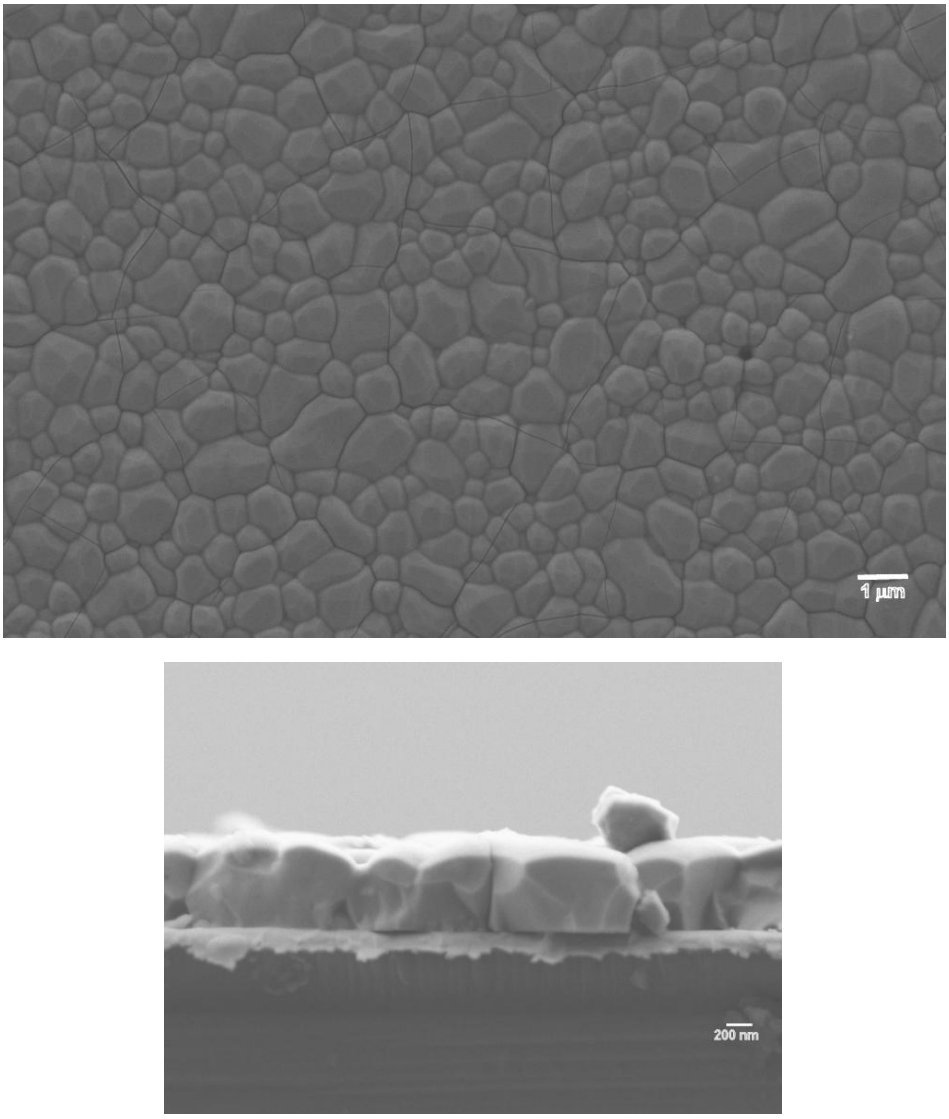

Figure 72: FE-SEM micrographs of the microstructures and cross-sections of BSO thin films prepared at 700°C for 1h, deposited from the sol R_h 60 with DCCA on a $Pt/TiO_2/SiO_2/Si$ substrate

The influence of the substrate on the microstructural development of BSO thin films deposited from sol R_h 60 with DCCA, was studied by FE-SEM. Fig. 72 - 74 shows FE-SEM micrographs of the microstructure and cross-section of the BSO thin film deposited on $Pt/TiO_2/SiO_2/Si$, sapphire and spinel substrate, annealed at 700°C for 1h.

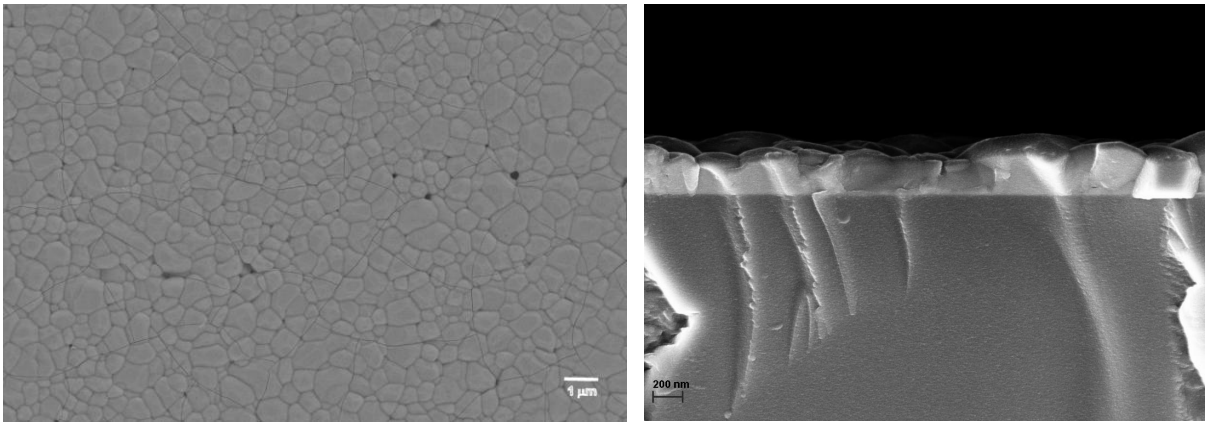

Figure 73: FE-SEM micrographs of the microstructures and cross-sections of BSO thin films prepared at 700°C for 1h, deposited from the sol R_h 60 with DCCA on a sapphire substrate

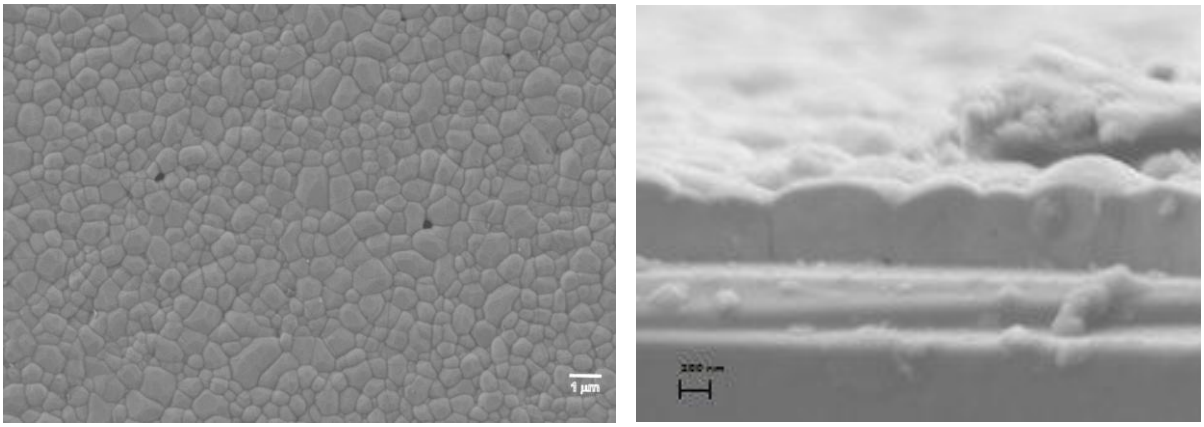

Figure 74: FE-SEM micrographs of the microstructures and cross-sections of BSO thin films prepared at 700°C for 1h, deposited from the sol R_h 60 with DCCA on a spinel substrate

No significant variation in the microstructural development of the deposited thin films on various substrates was observed. The BSO thin films deposited on $Pt/TiO_2/SiO_2/Si$, sapphire and spinel substrates show a rather dense bimodal microstructure with a grain size ranging from 200 nm to 1µm and an approximate thickness of 500 nm. It seems that the influence of the substrate on the microstructural development is reduced during pre-heating and annealing.

Atomic force microscopy was used to estimate the surface roughness of the BSO thin film deposited on various substrates. The Fig. 75 shows the micrographs of the BSO thin film deposited on the $Pt/TiO_2/SiO_2/Si$, sapphire and spinel substrates.

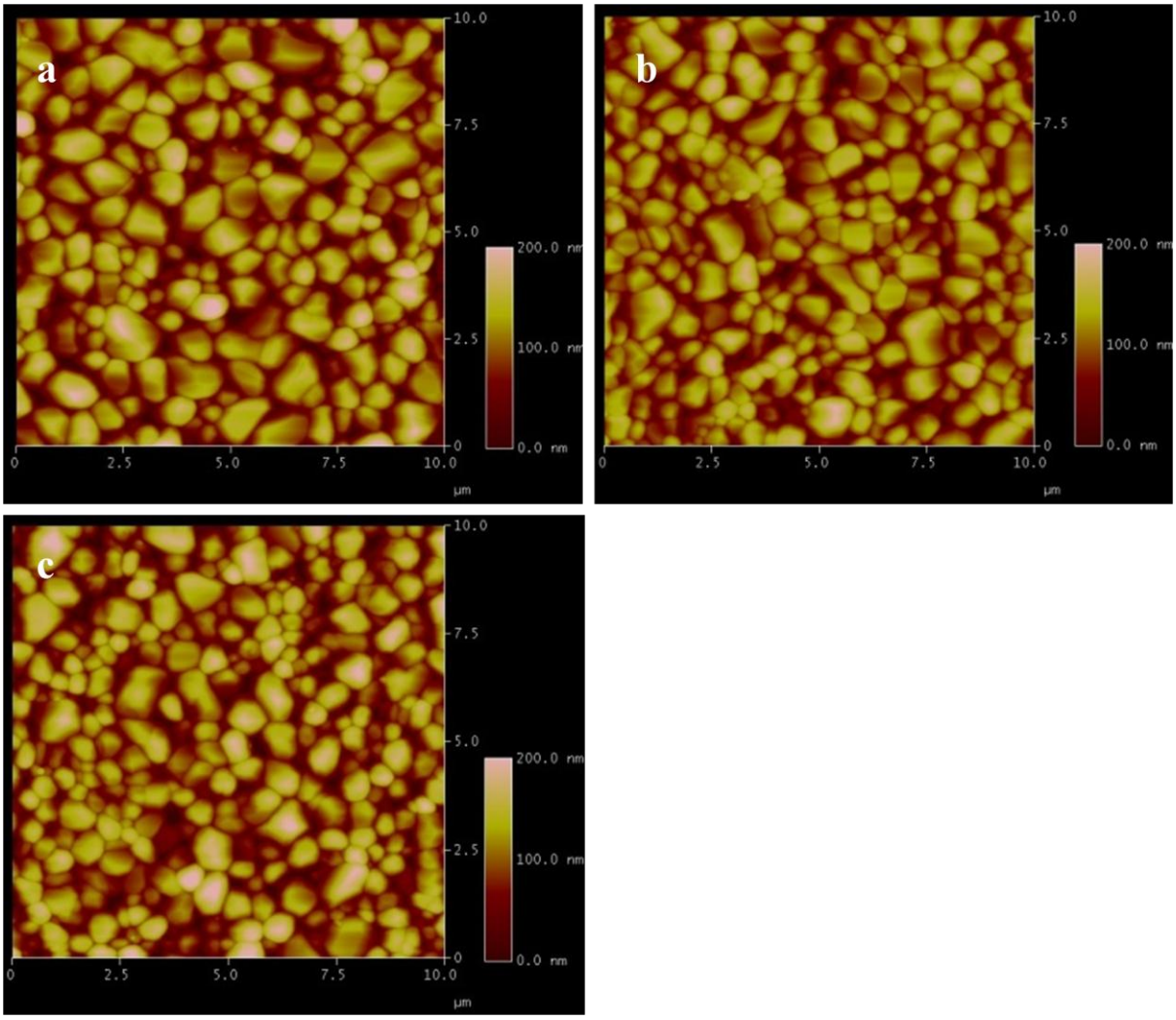

Figure 75: FE-SEM micrographs of the microstructures and cross-sections of BSO thin films prepared at 700°C for 1h, deposited from the sol R_h 60 with DCCA on a spinel substrate

Fig. 75 proves that the surface roughness does not vary with the substrate and the estimated average roughness (R_a) of the BSO thin films was 120 nm.

We believe that the influence of the substrate on the microstructural development of BSO thin films is reduced due to the good wettability of the sols during deposition. This good wettability of the sols resulted from the lower viscosity of the sol R_h 60 with DCCA. If the sol is homogeneously spread over the substrate, with further depositions and pre-heating treatment the influence of the substrate is reduced. Fig. 76 shows an SEM micrograph of 1-layer BSO thin film deposited on the $Pt/TiO_2/SiO_2/Si$ substrate. One can see that the sol is uniformly spread throughout the substrate, which causes a reduction of the influence of the substrate on the microstructural development of BSO thin films.

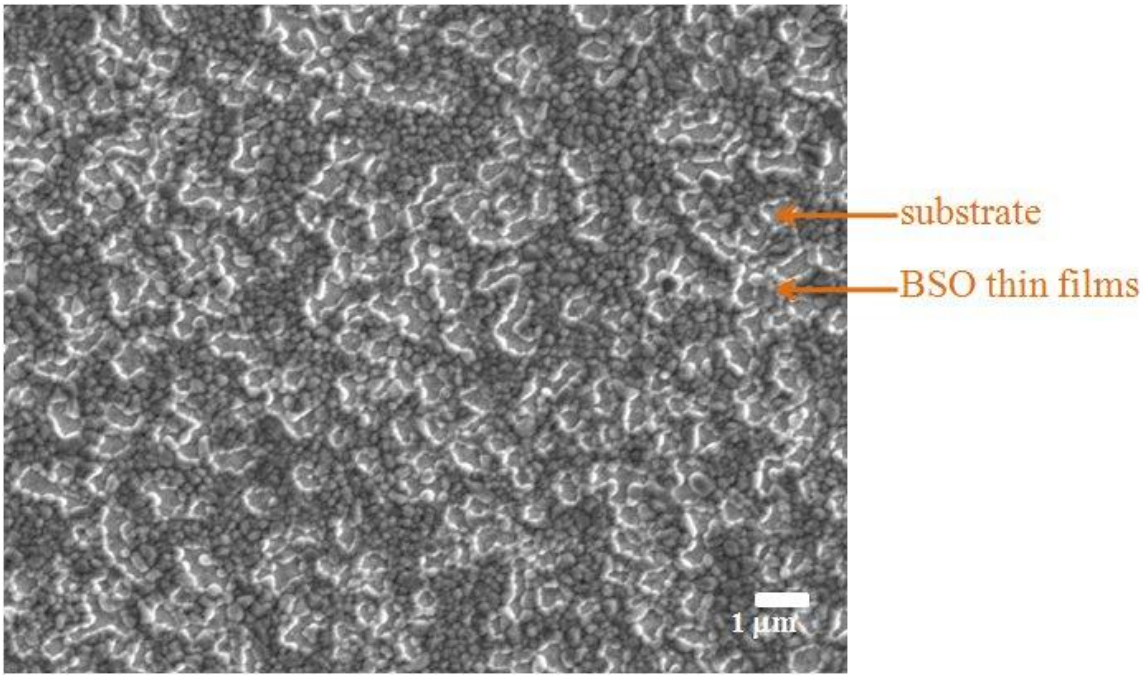

Figure 76: FE-SEM micrographs of the microstructure of 1-layer BSO thin films deposited from the sol R_h 60, with DCCA on a $Pt/TiO_2/SiO_2/Si$ substrate

4.3.3 Sol synthesis-2-EtO-EtOH

2-ethoxyethanol (2-EtO-EtOH) as solvent

In the sol-gel process the solvent directly affects the rate of the hydrolysis and condensation reaction, the solubility of the precursors and the time of the gelation [72-74]. In addition, the volatility of the solvent effects the porosity and the crack formation in the thin film synthesis. It is well known that acetic acid is not an inert solvent in an alkoxide solution [75-60]. It acts as a chemical modifying agent by reacting with alkoxide precursor or metal salt and serves as catalyser in the sol-gel process. In addition, acetic acid has a high vapour pressure, 1.58 kPa at 20°C, therefore, its tendency to evaporate from the thin film is high, which may result in porosity and crack formation in the BSO thin film. In contrast, the vapour pressure of 2-ethoxyethanol (0.5 kPa at 20°C) is lower than that of the acetic acid, therefore replacing the acetic acid with 2-ethoxyethanol in the precursor solution could reduce the rate of evaporation during the initial stages of drying, thus reducing the drying stress and preventing the cracking of the film. In addition, 2-ethoxyethanol in combination with the aprotic solvent could further retard the rate of hydrolysis and a condensation reaction.

The viscosity of the sol has a great influence on the microstructural development of thin films. Therefore, the viscosity behaviour of the sol R_h 60 with DCCA as a function of concentration was investigated. Fig. 77 shows the evolution of the viscosity with time and the sol concentration. The viscosity of the sol decreases with a decrease of the sol concentration down to 0.7 M. With a further dilution of sol R_h 60 with DCCA the precipitation of bismuth nitrate appeared. It is worth noting the similarity between the curves of the viscosity and stability for sols R_h 60 (Fig. 36 and Fig. 37) and sols R_h 60 with DCCA (Fig. 77 and Fig. 78). One can see that the precipitation appears below a concentration of 0.76 M in the sol R_h 60 with DCCA (Fig. 78) and also in sol R_h 60 (Fig. 37).

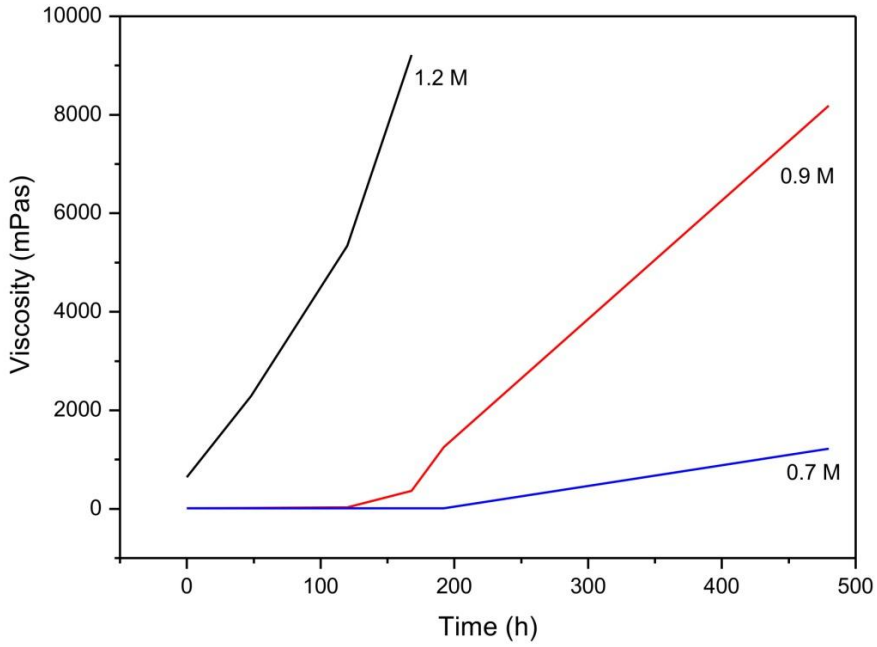

Figure 77: Dependence of the sol concentration on the viscosity of sol R_h 60 with DCCA

From Fig. 77 it is clear that the formamide does not have a significant influence on the viscosity or stability of the sols. On the other hand, there is slight difference in the time of gelation of the sols, which is shown in Fig. 78.

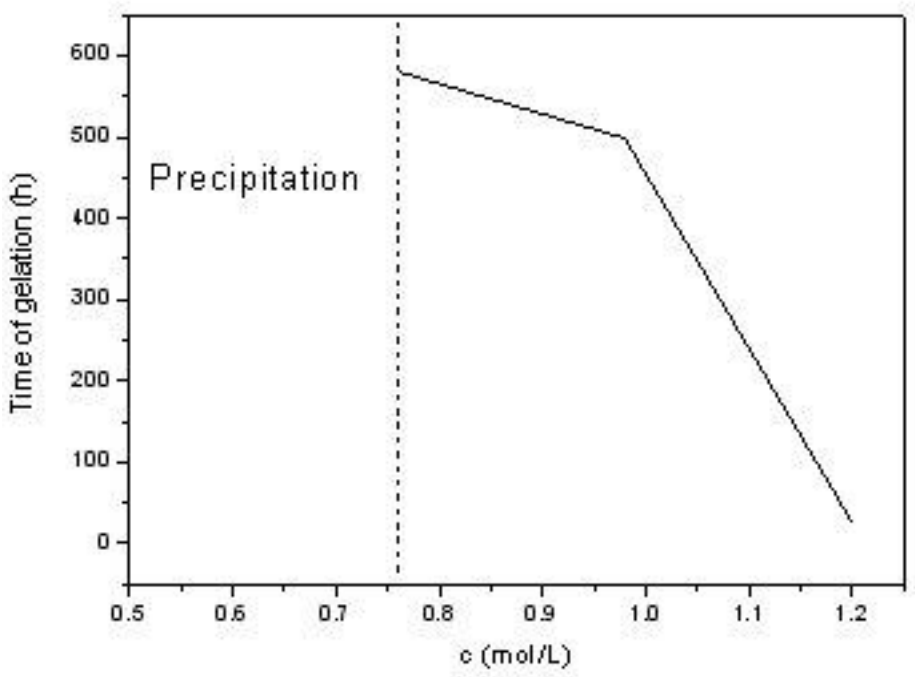

Figure 78: Dependence of the sol concentration on the gelation time of sol R_h 60 with DCCA

Fig. 78 shows the influence of the sol concentration on the time of gelation, where it can be seen that the time of gelation for the sol with a sol concentration of 1.2 M was 20 h, while the sol with a concentration of 0.76 M gelated in 560 h.

4.3.4 Thin-film deposition

Thin-film deposition and heat treatment represents the last step in the thin-film synthesis. Fig. 79 shows the FT-IR transmission spectrum for dried amorphous thin films deposited on Si substrates from the sols R_h 60 with DCCA.

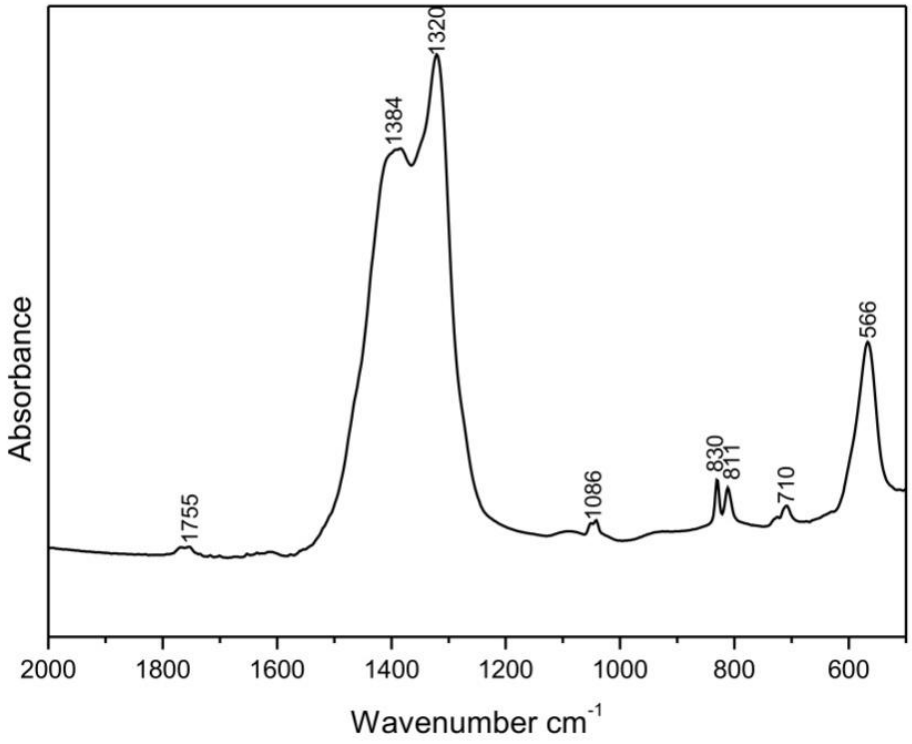

Figure 79: FT-IR transmission spectrum of thin film deposited from sol R_h 60 with DCCA

The absorption bands located at 1384, 1320, 830, 811 and 710 cm^{-1} were assigned to the vibrations of the N-O stretch [141]. The bend at 1755 cm^{-1} is attributed to the stretching vibration of acetic acid, which is still present in the thin film [87]. The band at 1086 cm^{-1} was related to the asymmetric stretch of the Si-O-Si bond [141]. The band located at 566 cm^{-1} was assigned to the vibration of the Bi-O bond [142]. This FT-IR transmission result indicates that in the thin films deposited from the sol R_h 60 with DCCA the bismuth ions are coordinated by nitrate ligands. Similar ATR FT-IR results were observed for sols with R_h 60 (Fig. 39), where the bismuth ion is also coordinated by nitrate ligands.

In a sol-gel process, before the thin film was subjected to high-temperature annealing, the BSO thin film would predominantly contain a network of Bi, Si and O atoms in amorphous form. The TEM analysis of the dried thin film, shown in Fig. 80, indicates the formation of 10 nm size particles in an amorphous matrix. Its electron diffraction pattern (Fig. 80 c) reveals the same crystalline phase δ-Bi_2O_3 as in dried thin films deposited from sol R_h 60 (Fig. 40).

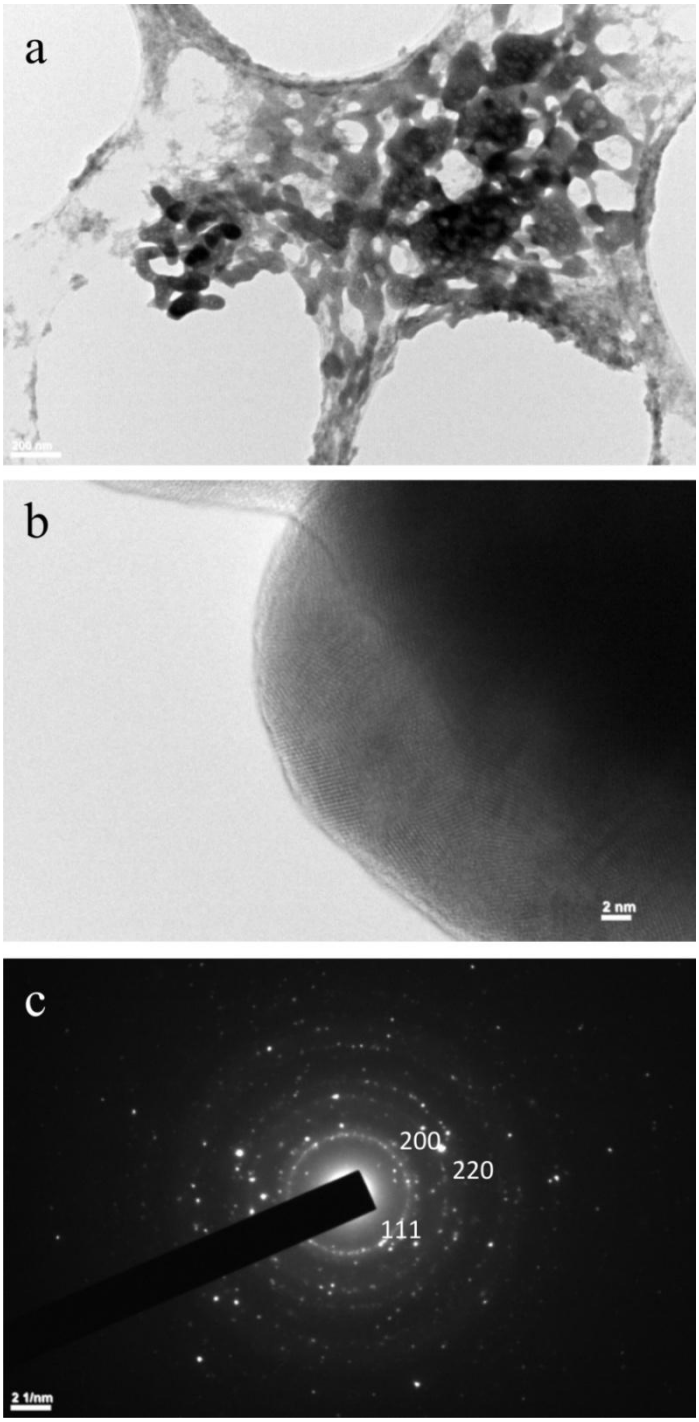

Figure 80: TEM analysis of a) and b) dried thin film deposited from sol R_h 60, with DCCA and c) electron diffraction pattern of the crystalline particle (Fig. 80 b)

In order to determine the pre-heating temperature of the BSO thin film deposited from sol R_h 60 with DCCA the thermoanalysis was done on xerogels (Fig. 81) and thin films (Fig. 82). In the case of the xerogel sample (Fig. 81) mass losses of 38 % were observed upon heating to 550°C. The thermal decomposition occurs stepwise: the mass loss from room temperature to 185 °C is 3.5 %, from 185 to 270°C, 19 %, from 270 to 330°C, 7.5 %, from 330 to 445°C, 2.5 % and upon further heating to 550°C, 5.5 %. The thermal effects recorded by DTA include a endothermic effect at 95°C, and a succession of exothermic peaks between 170°C and 500°C, with the strongest peaks at 245°C and 295°C. We followed the mass peaks of water (m/e^+ = 18), carbon dioxide (m/e^+ = 44) and nitrogen dioxide (m/e^+ = 46). Between room temperature and 170°C, the first step of mass loss, evaporation of water and residual solvent occurs as

confirmed by a broad endothermic peak. In further steps of mass loss between 170 and 330°C the evolution of water and carbon dioxide confirm the oxidation of organic groups in air. In addition, nitrogen dioxide evolution also occurs. The final step of the decomposition, between 330 and 550°C, is mainly a consequence of nitrogen dioxide evolution as a result of the decomposition of nitrate groups.

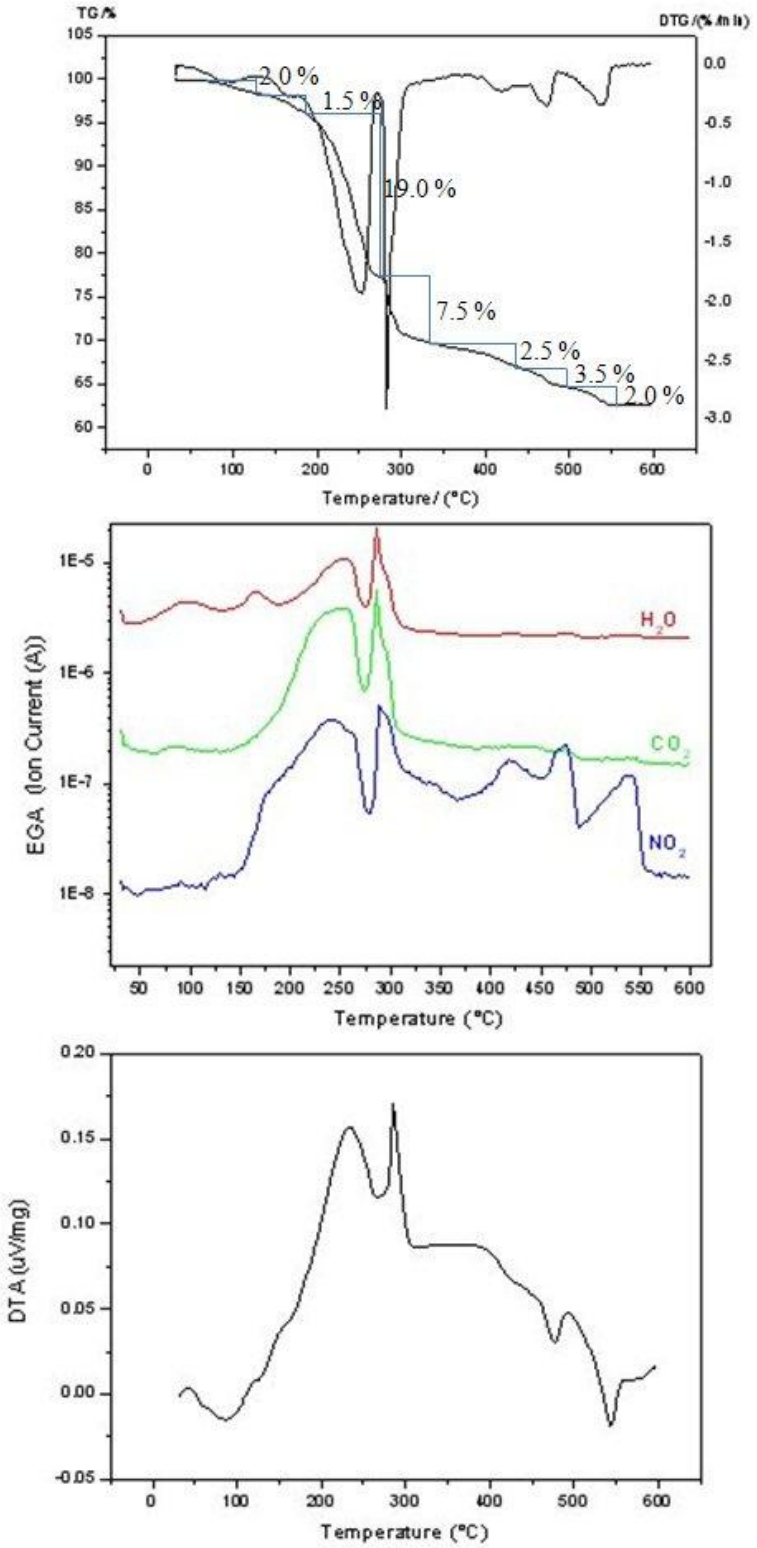

Figure 81: TG/DTG/EGA/DTA curves of xerogel of sol R_h 60 with DCCA

The thermoanalysis, TG and DSC curves, of the as-dried thin film are shown in Fig. 82.

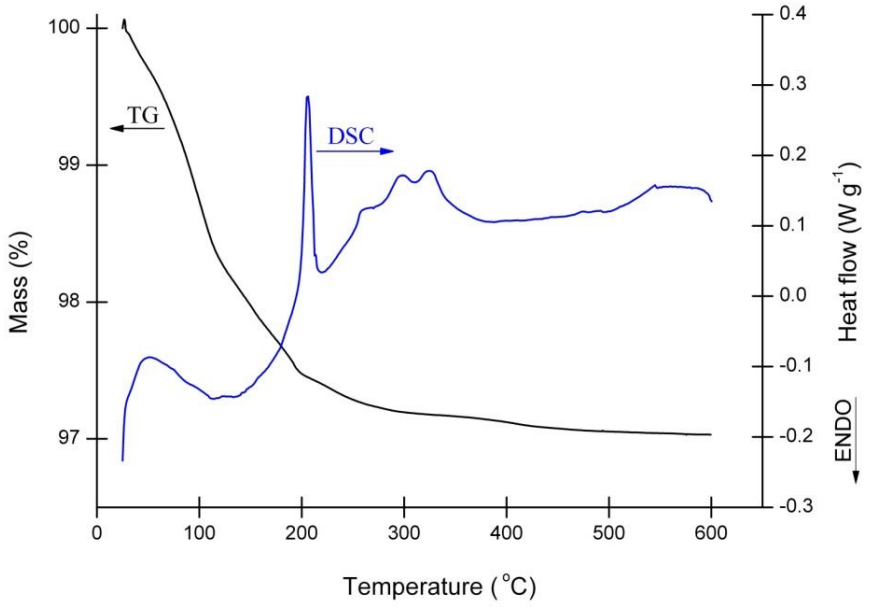

Figure 82: TG/DSC curves of thin film deposited from sol R_h 60, using DCCA

The weight loss in the TG curve (Fig. 82) corresponds to the evaporation of the solvent, residual organic and nitrate compounds. In the TG curve the same tendency of weight loss during heat treatment as in thin film deposited from sol R_h 60 with DCCA was observed (Fig. 69), where acetic acid was used as the solvent. Therefore, a preheating temperature of 250°C was used for the preparation of the BSO thin films from sol R_h 60 with DCCA.

As already mentioned, annealing temperatures have a significant influence on the phase evolution of the thin films. In order to follow the phase formation of the BSO phase we analyzed the X-ray diffraction pattern of a thin film deposited on a $Pt/TiO_2/SiO_2/Si$ substrate and annealed at temperatures ranging from 300°C to 700°C. The results of the X-ray analysis are shown in Fig. 83.

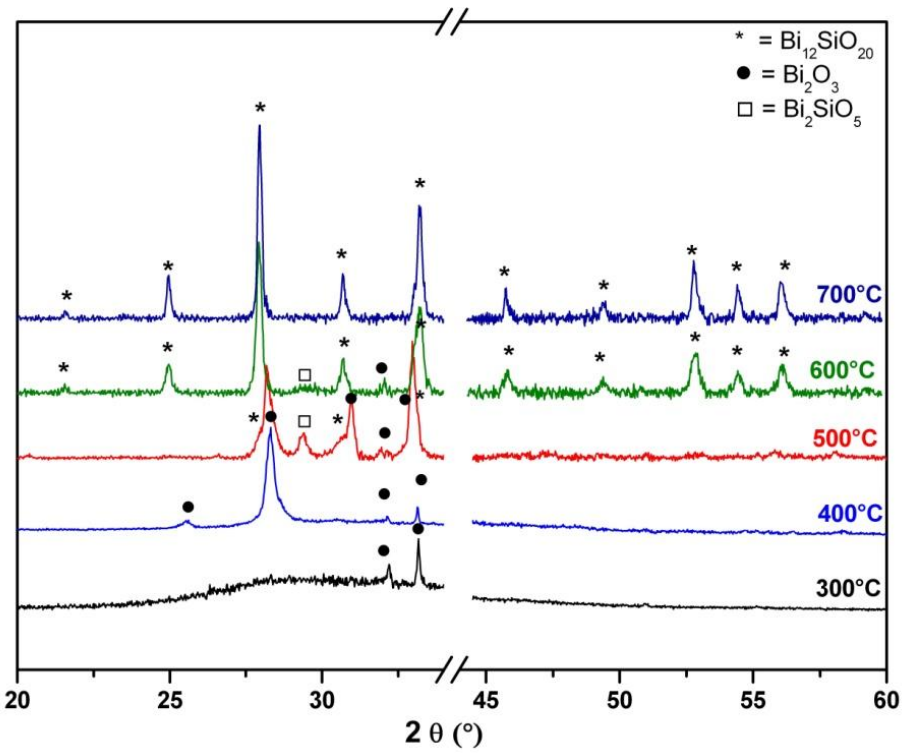

Figure 83: XRD patterns of the thin film deposited on a $Pt/TiO_2/SiO_2/Si$ substrate and annealed from 300°C to 700°C

At 300°C and 400°C we observed the presence of the bismuth oxide phase. After heating at 500°C, the formation of new phases $Bi_{12}SiO_{20}$ (BSO) and Bi_2SiO_5 was confirmed. At 600°C the majority of the reflections belongs to the sillenite BSO phase; however, there are still traces of the bismuth oxide and Bi_2SiO_5 phases present. When the annealing temperature was increased to 700°C the only detected phase was BSO. Under these annealing conditions no evaporation or sublimation of Bi_2O_3 from the thin films was observed, as only the pure BSO phase formed and no secondary Bi-deficient phases were detected. The same phase evolution was observed for the sapphire and spinel substrates.

The microstructural development of the BSO thin films which were pre-heated at 250°C and annealed at 700°C for 1 h were studied with FE-SEM. Fig. 84 shows the FE-SEM micrographs of the microstructure and the cross-section of a BSO thin film deposited on a $Pt/TiO_2/SiO_2/Si$ substrate. The BSO thin film resulted in a dense and homogeneous microstructure with a thickness of 250 nm.

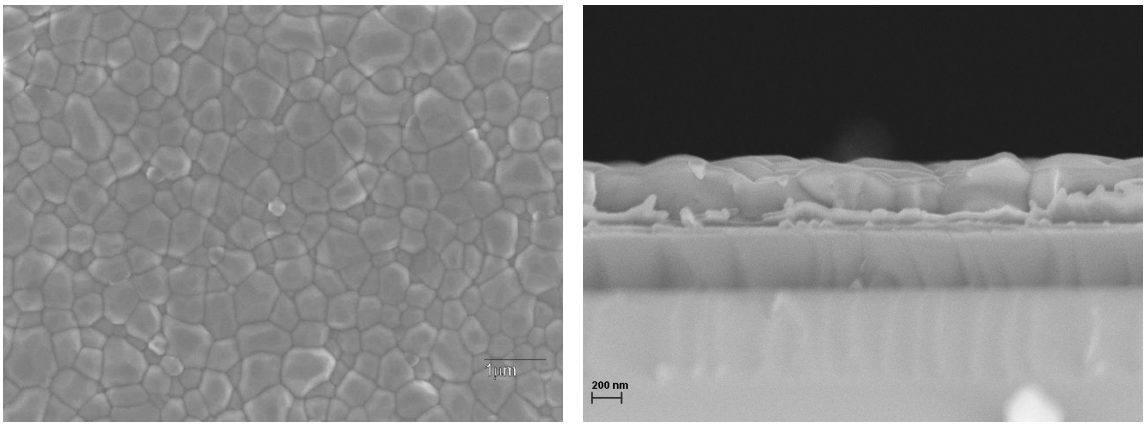

Figure 84: FE-SEM micrographs of the microstructures and cross-sections of BSO thin films prepared at 700°C for 1h, deposited from the sol R_h 60 with DCCA on a $Pt/TiO_2/SiO_2/Si$ substrate

A comparison of the microstructure of thin film deposited from sol R_h 60 with DCCA and the microstructure of the thin film deposited from sol R_h 60 without DCCA (Fig. 47) reveals large differences in the density of BSO thin films, indicating that formamide has a pronounced effect on the microstructural development. According to a report made by N. Viart et al.[143], on the structural evolution of a silica-sol containing formamide, relative to that of a sol without formamide, studied by FT-IR spectroscopy, they observed that in the formamide-containing sol a two-step structural evolution occurs. The condensation first preferentially leads to small oligomers of less than six atoms and these oligomers then condense together, resulting in a highly interconnected structure. While for the sol without formamide they observed that the structure is poorly interconnected, which leads to a non-uniform pore size distribution and a porous microstructure [147]. This observation is in accordance with our results for BSO thin films deposited from sol R_h 60 without DCCA, shown in Fig. 47. Regarding the report [147] and the results of our study one can conclude that in BSO thin films deposited from sol R_h 60 with DCCA (formamide) a two-step structural evolution occurs resulting in a highly interconnected structure and an even pore size distribution, which results in dense BSO thin films.

The AFM measurement of BSO thin film roughness (Fig. 85) deposited from sol R_h 60 with DCCA and annealed at 700°C, show that thin films have an average roughness (R_a) of 40 nm.

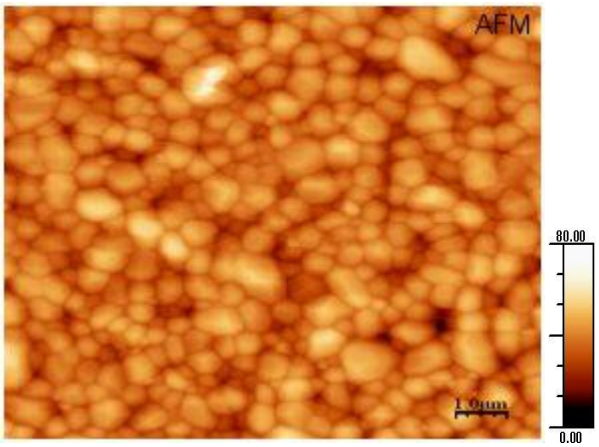

Figure 85: AFM micrographs of BSO thin films annealed at 700°C and deposited on $Pt/TiO_2/SiO_2/Si$

The microstructural analysis of the BSO thin film deposited from sol R_h 60 with DCCA on a sapphire substrate and annealed at 700°C for 1h (Fig. 86) revealed that the obtained thin film resulted in a dense and homogeneous microstructure with a thickness of 250 nm and an average roughness (R_a) of 50 nm.

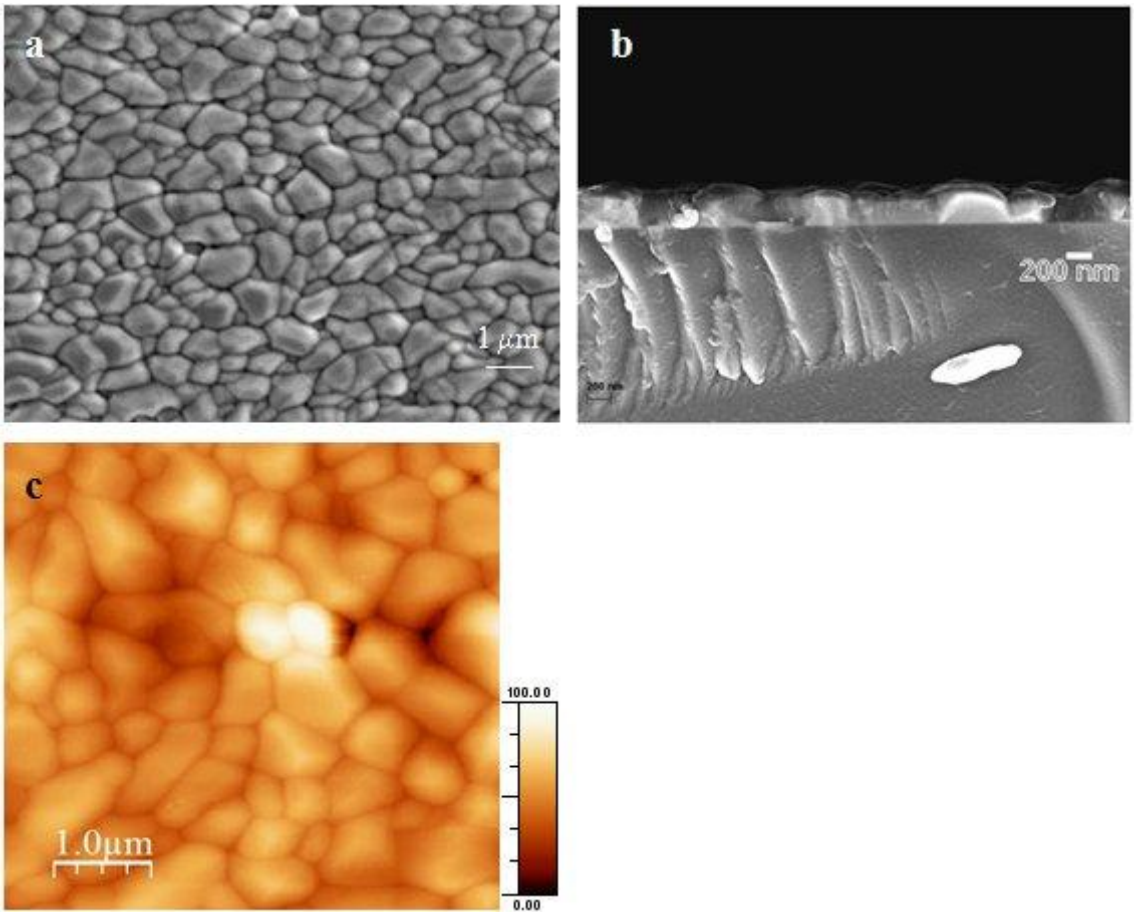

Figure 86: FE-SEM micrographs of the a) microstructure, b) cross-section and c) AFM of BSO thin film deposited on a sapphire substrate

From a comparison of the microstructural development of a BSO thin film on $Pt/TiO_2/SiO_2/Si$ (Fig. 84) and the sapphire substrate (Fig. 86) one can see that the substrate shows no significant influence on the quality of the thin film.

Fig. 87 shows a SEM micrograph of a 1-layer BSO thin film deposited on a $Pt/TiO_2/SiO_2/Si$ substrate. One can see that the sol is uniformly spread throughout the substrate, therefore the influence of the substrate with further deposition and heat treatment is reduced.

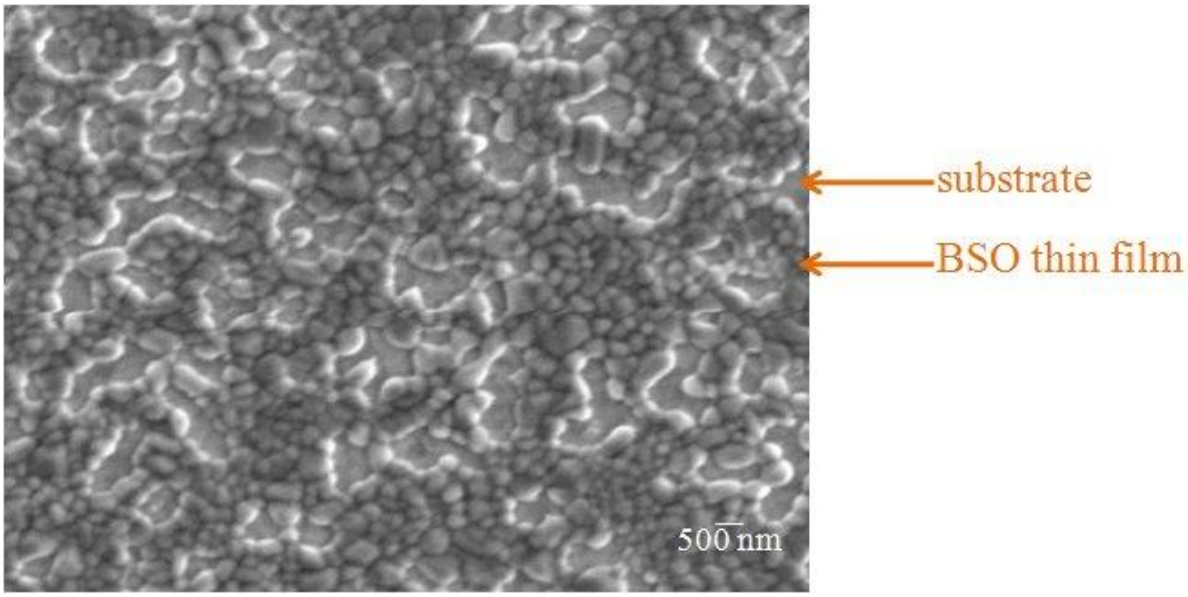

Figure 87: FE-SEM micrographs of the microstructure of 1-layer BSO thin films deposited from the sol R_h 60 with DCCA on a $Pt/TiO_2/SiO_2/Si$ substrate

4.4 Dielectric properties of BSO thin film

After optimization of the synthesis procedure to prepare dense, crack-free BSO thin films, the measurement of the dielectric properties was carried out. At present there is no commercially available equipment capable of measuring directly the relative dielectric constant and the dielectric losses of dielectric thin films at microwave frequencies. The usual method of examining the microwave properties of dielectric thin films is by sputtering a simple device such as a capacitor, measuring its response at microwave frequencies and evaluating its properties using a suitable device model [148].

There are two types of capacitors: parallel-plate capacitors (Fig. 88 a)), where the dielectric layer is sandwiched between the electrodes; and the planar capacitors (Fig. 88 b)), where the electrodes are patterned on the same side of the dielectric layer and are separated by a small gap. The parallel plate capacitor usually exhibits high capacitance, which increases enormously the uncertainty of the measurement at microwave frequencies, therefore, it is not suitable for the measurement of dielectric properties in the microwave region [148]. Therefore, only planar capacitor structure will be considered for the measurement of the microwave dielectric properties.

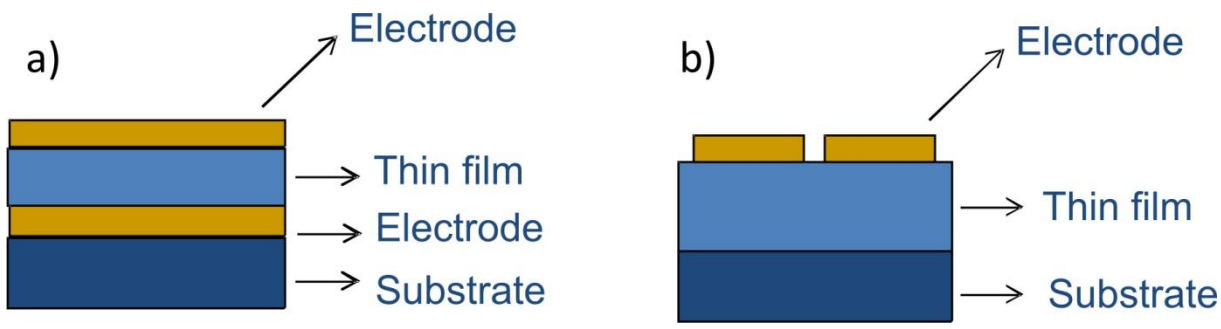

Figure 88: The structure of a) planar capacitor and b) parallel-plate capacitor

Fig. 89 shows the microwave dielectric properties of a BSO thin film as a function of the frequency measured at room temperature. It can be seen that the dielectric properties of BSO thin film are not frequency dependent. The dielectric loss of BSO thin films at 2 GHz was $2 \cdot 10^{-1}$, while the permittivity was 40. The large dielectric loss of the thin film indicated that the measuring configuration is not the most suitable for evaluating the dielectric properties of BSO-thin films.

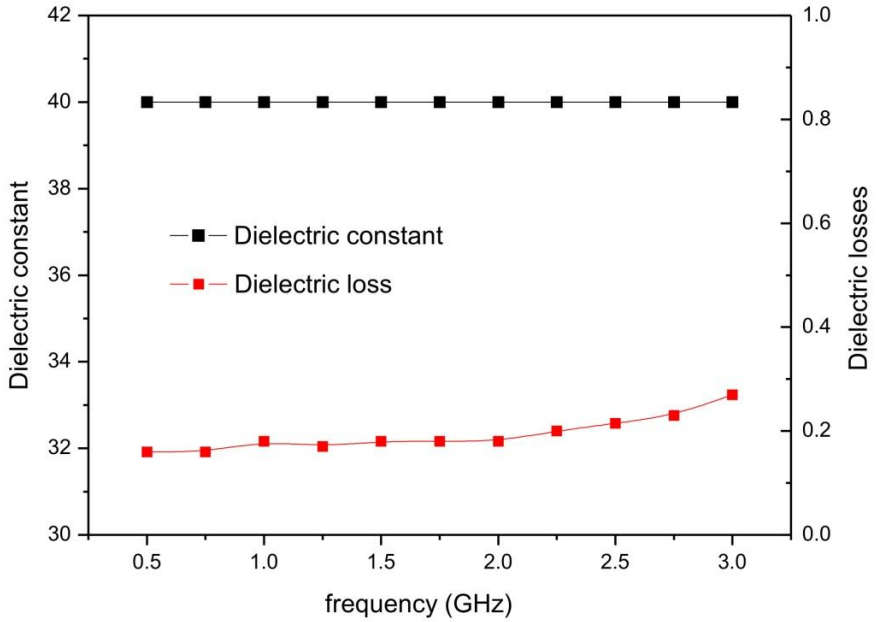

Figure 89: Microwave dielectric constant and dielectric loss for BSO thin as a function of frequency

The problem of evaluating the microwave properties of a BSO thin film by sputtering the planar capacitors is the limitation of the measurement ($\varepsilon_F / \varepsilon_D \geq 100$, $h_F \leq s \leq 10\ h_F$, $s \leq 0.25\ l$, $s \leq 0.5\ h_D$, where h_F is the dielectric thin film, h_D is the substrate thickness, s is the gap width, l is the electrode length, ε_D is the permittivity of the substrate and ε_F is the permittivity of the thin film[148]). The ε for the BSO bulk material is 37 and the ε for the spinel substrate is 8. Therefore, the ratio $\varepsilon_F / \varepsilon_D = 4.6$ is much lower than 100. Due to the small ratio between the dielectric constant of BSO thin film and the corundum substrate the uncertainty of the measurement increases.

The problem of evaluating the dielectric properties of a BSO thin film at microwave frequencies by synthesizing the planar capacitor can be overcome by using the split-dielectric-resonator method.

Krupka et al. proposed a split-dielectric-resonator method for the measurement of the dielectric properties of the dielectric sheet samples [149].

The dielectric properties of the BSO thin films deposited from sol R_h 60 with DCCA and 2-ethoxyethanol were measured at 10 GHz. The obtained permittivity and the dielectric loss were 40 and $17 \cdot 10^{-3}$, respectively.

For the measurement of the dielectric properties of the BSO thin films in the lower-frequency range (100 kHz-1MHz) parallel-plate capacitors was used. The parallel-plate capacitor was synthesized by using a $Pt/TiO_2/SiO_2/Si$ substrate, were Pt represents the bottom electrode, whereas for the upper electrode Au was used. A limitation in parallel-plate capacitors is the roughness of the BSO thin films. A low surface roughness promotes better contact properties between the electrode and the thin film and reduces the insertion losses.

The dielectric properties at lower frequencies (100 kHz-1MHz) measured by the synthesis of parallel-plate capacitors, are shown in Fig. 90.

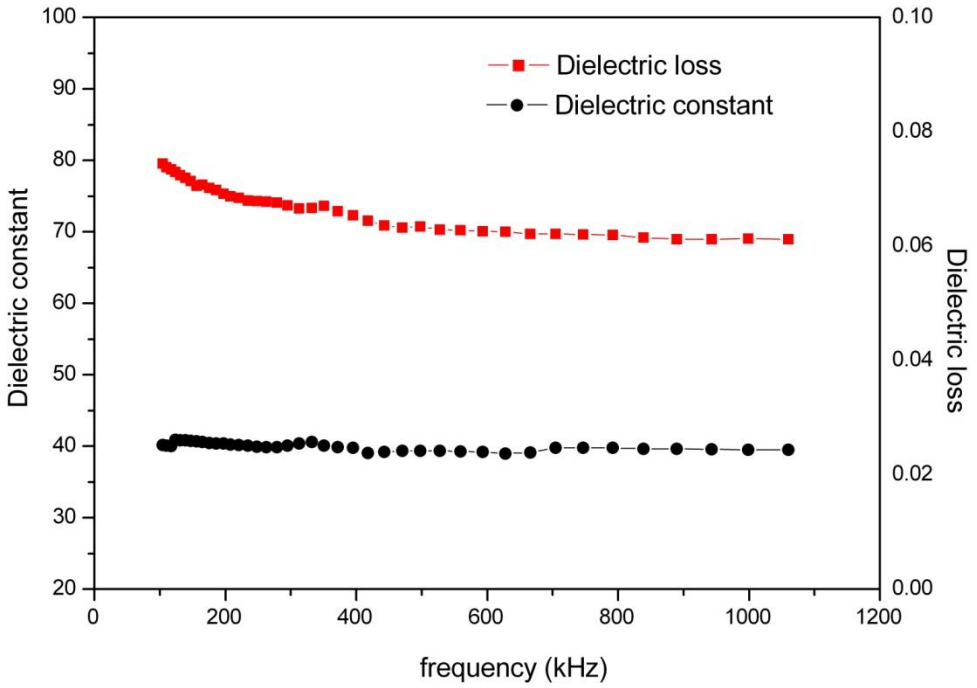

Figure 90: Dielectric constant and dielectric loss for BSO thin as a function of frequency

It is clear that the dielectric properties of the BSO thin film are not frequency dependent. The dielectric loss of the BSO thin films at 1MHz was $6 \cdot 10^{-2}$, while the permittivity was 40. The large dielectric loss in the thin film was attributed to the effect of the interfacial dead layer, possibly existing at the film/electrode interface. The large surface roughness of the BSO thin film (40 nm) can increase the dielectric losses of the BSO thin film by forming a dead layer between the electrode and the thin film.

5. Conclusion

The intention of this thesis was to systematically investigate the synthesis parameters for the preparation of dense BSO thin films, determine the dielectric properties of the BSO thin films and to consider the possibility of using BSO thin films in modern electronic systems.
The BSO thin films were prepared from three different molar ratios (R_h):

1. Synthesis of sol R_h 60
2. Synthesis of sol R_h 5
3. Synthesis of sol R_h 60 with DCCA

The deposited BSO thin films were pre-heated at 250°C and annealed at 700°C.

Synthesis of sol R_h 60

In the synthesis procedure of sol R_h 60 we observed the formation of precipitates below 0.76 M of sol concentration. A sol with a concentration of 1.2 M gelates in 5 h, while a sol with a concentration of 0.76 M becomes a gel in 470 h. Moreover, the sol-gel structure was poorly interconnected, which led to a non-uniform pore-size distribution. This resulted in the development of a porous microstructure. In addition, an excessive hydrolysis and condensation reaction also contributed to the formation of a porous microstructure of BSO thin films. In this synthesis procedure there was no visible influence of the substrate on the microstructural development of the BSO thin film.

Synthesis of sol R_h 5

The amount of water in the sol, the R_h value, was decreased to control the rate of hydrolysis and the condensation reaction. In the synthesis procedure of sol R_h 5, a stable sol was formed by adding ethanolamine to the solution. Ethanolamine as a complexing agent induced two major effects, the steric hindrance and inductive effects, which reduced the reaction of the water with the bismuth precursor and ensured the stability of the sol with aging time. In addition, the ethanolamine also reduced the catalytic effect of the acetic acid. The gelation time for the sol R_h 5 with a concentration of 1.1 M was 220 h, while the sol R_h 5 with a concentration of 0.48 M becomes a gel in 723 h. We observed that the substrate had a large influence on the microstructural development. The investigation of the influence of different substrates on the microstructural development revealed that $Pt/TiO_2/SiO_2/Si$ as a substrate led to the formation of a homogeneous and dense BSO thin film of thickness ≅ 200nm. The thin film deposited on the spinel substrate also showed a homogeneous microstructure with a thickness of 300 nm, while the BSO thin film deposited on the sapphire substrate resulted in a porous thin-film formation with a rough surface and a thickness of 400 nm. The roughness measured by AFM ranged from 50 to 60 nm for the $Pt/TiO_2/SiO_2/Si$ substrate and 20 to 30 nm for the spinel substrate, while the roughness of the BSO thin film deposited on the sapphire substrate was as high as 100 to 120 nm.
The disadvantage of using ethanolamine as a stabilizing agent was in its high viscosity, which consequently caused an increase in the viscosity of the sol and with this the poor wetability of the substrate was observed. In addition, the $Bi(NO_3)_3 \cdot 5H_2O$ must be vacuum dried for 96 h to reduce the amount of water. After dissolving the dried $Bi(NO_3)_3$ in acetic acid, and before the ethanolamine is added, bismuth showed a very strong tendency to re-crystallize.

Synthesis of sol R_h 60 with DCCA

In order to avoid the disadvantages of using ethanolamine in sol synthesis another synthesis procedure was adapted. To control the rate of the hydrolysis and condensation reactions and the drying behaviour of the gel network, formamide (DCCA) was added to the sol. In sols R_h 60 with DCCA, we have studied the influence of different solvents (acetic acid, 2-ethoxyethanol) on the stability of sols and on the microstructural development of the $Bi_{12}SiO_{20}$ thin films.
We observed that the solvent had a significant influence on the stability of the sols and the quality of the BSO thin films. By comparing the reaction mechanism of the sols using 2-ethoxyethanol or acetic acid we were able to conclude that the hydrolysis and condensation reactions are more pronounced in the sol using acetic acid as a solvent, which results in a shorter gelation time (c = 0.76 M, t_G = 84 h) compared to the sol using 2-ethoxyethanol as the solvent (c = 0.76 M, t_G = 580 h). When the acetic acid was used as the solvent, the coordination sphere of the bismuth in the sols changed. In such sols the bismuth is bidentately coordinated with the carboxylate ligand, which allowed the formation of stable sols. When 2-ethoxyethanol was used as the solvent, precipitates formed below the 0.76-M sol concentration, due to the bismuth coordination with the nitrate ligands. The deposition of the BSO thin films on $Si/SiO_2/TiO_2/Pt$ from the sol using 2-ethoxyethanol as a solvent resulted in a homogeneous and dense microstructure with a thickness of 250 nm, while the BSO thin films deposited from the sol using acetic acid as a solvent resulted in a rather dense microstructure with a crack formation and an approximate thickness of 300 nm. We observed that the surface roughness of the BSO thin films deposited from the sol using acetic acid, does not vary with the substrate and it is estimated to be 120 nm, while the BSO thin films deposited from the sol using 2-ethoxyethanol exhibit 30 nm roughnesses. In this synthesis procedure the substrate has no influence on the microstructural development.

The dielectric properties were studied on a thin film deposited from the sol R_h 60 with DCCA and 2-ethoxyethanol, which exhibited a dense and crack-free microstructure. For the measurement of the dielectric properties of the BSO thin films in the lower-frequency region (100 kHz-1MHz) parallel-plate capacitors was used. We observed that the dielectric properties of the BSO thin film are not frequency depended. The d dielectric loss of the BSO thin films at 1MHz was $6\ 10^{-2}$, while the dielectric constant was 40. For the measurement of the dielectric properties in the microwave region (0.5 - 3 GHz) the planar-plate capacitor was used. The dielectric constant and the dielectric loss at 2 GHz were 40 and $2\ 10^{-1}$, respectively, while the dielectric constant and the dielectric losses, measured with split-dielectric-resonator at 10 GHz, were 40 and $1.7\ 10^{-2}$, respectively. The most suitable measurement configuration for the evaluation of the dielectric properties of BSO thin films was found to be split-dielectric-resonator method.

The obtained results suggest that such materials are attractive for microwave applications.

6. Acknowledgements

Looking back, I am surprised and at the same time very grateful for all I have received throughout these years. It has certainly shaped me as a person and has led me to where I am now.

First, I would like to thank my supervisor, Prof. Dr. Danilo Suvorov, for giving me an opportunity to conclude my education with a doctoral degree, for his guidance in my work and for his constant support and encouragement.

Thanks to Dr. Špela Kunej not only for the uncountable number of useful discussions, but also for her friendship.

Thanks to Asst. Prof. Boštjan Jančar for the TEM analysis and helpful discussions that produced numerous ideas.

Thanks to Prof. Dr. Boris Orel for FT-IR analysis and for valuable discussions about my work.

Finally, I would like to thank my family for giving me an opportunity to study and for their support of my decision.

Last, but not least, very special thanks to my husband, Damijan, for his encouragement, support and patience.

7. References

1. Chen, Y. C.; Wang, C. W.; Chen, K. H.; Huang, Y. D.; Chen, Y. C. Microwave Dielectric Properties of $0.93(Mg_{0.95}Co_{0.05})TiO_3$–$0.07CaTiO_3$ for Application in Patch Antenna. *Japanese Journal of Applied Physics* **47**, 992 (2008).
2. Chen, Y.; Zeng, Y. W. Double-layered coplanar patch antenna on $CaLa_4Ti_5O_{17}$ high-permittivity substrate with coplanar waveguide feed line. *Microwave and Optical Technology Letters* **51,** 98 (2009).
3. Schuisky, M.; Hlrsta, A. Epitaxial growth of $Bi_2O_{2.33}$ by halide CVD. *Chemical Vapor Deposition* **2**, 235 (1996).
4. Mehring, M. From molecules to bismuth oxide-based materials: Potential homo- and heterometallic precursors and model compounds. *Coordination Chemistry Reviews* **25**, 974 (2007).
5. Levin, E. M.; Roth, R. S. Polymorphism of bismuth sesquioxide. I. Pure Bi_2O_3. *Journal of Research of the National Bureau of Standards: A Physics and Chemistry* **68 A,** 189 (1964).
6. Miyayama, M. Yanagida, H. J. Oxygen ion conduction in γ-Bi_2O_3 doped with Sb_2O_3. *Journal of Material Science* **21**, 1233 (1986)
7. Levin, E. M.; Roth, R. S. Polymorphism of bismuth sesquioxide, II. Effects of oxide additions of type polymorphism of Bi_2O_3. *Journal of Research of the National Bureau of Standards: A Physics and Chemistry* **68 A,** 197 (1964).
8. Sillen, L.G. X-ray Studies of Bismuth Trioxide. *Ark. Kemi. Mineral. Geol.* **12A**, 1 (1937).
9. Valant, M.; Suvorov, D. A Stoichiometric Model for Sillenites. *Chemistry of Materials* **14,** 3471 (2002).
10. Valant, M.; Meden A.; Suvorov D. Isomorphic A-Site Substitution on Sillenite-Type Compound. *Journal of American Ceramic Society* **87**, 677 (2004).
11. Radaev, S. F.; Simonov, V. I. Structures of Sillenites and Atomic Mechanisms of their isomorphic substitutions. *Soviet Physics-Crystallography (Engl. Transl.)* **37**, 484 (1992).
12. Murray, A. D.; Catlow, C. R. A.; Beech, F.; Drennan, J. A Neutron Powder Diffraction Study of the Low- and High-Temperature structure of $Bi_{12}PbO_{20}$. *Journal of Solid State Chemistry* **62,** 290 (1986).
13. Ballman, A. A.; Brown, H.; Tien, P. K.; Martin, J. The growth of the single crystalline waveguiding thin films of piezoelectric Sillenites. *Journal of Crystal Growth* **20,** 251 (1973).
14. Alfonso, J. E.; Martin, M. J.; Volkov, V.; Zaldo, C.; Aguilo, M., Da Silva, M. F.; Saores, J. C. Photoconductive $Bi_{12}MO_{20}$-type films prepared by pulsed laser deposition. *Journal of Material Research* **14**, 4409 (1999).
15. Tada, K.; Kuhara, Y.; Tatsumi, M.; Yamaguchi, T. Liquid-phase epitaxial growth of bismuth silicon oxide single-crystal film: a new optically activated optical switch. *Applied Optics* **21,** 2953 (1982).
16. Attard, A. E. Theory of origins of photorefractive and photoconductive effects in γ-$Bi_{12}SiO_{20}$. *Journal of Applied Physics* **69,** 44 (1991).

17. Bruton, T. M.; Briece, J. C.; Hill, O. F.; Whiffin, P. A. C. The flux growth of some γ-Bi_2O_3 crystals by the top seeded technique. *Journal of Crystal Growth* **23,** 21 (1974).
18. Toyoda, T.; Nakanishi, H.; Endo, S.; Irie, T. Hydrostatic pressure dependence of the optical absorption edge in $Bi_{12}SiO_{20}$. *Journal of Applied Physics* **61,** 2065 (1987).
19. Hennesey, P.; Vedam, K. Piezo- and thermo-optical properties of $Bi_{12}SiO_{20}$. *Journal of the Optical Society of America* **89**, 352 (1979).
20. Panchenko, T. V. Photo- and thermally induced optical absorption and photoconductivity of Sillen crystals. *Physics of the Solid State* **42,** 657 (2000).
21. Seery, D. A.; Garret, M. H.; Tanguay, A. R. Electro-optic measurement of the volume resistivity of bismuth silicon oxide ($Bi_{12}SiO_{20}$). *Journal of Crystal Growth* **85**, 282 (1987).
22. Lenzo, P. V.; Spencer, E. G.; Ballman, A. A. Optical activity and electro-optic effect in bismuth germanium oxide ($Bi_{12}GeO_{20}$). *Applied Optics* **5,** 1688 (1966).
23. Henry, M.; Mallick, S.; Rouede, D. Propagation of light in an optically active electro-optic crystal of $Bi_{12}SiO_{20}$. *Journal of Applied Physics* **59,** 2650 (1986).
24. Mallick, S.; Rouede, D. Effiency and polarization characteristics of photorefractive diffraction in $Bi_{12}SiO_{20}$. *Journal of the Optical Society of America B* **4,** 1247 (1987).
25. Nomura, K.; Ogawa, H. Electro-optic effects of electron cyclotron resonance plasma-sputtered thin films on sapphire. *Journal of Applied Physics* **70**, 3234 (1991).
26. Tassev, V.; Diankov, G.; Gospodinov, M. Optical activity of doped sillenite crystals. *Material Research Bulletin* **30**, 1263 (1995).
27. Lin, C.; Fan, T.; Zhang, Y.; Niu, S.; Gou, C.; Shi, Z. A study of acoustical activity in $Bi_{12}GeO_{20}$. *Solid State Communications* **54,** 803 (1985).
28. Marquet, H.; Gies, J-G.; Merle, J. C. The role of some shallow trap centers in the photochromism of $Bi_{12}GeO_{20}$. *Europhysics Letters* **46,** 389 (1999).
29. Valant, M.; Suvorov, D. Processing and dielectric properties of sillenite compounds $Bi_{12}MO_{20-\delta}$ (M = Si, Ge, Ti, Pb, Mn, $B_{1/2}P_{1/2}$). *Journal of the American Ceramic Society* **84**, 2900 (2001).
30. Aldrich, R. E.; Hou, S. L.; Harvill, M. L. Electrical and optical properties of $Bi_{12}SiO_{20}$. *Journal of Applied Physics* **42**, 493 (1970).
31. Nagao, Y.; Mimura, Y. Epitaxial Growth of $Bi_{12}SiO_{20}$ films by Chemical Vapor Deposition. *Japanese Journal of Applied Physics* **24**, 954 (1985).
32. Alonso, J. C.; Diamant, R.; Horo-Poniatowski, E.; Fernandez-Guasti, M.; Munoz, G.; Comarillo, I.; Jouanne M.; Morhange, J. F. Raman characterization of $Bi_{12}SiO_{20}$ thin films obtained by pulsed laser deposition. *Applied Surface Science* **109-110**, 359 (1997).
33. Okada, T.; Yahiro, F.; Uetsuhara, H.; Nakata, Y.; Maeda, M.; Higuchi, S.; Ueda, K. Deposition of highly oriented $Bi_{12}SiO_{20}$ thin films on Y-stabilized zirconia and SiO_2 by pulsed-laser deposition. *Applied Physics* **A 69**, S723 (1999).
34. Plyaka, S. N.; Sokolyanskii, G. Ch.; Klebanskii, E. O.; Sadovkaya, L. Ja. Conductivity of the $Bi_{12}SiO_{20}$ thin films. *Condensed Matter Physics* **2**, 625 (1999).
35. Klebanskii, E. O.; Kudzin, A. Yu.; Pasalskii, V. M.; Plyaka, S. N.; Sadovskaya, L. Ya. Thin sol-gel bismuth silicate films. *Physics of the solid state* **41,** 913 (1999).
36. Jain, M.; Tripathi, A. K.; Goel, T. C.; Pillai, P. K. C. Preparation and characterization of bismuth silocate (BSO) thin film by the sol-gel technique. *Journal of Matterials Science Letters* **18**, 479 (1999).
37. Brinker, C. J.; Scherer, G. W. *Sol-Gel Science:The Physics and Chemistry of Sol-Gel Processing* (Academic Press, San Diego, 1989).
38. Pierre, A. C. *Introduction to sol-gel processing* (Kluwer Academic Publisher, Boston, 1998).

39. Uhlmann, D. R.; Rajendran, G. P. *Coatings: The land of opportunity for sol-gel coatings, Ultrastructure processing of advance ceramics* (John Wiley, New York, 1988).
40. Vergöhl, M.; Malkomen, N.; Matthée, T.; Bräuer, G.; Richter, U.; Nickol, F. W.; Bruch, J. In situ monitoring of optical coatings on architectural glass and comparison of the accuracy of the layer thickness attainable with ellipsometry and photometry. *Thin Solid Film* **392**, 258 (2001).
41. Disclih, H. *Thin films from the sol-gel process in sol-gel technology for thin films, fibers, preforms, electronics and specialty form.* (L. C. Klein, ed., Notes Publications, New Jersey, 1988)
42. Matsuda, A.; Tohge, N.; Minami, T. Preparation of $B_2O_3 - P_2O_5 - SiO_2$ coating films by the sol-gel method. *Journal of Materials Science* **27** 4189 (1992).
43. Armelao, L.; Colombo, P.; Fabrizio, M. Synthesis of Bi_2O_3 and $Bi_4(SiO_4)_3$ thin films by the sol-gel method. *Journal of Sol-Gel Science and Technology* **13** 213 (1998).
44. Uhlmann, D. R.; Dawley, J. T.; Poisl, W. H.; Zelinski, B. J. J. Ferroelectric films. *Journal of Sol-gel science and technology* **19**, 53 (2000).
45. Cerc Korošec, R.; Bukovec, P.; Pihlar, B.; Padežnik Gomilšek, J. The role of thermal analysis in optimization of the electrochromic effect of nickel oxide thin films, prepared by the sol-gel method. Part I. *Thermochimica Acta* **402** 57 (2003).
46. Cerc Korošec, R.; Bukovec, P.; Pihlar, B.; Padežnik Gomilšek, J. The role of thermal analysis in optimization of the electrochromic effect of nickel oxide thin films, prepared by the sol-gel method. Part II. *Thermochimica Acta* **410** 65 (2004).
47. De Santics, O.; Gomez, L.; Pellegri, N.; Parodi, C.; Marajofsky, A.; Duran, A. Protective Glass Coatings on metallic substrate. *Journal of Non-Crystalline Solids* **121**, 338 (1990).
48. Bradley, D. C.; Mehrotra, R. C.; Gaur, D. P. *Metal Alkoxides* (Academic Press, New York, 1978)
49. Livage, J.; Henry, M.; Sanchez, C. Sol-gel chemistry of transition metal oxide. *Journal of Solid state chemistry* **18**, 259 (1998).
50. Crisan, M.; Braileanu, A.; Raileanu, M.; Crisan, D.; Teodorescu, V. S.; Birjega, R.; Marinescu, V. E.; Madarasz, J.; Pokol, G. TiO_2-based nanopowders obtained from different Ti-alkoxides. *Journal of Thermal Analysis and Calorimetry* **88**, 301 (2007).
51. Fidalgo, A.; Ciriminna, R.; Ilharco, L. M.; Pagliaro, M. Role of the Alkyl−Alkoxide Precursor on the Structure and Catalytic Properties of Hybrid Sol−Gel Catalysts. *Chemistry of Materials* **17** 6686 (2005).
52. Babanneau, F.; Doef, S.; Leaustic, A.; Sanchez, C.; Cartier, C.; Verdaguer, M. XANES and EXAFS study of titanium alkoxides. *Inorganic Chemistry* **27**, 3166 (1988).
53. Barray Carter, C.; Grant Nortor, M. *Ceramics Materials, Science and Engineering* (Marcel Dekker, New York, 1999)
54. Kwon, S. W.; Park, S. B. Effect of precursors on the preparation of lithium aluminates. *Journal of Nuclear Materials* **264** 131 (1997).
55. Brinker, C. J.; Mukherjee, S. P. Conversion of monolithic gels to glasses in a multicomponent silicate system. *Journal of Material Science* **16**, 1980 (1981).
56. Toyoda, M.; Payne, M. Synthesis and characterization of an acetate-alkoxide precursor for sol-gel derived $Bi_4Ti_3O_{12}$. *Material Letters* **18,** 84 (1993).
57. Malic, B.; Arcon, I.; Kosec, M.; Kodre, A. A structural study of amorphous alkoxide-derived lead titanium complexes. *Journal of Material Research* **12,** 2602 (1997).
58. Boulmaaz, S.; Papiernik, R.; Hubert-Pfalzgraf, G. L.; Septe, B.; Vaissermann, J. Chemical routes to oxides : alkoxide vs. alkoxide-acetate routes : synthesis, characterization, reactivity and polycondensation of $MNb_2(OAc)_2(OPr^i)_{10}$ (M = Mg, Cd, Pb) species. *Journal of Material Chemistry* **7,** 2053 (1997).

59. Toyoda, M.; Hamaji, Y.; Tomono, K.; Payne, D. A. Synthesis and characterization of $Bi_4Ti_3O_{12}$ thin films by sol-gel processing. *Japanese Journal of Applied Physics* **32**, 4158 (1993).
60. Schwartz, R. W.; Schneller, T.; Waser, R. Chemical solution deposition of electronic oxide films. *Comptes Rendus Chimie* **7**, 433 (2004).
61. Li, D. X.; Thompson W. J. Mullite Formation Kinetics of a Single-Phase Gel. *Journal of the American Ceramic Society* **73**, 964 (1990).
62. Yao, F. W.; Hong, W.; Xia, S. S. Preparation and characterization of bismuth titanate $Bi_{12}TiO_{20}$ nanocrystals. *Journal of Materials Science Letters* **21**, 1803 (2002).
63. Gu, H.; Dong, C., Chen, P.; Bao, D.; Kuang, A.; Li, X. Growth of layered perovskite $Bi_4Ti_3O_{12}$ thin films by sol-gel method. *Journal of Crystal Growth* **186** 403 (1998).
64. Gu, H.; Cao, W.; Song, R.; Zhou, X.; Wang, J. Effects of precursor solution pH value and substrate texture on orientation degree of sol-gel derived bismuth titanate thin films. *Physica Status Solidi* **198**, 282 (2003).
65. Kim, S. H.; Kim, C. E.; Oh, Y. J.; Preparation of $PbTiO_3$ thin films using an alkoxide-alkanolamine sol-gel system. *Journal of Materials Science* **30**, 5639 (1995).
66. Kim, C. E.; Park, Y. I.; Lee, H. W. Preparation of $PbTiO_3$ fibres using triethanolamine-complexed alkoxide. *Journal of Materials Science Letters* **16,** 96 (1997).
67. Li, P.; Ferguson B.; Francis L. F. Sol-gel processing of lithium disilicate 2: crystallization and microstructure development of coatings. *Journal of Materials Science* **30**, 4076 (1995).
68. Madeswaran, S.; Giridharan, N. V.; Jayavel, R. Sol-Gel synthesis and property studies of layered perovskite bismuth titanate thin films. *Material Chemistry and Physics* **80**, 23 (2003).
69. Xie, D.; Pan, W.; Shi, H. Synthesis and characterization of $Sr_{1-x}Ba_xBi_4Ti_4O_{15}$ ferroelectrics materials. *Materials Science and Engineering* **B99**, 352 (2003).
70. Chen, K. C.; Tsuchiya, T.; Mackenzie, J. D. Sol-gel processing of silica: I. The role of the starting compounds. *Journal of Non-Crystalline Solids* **81,** 227 (1986).
71. Guglielmi, M.; Carturan, G. Precursors for Sol-Gel Preparations. *Journal of Non-Crystalline Solids* **100** 16 (1988).
72. Fidalgo, A.; Ilharco, L. M. Thickness and structure of sol-gel hybrid films: II-the role of the solvent. *Journal of Sol-Gel Science and technology* **26**, 357 (2003).
73. Orignac, H. C.; Almeida, R. M. Influence of Solvent Concentration on the Microstructure of SiO_2-TiO_2 Sol-Gel Films. *Journal of Sol-Gel Science and technology* **8**, 243 (1997).
74. Gonzales, M. B.; Wu, A.; Vilarinho, P. M. Influence of solvents on microstructure and dielectric properties of $Ba_{0.5}Sr_{0.5}TiO_3$ thin films prepared by a diol-based sol-gel process. *Chemistry of Materials* **18**, 1737 (2006).
75. Pope, E. J. A.; Mackenzie, J. C. Sol-gel processing of silica: II. The role of the catalyst. *Journal of Non-Crystalline Solids* **87**, 185 (1986).
76. Parrill, T. M. Heat treatment of spun-on acid-catalyzed sol-gel silica films. *Journal of Materials Research* **9**, 723 (1994).
77. Silva C. R.; Airoldi, C. Acid and Base Catalysts in the Hybrid Silica Sol–Gel Process. *Journal of Colloid and Interface Science* **195**, 381 (1997).
78. Debsikdar, J. C. Transparent zirconia gel-monolith from zirconium alkoxide. *Journal of Non-Crystalline Solids* **86**, 231 (1986).
79. Debsikdar, J. C. Preparation of transparent nom-crystalline stoichiometric magnesium aluminate gel-monolith by the sol-gel process. *Journal of Materials Science* **20** 44 (1985).
80. Verma, A.; Samanta, S. B.; Bakhshi, A. K.; Agnihotry, S. A. Effect of stabilizer on structural, optical and electrochemical properties of sol-gel derived spin coated TiO_2 films. *Solar energy materials and solar cells* **88**, 47 (2005).

81. Lenza, R. F. S.; Vasconcelos, W. L. Structural Evolution of silica sols modified with formamide. *Journal of Materials Research* **4**, 175 (2001).
82. DeLange, R. S. A.; Hehhink, J. H. A; Kelzer, K.; Burggraaf, A. J. Polymeric-silica-based sols for membrane modification applications: sol-gel synthesis and characterization with SAXS. *Journal of Non-Crystalline Solids* **191**, 1 (1995).
83. Winter, R.; Chan, J. B.; Frattini, R.; Jonas, J. The effect of fluoride on the sol-gel process. *Journal of Non-Crystalline Solids* **105** 214 (1988).
84. Brinker, C. Hydrolysis and condensation of silicates: Effects on structure. *Journal of Non-Crystalline Solids* **100**, 31 (1988).
85. Corriu, R.; Guerrin, C.; Moreau, J. A general route to five coordinated hydridosilicates. *Topics in Stereochemistry* **15**, 43 (1984).
86. Doeuff, S.; Henry, M.; Sanchez, C.; Livage, J. The gel route to Cr^{3+}-doped TiO_2, an ESR study. *Journal of Non-Crystalline Solids* **89**, 84 (1987).
87. Doeuff, S.; Henry, M.; Sanchez, C.; Livage, J. Hydrolysis of titanium alkoxides: Modification of the molecular precursor by acetic acid. *Journal of Non-Crystalline Solids* **89**, 206 (1987).
88. Camper, A.; Arroyo, R.; Sanchez, C.; Livage, J. *Ultra structure processes of ceramics, glasses and composites (L. L. Hench & D. R. Ulrich john Wiley & Sons*, San Diego, 1987).
89. Sugahara, Y.; Okada, S.; Sato, S.; Kuroda, K.; Kato, C. ^{29}Si-NMR study of hydrolysis and initial polycondensation processes of organoalkoxysilanes. II. Methyltriethoxysilane. *Journal of Non-Crystalline Solids* **167**, 21 (1994).
90. Klein, L. C. Sol-gel processing of silicates. *Annual Review of Materials Science* **15,** 227 (1985).
91. Schmidt, H.; Scholze, H.; Kaiser, A. Principle of hydrolysis and condensation reaction of alkoxysilanes. *Journal of Non-Crystalline Solids* **63**, 1 (1984).
92. Iler, R. K. *The chemistry of Silica* (John Willey & Sons, Canada, 1979).
93. Aelion, R.; Loebel, A.; Eirich, F. J. Hydrolysis of Ethyl Silicate. *Journal of the American Chemical Society* **72**, 5705 (1950).
94. Kelts, L. W.; Effinger, N. J.; Melpolder, S. M. Sol-gel chemistry studied by ^{1}H and ^{29}Si nuclear magnetic resonance. *Journal of Non-Crystalline Solids* **83**, 353 (1986).
95. Engelhardt, V. Q.; Altenburg, W.; Hoebbel, D. ^{29}Si-NMR-Spetkroskopie an Silicatlosungen. IV. Untersuchungen zur Kondensation der monokieselsaure. *Zeitschrift fur Anorganische und Allgemeine Chemie* **428,** 43 (1977).
96. Pohl, E. R.; Osterholtz, F. D. *Molecular characterization of composite interfaces* (Springer, 1985).
97. Swain, C. G.; Esteve, M.; Jones, R. H. Organosilicon Chemistry: the mechanisms of Hydrolysis of Triphenylsilylfluoride and Triphenylmethylfluoride in 50%Water-50%Acetone. *Journal of the Chemical Society* **71**, 965 (1949).
98. Orcel, G.; Chung, J. Sol-gel kinetics of tetraethylorthosilicate (TEOS) on acid catalyst. *Journal of Non-Crystalline Solids* **110,** 26 (1989).
99. Artaki, I.; Zerda, T.; Jones, J. NMR and Raman study of the hydrolysis reaction in sol-gel process. *Journal of Physical Chemistry* **89**, 4399 (1985).
100. Henc, L. L.; West, J. K. The sol-gel process. *Chemical Reviews* **90**, 33 (1990).
101. Wang, Z. L.; Liu, Y.; Zhong, Z. *Handbook of Nanophase and Nanostructured Materials* (Kluwer Academic Publisher, New York, 2003).
102. Colby, M. W.; Osaka, A.; MacKenzie, J. D. Effect of temperature and R_h on formation of silica gel. *Journal of Non-Crystalline Solids* **82,** 37 (1986).
103. Aelion, A.; Loebel, A.; Eirich, F. Hydrolysis of the Ethyl Silicate. *Journal of the American Chemical Society* **72**, 5705 (1950).

104. Simões, A. Z.; González, A. H. M.; Zaghete, M. A.; Cilense, M.; Varela, J. A.; Stojanovic, B. D. Influence of viscosity and ionic concentration on morphology of PLZT thin films. *Applied Surface Science* **172**, 68 (2001).
105. De Costa, G. C.; Simoes, A. Z.; Gasparotto, G.; Zaghete, M. A.; Stojanovic, B. D.; Cilense, M.; Varela, J. A. Effect of viscosity and temperature on the microstructure of BBT thin films. *Journal of Materials Research* **6**, 347 (2003).
106. Hong, J.-K.; Kim, H.-R.; Park, H.-H. The effect of sol viscosity on the sol–gel derived low density SiO_2 xerogel film for intermetal dielectric application. *Thin Solid Films* **332,** 449 (1998).
107. Fuierer, P.; Li, B. Nonepitaxial Orientation in Sol-Gel Bismuth Titanate Films. *Journal of the American Ceramic Society* **85**, 299 (2002).
108. Partlow, D. P.; Yoldas, B. E. Colloidal versus polymer gels and monolithic transformation in glass-forming systems. *Journal of Non-Crystalline Solids* **46,** 156 (1981).
109. Cohen, E. D.; Gutoff, E. B. *Choosing a coating method in modern coating and drying technology* (VCH Publisher, Inc., New York, 1992).
110. Ichiki, M.; Zhang, L.; Yang, Z.; Ikehara, T.; Maeda, R. Thin film formation on non-planar surface with use of spray coating fabrication. *Microsystem technologies* **10**, 360 (2004).
111. Marage**,** P.; Langlet, M.; Joubert, J. C. A new route for the deposition of SiO_2 sol-gel coatings. *Thin Solid Films* **238**, 218 (1994).
112. Kawayama, I; Kontani, K.; Tonuchi, M. Initial growth of $SrBi_2Ta_2O_9$ thin films on various substrates. *Thin Solid Films* **464-465**, 160 (2004).
113. Cheng, W. X.; Ding, A. L.; Qui, P. S.; He, X. Y.; Zheng, X. Sh. Optical and dielectrical properties of $(Zn_{0.8},Sn_{0.2})TiO_4$ thin films prepared by sol-gel process. *Materials Science Engineering* **B99**, 382 (2003).
114. Hwang, K.-S.; Kang B.-A.; Jeon, Y.-S.; An, J.-H.; Kim, B.-H.; Nishio, K; Tsuchiya, T. AFM study of LaNiO3 thin film on various single crystal substrates prepared by using metal naphthenate precursor. *Surface & Coatings Technology* **190**, 331 (2005).
115. Simões, A. Z.; Gonzales, A. H. M.; Zaghete, M. A.; Varela, J. A.; Stojanovic, B. D. Effect of the Atmosphere and Substrate on the Crystallization of PLZT Thin Films. *Journal of Materials Research* 3, 1 (2000).
116. Yi, G.; Sayer, M. Sol-Gel Processing of Complex Oxide Films. *Ceramic Bulletin* 70, 1173 (1991).
117. Carreras, E. S.; Chabert, F.; Dunstan, D. E.; Franks, G. V. Avoiding cracks during drying of thin films from aques suspensions. *Journal of Colloid and Interface Science* **313**, 160 (2007).
118. Zarzycki, J.; Prassas, M.; Phalipponi, Synthesis of glass from gel. *Journal of Materials Science* **17**, 3371 (1982).
119. Brinker, C. J.; Scherrer, G. W. Sol-Gel Glass. I. Gelation and Structure**.** *Journal of Non-Crystalline Solids* **70,** 301 (1985).
120. Scherer, G. W.; Brinker, C. J.; Roth, E. P. Sol-Gel Glass. III. Viscous sintering. *Journal of Non-Crystalline Solids* **72,** 369 (1985).
121. Wongcharee, K.; Brungs, M.; Chaplin, R.; Hong, Y. J.; Sizgek, E. Influence of Surfactant and Humidity on Sol-Gel Macroporous Organosilicate Coatings. *Journal of Sol-Gel Science and Technology* **29**, 115 (2004).
122. Chang, D.-A.; Choh, Y.-H.; Hisieh, W.-F.; Lin, P.; Tseng, T.-Y. The role of drying-control chemical additives on the preparation of sol-gel derived PLZT thin films. *Journal of Materials Science* **28,** 6691 (1993).
123. Cairncross, R. A.; Francis, L. F.; Scriven, L. E. Competing Drying and Reaction Mechanisms in the Formation of Sol-Gel Films, Fibers and Spheres. *Drying Technology Journal* **10**, 893 (1992).

124. Cairncross, R. A.; Francis, L. F.; Scriven, L. E. Predicting Drying in Coatings that React and Gel: Drying Regime Maps. *AICHE Journal* **42**, 55 (1995).
125. Hennings, D.; Rosenstein, G.; Schreinemacher, H. Sol-gel preparation of barium titanate from barium-titanium acetate gel precursor. *Journal of European Ceramic Society* **8**, 107 (1991).
126. Brinker, C. J.; Scherer, G. W.; Roth, E. P. Sol-Gel-Glass. II: Physical and Structural Evolution During Constant Heating Rates. *Journal of Non-Crystalline Solids* **72**, 345 (1985).
127. Schwartz, R. W.; Voigt, J. A.; Tuttle, B. A.; Payne, D. A.; Reichert, T. L.; Dasalla, R. S. Comments on the effects of solution precursor characteristics and thermal processing conditions on the crystallization behaviour of sol-gel derived PZT thin films. *Journal of Materials Research* **12**, 444 (1997).
128. Roy, R. *Journal of American Ceramic Society* **52**, 344 (1969).
129. Kong, L. B.; Ma, J. Randomly oriented $Bi_4Ti_3O_{12}$ thin films derived from a hybrid sol-gel process. *Thin Solid Films* **179**, 89 (2000).
130. Joshi, V.; McCartney, M. L. The Influence of Water of Hydrolysis on Microstructural Development in Sol-gel Derived $LiNbO_3$ Thin Films. *Journal of Materials Research* **8**, 2668 (1992).
131. Zhai, J.; Chen, H. Orientation Control and Dielectric Properties of Sol-Gel Deposited (Ba, Sr)TiO_3 Thin Films for Room Temperature Tuneable Element Applications. *Journal of the Korean Ceramic Society* **40**, 380 (2003).
132. Eichost, D. J.; Payne, D. A. Processing and properties of sol-gel derived lithium niobate thin film. *Material Research Society Proceedings* **121**, 773 (1990).
133. Song, S.; Zhai, J.; Yao, X. Effects of buffer layer on the dielectric properties of $BaTiO_3$ thin films prepared by sol-gel method. *Material Science and Engineering B* **145**, 28 (2007).
134. Koutsaroff, I. P.; Woo, P.; McNeil, L.; Zelner, M.; Kassam, A.; Capanu, M.; Chmiel, L.; McClelland, B.; Cervin-Lawry, A.: Dielectric Properties of (Ba, Sr) TiO_3 MOD Films Grown on Various Substrates. *Proceedings of 13th IEEE International Symposium of Application of Ferroelectrics* 247-250 2002.
135. Thompson, C. V. Grain Growth in Thin Film. *Annual Review of Materials Science* **20**, 245 (1990).
136. Vratny, F. Infrared spectra of Metal Nitrates. *Applied Spectroscopy* **13**, 59 (1959).
137. Doeuff, S.; Henry, M.; Sanchez, C.; Livage, J. Hydrolysis of titanium alkoxides: Modification of the molecular precursor by acetic acid. *Journal of Non-Crystalline Solids* **89**, 206 (1987).
138. Orel, B.; Ješe, R.; Lavrenčič, U.; Grdadolnik, J.; Puchberger, M. IR ATR spectroscopic studies of aprotic condensation of $(EtO)_3$-Si-R-Si$(OEt)_3$ and R-Si$(OEt)_3$ systems with carboxylic acids. *Journal of non-crystalline solids* **351**, 530 (2005).
139. Yi, G.; Sayer, M. An Acetic Acid/Water-Based Sol-Gel PZT Process: I. Modification of Zr and Ti Alkoxide with Acetic Acid. *Journal of Sol-Gel Science and Technology* **6**, 65 (1996).
140. Mehring, M.; Mansfeld, D.; Paasalmaa, S.; Schurmann, M.; Polynuclear Bismuth-Oxo Cluster: Insight into the Formation Process of a Metal Oxide. *Chemistry A European Journal* **12,** 1767 (2006).
141. Smith, B. *Infrared spectral interpretation: a systematic approach* (CRC Press, Florida, 1999)
142. Ardelan, I.; Cora, S.; Lucacel, R.; Hulpus, O. EPR and FT-IR spectroscopic studies of B_2O_3-Bi_2O_3-MnO. *Solid State Science* **7**, 1438 (2005).
143. Chehab, S.; Conflant, P.; Drache, M.; Boivin, J. C.; McDonald, G. Solid-state reaction pathways of Sillenite-phase formation studied by high-temperature X-ray

diffractometry and differential thermal ananlysis. *Materials Research Bulletin* **38**, 875 (2003).

144. Fei, Y. T.; Fan, S. J.; Sun, R. Y.; Xu, J. Y. Crystallizing behaviour of $Bi_2O_3 - SiO_2$ system. *Journal of Materials Science Letters* **19**, 893 (2000).
145. Lefevre, M. J.; Speck, J. S.; Schwartz, R. W.; Dimos, D.; Lockwood, S. J. Microstructural development in sol-gel derived lead zirconate titanate thin films: The role of precursor stoichiometry and processing environment. *Journal of Materials Research* **11**, 2076 (1996).
146. Tirumala, S.; Desu, S. B.; Rastogi, A. Role of bismuth precursor in crystallization of $SrBi_2Ta_2O_9$ thin films. *Applied Physics A* **70**, 253 (2000).
147. Viart, N.; Ninznasnsky, D.; Rehspringer, J. L. Structural evolution of a formamide modified sol-spectroscopic study. *Journal of Sol-Gel Science and Technology* **8**, 183 (1997).
148. Petrov, P. K.; Mc Alford, N.; Gevorgyan, S. Techniques for microwave measurements of ferroelectric thin films and their associated error and limitations. *Measurement Science and Technology* **16**, 583 (2005).
149. Krupka, J.; Geyer, R. G.; Baker-Jarvis, J.; Ceremuga, J. Measurements of the complex permittivity of microwave circuits board substrates using split dielectric resonator and re-entrant cavity techniques. *Seventh international Conference on Dielectric Materials Measuremnts& Applications*, IEE, London, 21-24.
150. Li, J.; Kakemoto, H.; Wada, S.; Tsurumi, T. Dielectric relaxation in gigahertz region and phase transition of $BaTiO_3$-based ceramics. *Journal of Applied Physics* **100**, 024106 (2006).

Index of Figures

Figure 33: FT-IR spectrums of a) TEOS, b) CH_3COOH and c) CH3COOH-TEOS solution.

Figure 34: FT-IR spectrums of a) TEOS-$C_4H_{10}O_2$, b) TEOS-CH_3COOH, c) CH_3COOH-$C_4H_{10}O_2$, d) $Bi(NO_3)_3{\cdot}5H_2O$- CH_3COOH and e) sol R_h60.

Figure 35: Molecular structure of trimeric [$Bi(OSiEt_3)_3$]. The large black spheres correspond to bi atoms and the smaller ones to C atoms, while O and Si atoms are represented by different shades from brighter to darker, respectively.

Figure 36: Dependence of the sol concentration on the viscosity of sol R_h 60.

Figure 37: Dependence of the sol concentration on the time of gelation of sol R_h 60.

Figure 38: FT-IR spectrums of a) precipitate in sol R_h 60 and b) $Bi(NO_3)_3{\cdot}5H_2O$.

Figure 39: FT-IR spectrum of thin film deposited from sol R_h 60.

Figure 40: TEM analysis of a) and b) dried thin film deposited from sol R_h 60 and c) electron diffraction pattern of the crystalline particle (Fig. 31 b).

Figure 41: The EDS spectrum of crystalline particle shown in Fig. 40 b.

Figure 42: TEM analysis of a) and b) dried thin film deposited from sol R_h 60 aged for 24h and c) electron diffraction pattern of the crystalline particle (Fig. 42 b).

Figure 43: X-ray diffraction patterns of thin films deposited on a sapphire substrate and heated at various temperatures.

Figure 44: X-ray diffraction patterns of thin films deposited on a silicon substrate annealed at 700°C, 1h.

Figure 45: Binary phase diagram of Bi_2O_3-SiO_2 system.

Figure 46: X-ray diffraction patterns of BSO thin films deposited on the Au substrate annealed at 700°C/1h.

Figure 47: FE-SEM micrographs of the microstructure of thin films annealed at 700 °C deposited on substrate a) Pt/TiO_2/SiO_2/Si, b) sapphire, c) spinel.

Figure 48: FT-IR spectrums of a) sol R_h 5 b) $Bi(NO_3)_3{\cdot}5H_2O$, c) CH_3COOH and d) ethanolamine.

Index of Tables

Appendix

Publications

Original scientific article

1. VEBER, Asja, VALANT, Matjaž, SUVOROV, Danilo. The synthesis of $Bi_{12}SiO_{20}$-based thin films by the sol-gel method = Sinteza tankih plasti Bi12SiO20 z metodo sol-gel. *Mater. tehnol.*, 2005, letn. 39, št. 1/2, str. 25-28

2. VEBER, Asja, KUNEJ, Špela, SUVOROV, Danilo. Synthesis and microstructural characterization of $Bi_{12}SiO_{20}$ (BSO) thin films produced by the sol-gel process. *Ceram. int.*. [Print ed.], 2009, vol. 36, no. 1, str. 245-250.

3. VEBER, Asja, KUNEJ, Špela, SUVOROV, Danilo. The effect of the solvent on the formation of sol-gel-derived $Bi_{12}SiO_{20}$ thin films. *J. Eur. Ceram Soc.* 2010- article in press

Published scientific conference contribution abstract

4. VEBER, Asja, VALANT, Matjaž, SUVOROV, Danilo. Sinteza tankih plasti $Bi_{12}SiO_{20}$ z metodo sol-gel = The synthesis of $Bi_{12}SiO_{20}$ z metodo sol-gel. V: JENKO, Monika (ur.). 12. konferenca o materialih in tehnologijah, Portorož, 27-29 september 2004 = 12th Conference on materials and technology, Portorož, Slovenia, 27-29 September, 2004. *Program in knjiga povzetkov*. Ljubljana: Inštitut za kovinske materiale in tehnologije], 2004, str. 48.

5. KUNEJ, Špela, VEBER, Asja, SUVOROV, Danilo. Preparation of the $Bi_{12}SiO_{20}$ thim films by the sol-gel method. V: *SLONANO 2007 : 10-12 October, Jožef Stefan Institute, Ljubljana, Slovenia : programme & abstracts*. Ljubljana: Jožef Stefan Institute, 2007.

6. KUNEJ, Špela, VEBER, Asja, SUVOROV, Danilo. Preparation of the $Bi_{12}SiO_{20}$ thin films by the sol-gel method. V: *SLONANO 2007 : 10-12 October, Jožef Stefan Institute, Ljubljana, Slovenia : programme & abstracts*. Ljubljana: Jožef Stefan Institute, 2007.

7. VEBER, Asja, SUVOROV, Danilo. Effects of the precursor solution on sol-gel-derived $Bi_{12}SiO_{20}$ thin films. V: SGM'08, 5th International Conference on Sol-Gel Materials, Research, Technology, Applications, 1-5 June 2008, Trzebieszowice. *Abstracts*. [S. l.: s. n.], 2008, str. 77.

8. VEBER, Asja, SUVOROV, Danilo. The thickness, morphology and structure of sol-gel $Bi_{12}SiO_{20}$ thin films. V: USKOKOVIĆ, Dragan (ur.). Tenth Annual Conference of the Yugoslav Materials Research Society YUCOMAT 2008, Herceg Novi, Montenegro, September 8-12,2008. *Programme and the book of abstracts*. Belgrade: Institute of Technical Sciences of SASA, 2008, str. 74.

9. VEBER, Asja, KUNEJ, Špela, SUVOROV, Danilo. Synthesis and characterization of $Bi_{12}SiO_{20}$ (BSO) thin films produced using the sol-gel process. V: KOBE, Spomenka (ur.), ŽUŽEK ROŽMAN, Kristina (ur.), NOVAK, Saša (ur.), FIDLER, Sanja (ur.). *WomenInNano winter school : 7-9 February 2008, Kranjska Gora, Slovenia : abstract book*. [S.l.: s.n.], 2008, str. 115.

10. VEBER, Asja, SUVOROV, Danilo. Synthesis and characterization of sol-gel prepared $Bi_{12}SiO_{20}$ thin films. V: XV. International Sol-Gel Conference, Sol-Gel'09, Porto de Galinhas, Pernambuco, Brazil, August 23-27, 2009. *Book of abstracts*. [S. l.]: ISGS: = International Sol-Gel Society, 2009, str. 78.

11. VEBER, Asja, SUVOROV, Danilo. Vpliv topila na $Bi_{12}SiO_{20}$ tanke plasti pripravljene s sol-gel metodo. V: ISKRA, Jernej (ur.), MILOŠEV, Ingrid (ur.). *Dan mladih raziskovalcev 2009*. Ljubljana: Institut "Jožef Stefan", 2009, 1 str.

12. PADEŽNIK GOMILŠEK, Jana, VEBER, Asja, KODRE, Alojz, SUVOROV, Danilo. EXAFS study of synthesis of sol-gel prepared $Bi_{12}SiO_{20}$ thin films. V: *14th International conference on X-ray absorption fine structure, Camerino, Italy, 26-31 July 2009 : program and abstracts*. [S. l: s. n.], 2009, str. 183.

13. BRAČKO, Ines, VEBER, Asja, OTONIČAR, Mojca, ŠETINC, Tina, DOŠLER, Urban, ŽUNIČ, Vojka. Predstavitev mladih raziskovalcev Odseka za raziskave sodobnih materialov. V: ŠETINA, Barbara (ur.), JUNKAR, Ita (ur.), KALUŽA, Boštjan (ur.), ELERŠIČ, Kristina (ur.). 1. študentska konferenca Mednarodne podiplomske šole Jožefa Stefana, 19. - 20. maj 2009, Ljubljana, Slovenija = 1st Jožef Stefan International Postgraduate School Student's Conference, 19th - 20th May 2009, Ljubljana, Slovenia. *Zbornik prispevkov*. Ljubljana: Mednarodna podiplomska šola Jožefa Stefana, 2009, str. 8-9.